MINISTRY OF TECHNOLOGY

AERONAUTICAL RESEARCH COUNCIL
REPORTS AND MEMORANDA

Wind Tunnel Measurements of the Low Speed Stalling Characteristics of a Model of the Hawker-Siddeley Trident 1C

By D. ISAACS
Aerodynamics Dept., R.A.E., Bedford

LONDON: HER MAJESTY'S STATIONERY OFFICE
1969
PRICE £1 10*s* 0*d* [£1·50] NET

Wind Tunnel Measurements of the Low Speed Stalling Characteristics of a Model of the Hawker-Siddeley Trident 1C

By D. ISAACS

Aerodynamics Dept., R.A.E., Bedford

Reports and Memoranda No. 3608*
May, 1968

Summary.

Tests have been made in the 8 ft × 8 ft wind tunnel on a 1/18·86 scale model in order to investigate the effects of Reynolds number and Mach number on the low speed stalling characteristics. In particular, measurements of lift and pitching moment were obtained in conjunction with flow visualization studies using tufts attached to the wing upper surface. The investigation covered a range of Reynolds number based on standard mean chord from $1 \cdot 12 \times 10^6$ to $4 \cdot 33 \times 10^6$, with a Mach number range extending from 0·15 to 0·30.

The results obtained effectively demonstrate the importance of testing accurate models at sufficiently high Reynolds numbers, and of the necessity of separating Reynolds number effects from Mach number effects, if realistic values of $C_{L\max}$ are to be obtained in wind-tunnel tests and if the full scale type of stall development is to be reproduced at model scale.

The stall development on the present model at the highest Reynolds number of the tests ($R_{\bar{c}} = 4 \cdot 33 \times 10^6$) closely resembles that on the aircraft at the same Mach number (0·2) and the full scale Reynolds number of $14 \cdot 5 \times 10^6$.

LIST OF CONTENTS

Section

---

*Replaces R.A.E. Technical Report 68 108—A.R.C. 30 775.

LIST OF CONTENTS—*continued*

Section

1. *Introduction.*

Over recent years, with the advent of swept-wing transport aircraft having high mounted tailplanes and rear mounted engine nacelles, renewed interest has been shown in aircraft stall and post stall characteristics. Several investigations into the stalling behaviour of this type of aircraft have been reported[1,2,3,4]. The present report describes in detail, tests on a 1/18·86 scale model of the Hawker-Siddeley Trident 1C in the 8 ft × 8 ft wind tunnel at R.A.E. Bedford. The independent effects of Reynolds number and Mach number on the low speed stalling characteristics, were fully investigated by means of force measurements and flow visualization studies using tufts. The report includes a comparison of the stalling behaviour of the present model with that of the aircraft. At the highest Reynolds number of the tests ($R_{\bar{c}} = 4{\cdot}33 \times 10^6$), the stall development on the model closely resembles that on the aircraft at the same Mach number (0·2) and the full scale Reynolds number of $14{\cdot}5 \times 10^6$. In both cases the flow breakdown first occurs over the wing inboard of the fence giving rise to an initial nose-down pitching moment break.

2. *Description of the Model.*

2.1. *General Description.*

The model was of 1/18·86 scale and, with certain exceptions detailed below and in Section 2.2, was fully representative of the Hawker-Siddeley Trident 1C. This aircraft is typical of the subsonic transport layouts with rear engine installations and high mounted tailplanes. It has wings of aspect ratio 5·933, taper ratio 0·271, and a quarter chord sweepback of 35° outboard of the crank in the trailing edge. For definitions of the wing geometry *see* Section 2.2 and Table 1. The wing root-chord leading edge is located at 45 per cent of the fuselage radius below the fuselage centreline. The tailplane is mounted on top of the fin, approximately 2·7 fuselage radii above the fuselage centreline. The two side-engine nacelles are mounted on pylons and are located near the level of the fuselage centreline. Their fore and aft location is roughly half way between the wing trailing edge and the tailplane leading edge. Fig. 1 shows the general arrangement of the model and Fig. 2 shows a photograph of the model mounted in the working section of the 8 ft × 8 ft wind tunnel.

Model forces were measured on a six component internal strain gauge balance, and the model was supported by a single sting. The cross sectional dimensions of the balance and the forward part of the sting were relatively large (3 in. × $2\frac{1}{4}$ in.), compared with sting-balance assemblies used with this type of model for drag measurements at high subsonic speeds (typically $2\frac{1}{4}$ in. diameter), due to the more demanding stiffness requirements of the present tests. Even so, the model incidence range had to be restricted during stalls at the highest Mach number (0·3) due to severe buffeting of the model. The use of such a large support sting necessitated the removal of quite a large section of the rear fuselage in order to give adequate clearance (Fig. 1). The cut-out extended forward on the undersurface of the fuselage to 0·54 in. ahead of the engine nacelle pylon trailing edge, and at the sides of the model, to 1·59 in aft of the pylon trailing edge. Although this asymmetric cut-out could slightly affect the overall level of the lift and pitching moment acting on the model, it is thought that the changes would not vary with model incidence and so would not affect the stalling characteristics.

Because of the large cross-sectional area of the sting support it was not possible to provide any simulation of air flow through the dorsal fin-root intake, which was faired over. Externally, the two side-engine nacelles were fully representative. Internally, there was a slight contraction aft of the inlet followed by a constant area duct to the exit. The mass flow through such a duct would probably not be representative of full scale, but it is unlikely that the model stall would be significantly affected either by the reduction in mass flow of the side intakes, or by the faired over central intake.

The model wings* were each machined from aluminium alloy plate (DTD 5020), and were dowelled and bolted to the balance adaptor. The fuselage, which was made of glass cloth and epoxy resin, was bolted down on to the wings. Positive location was provided, in a fore and aft sense by the wing block, and laterally by the balance adaptor. The side engine nacelles and pylons were made separately from the fuselage, again of glass cloth and epoxy resin, and were bolted into place. The fin was made integral with the fuselage, and here, the fibreglass construction was reinforced with a steel plate on the fin centreline. Similarly, the tailplane, which was bolted and dowelled onto the top of the fin reinforcing plate, was also of fibreglass construction reinforced with a steel plate. The tail setting angle was fixed at a nominal 6° negative relative to the fuselage centreline. This value was chosen as being typical of full-scale conditions with the aircraft near the stalling incidence and with the leading edge drooped, flaps fully deflected, and undercarriage down, etc. The elevator, rudder and undercarriage were not represented on the model. The more important details of the model geometry are summarized in Tables 1 and 2.

2.2. *Wing Details.*

The basic wing planform, with leading edge undrooped and flaps undeflected, has double taper, with kinks in the leading and trailing edges on the skew section 'C' (Fig. 3). Inboard of section 'C' the leading and trailing edge sweepback angles are 38·84° and 3·93° respectively, whereas outboard of section 'C' they are 38·12° and 24·09° respectively. The latter gives a quarter chord sweepback of 35° over the outboard wing. The aspect ratio of the wing is 5·933 and the taper ratio 0·271 (*see* Table 1).

---

*The model was designed around a set of existing wings. These had been part of an early model of the pre-series 1 aircraft which was made for routine tests in the Aircraft Research Association transonic tunnel. In order to obtain a model which was representative of the series 1 aircraft, a new fuselage assembly (including fin, tailplane and nacelles) was made by R.A.E. and fitted to the existing wings after their span had been increased by means of a spacer located on the model centreline.

On the aircraft there is provision for drooping the entire wing leading edge between section 'A' and the wing tip as a leading-edge flap. For take-off and landing the leading-edge droop is set at 26°, measured normal to the droop hinge line, whereas in the cruise configuration it is fully retracted. The droop hinge line is located near the wing undersurface (Figs. 13 and 14), and is swept at 37·30° inboard of the kink section 'C', and at 37·05° outboard of it. The chordwise location of the hinge line varies between 10·8 per cent at section 'A' and 15·0 per cent at section 'G'. In the drooped configuration, the gap, which would occur in the upper surface profile between the drooped leading edge or droop 'beak' and the fixed skin aft of the hinge line, is closed by a circular arc profile fairing plate (Figs. 13 and 14). With the leading-edge profile in the cruising configuration, the fairing plate is retracted into the wing. The model had a set of interchangeable leading edges which were readily detachable and pre-set to various droop angles. For the present tests a droop angle of 26°, representative of aircraft high lift conditions, was fitted.

A total of 57 vortex generators per side are fitted to the aircraft wings. 55 of these generators are located on the fairing plates outboard of 46 per cent semi-span, with the remaining 2 generators (Nos. 36 and 37 from the inboard end) located on the droop 'beak' ahead of the fairing plate at approximately 77 per cent semi-span. These were all represented on the model, except that for convenience, all 57 vortex generators were fitted in the location of the fairing plate. The dimensions of the generators were to scale except for height. This was increased by a factor of 1·3 in order to maintain correct scaling of the exposed height above the boundary layer (at $R_{\bar{c}} = 1{\cdot}12 \times 10^6$). The locations and settings of the generators were fully representative of those fitted to the aircraft.

A Kruger flap was located inboard of the wing leading-edge droop but as on the aircraft it did not extend quite as far as the fuselage side (Fig. 4). A fence was fitted to the wing upper surface at 46 per cent semi-span, and two spoilers, each having a triangular streamwise section shape, were located on the fairing plate inboard of the fence (Fig. 3).

Both inboard and outboard double-slotted flaps were represented on the model (Figs. 3, 4 and 5), and were set at a nominal 50° measured normal to the hinge line. The flaps supports were not completely representative (Fig. 4), being the minimum size possible consistent with strength considerations. Ailerons were fitted to the model but were undeflected throughout the tests.

2.3. *Wing Warp and Section Details.*

The full scale height location of the unloaded wing leading and trailing edges (zero g shape) is shown in Fig. 6. The y and z dimensions are measured outboard of the root-rib datum and above the wing horizontal datum respectively. The wing horizontal datum is defined as the plane passing through the root-rib datum leading edge, parallel to the fuselage centreline. Kinks occur in the leading-edge height at the skew sections 'C' and 'H', and in the trailing-edge height at the skew section 'C' only. The location of these and other important sections is shown in Fig. 3. The model wings were manufactured with full allowance for the full scale aeroelastic distortion under steady, level flight, i.e. under 1 g conditions. Details of the full scale wing twist, under zero g conditions (jig twist), and under 1 g conditions, are shown in Fig. 7.

Following the series of tests described in the present Report, the model wings were subjected to a detailed inspection, and wing ordinates were measured on both upper and lower surfaces of port and starboard wings at 7 spanwise stations (stations 'A' to 'G' in Fig. 3). These measurements have been analysed to give the wing geometrical twist error, $\Delta\alpha_\omega$, which is defined as the difference between the full scale 1 g twist and the measured model twist. $\Delta\alpha_\omega$ is zero over the inboard half of the semi-span, but is increasingly negative over the outboard half (Fig. 9a).

In order to examine more closely the significance of the variation of the twist error, $\Delta\alpha_\omega$, with spanwise position, it is necessary to include the effects of the induced upwash due to tunnel constraint. The change in incidence along the wing leading edge due to tunnel constraint, $\Delta\alpha_T$, has been calculated by the method of Acum[5] for $C_L = 1{\cdot}6$ and $1{\cdot}9$, which represent respectively, the minimum and maximum values of $C_{L\,\max}$ achieved during the present tests. This theory takes no account of flaps, wing leading edge droop or wing warp, but the overall level and the spanwise variation are thought to be of the right order. A mean correction for tunnel constraint, $\delta\alpha_T$, has been applied to model incidence in the present results (cf. Section 4), but no attempt has been made to allow for the spanwise variation of induced incidence shown in Fig. 8. Fortuitously, the wing geometric twist error, $\Delta\alpha_{\omega}$, is of opposite sign to the tunnel constraint effect, $\Delta\alpha_T - \delta\alpha_T$, and roughly the same size, so that partial cancellation of these two effects is obtained (Fig. 9b), the degree of cancellation depending on the lift coefficient.

In order to get some idea of the magnitude of the aeroelastic wing twist occurring on the model, a calculation was made using a greatly simplified model of the wing. The wing was assumed to be untapered and to have the same span and standard mean chord as the present model. The angle of sweepback was assumed to be 38·5°, and the section shape was of constant thickness, with a thickness/chord ratio such that it had the same local stiffness as the true wing section. The calculation was performed for a kinetic pressure of 220 lb/sq ft, (corresponding to $M = 0{\cdot}2$, $R_{\bar{c}} = 4{\cdot}33 \times 10^6$) and a lift coefficient of 1·75, giving a total lift force of 1471 lb, half of which was assumed to act on each exposed wing panel. The lift was assumed to be evenly distributed along the 25 per cent chord line. The angle of twist at the tip was calculated to be $-0{\cdot}63°$. However, it is thought that the true wing planform would be somewhat stiffer than the model used in the calculation, and in addition the spanwise centre of pressure would be well inboard of 50 per cent exposed semi-span because of planform taper and flaps. It is probable therefore that the calculated twist would be overestimated by a factor of as much as two, and that a more realistic value of the tip twist would be of the order of $-0{\cdot}3°$, at maximum lift and high kinetic pressure. The effect of the aeroelastic twist on the total twist error, which is negative, is to increase the size but to reduce the amount of spanwise variation (Fig. 9b). Thus the quoted values of stalling incidence will be in error by as much as $-0{\cdot}30°$, with the size of the error varying with Reynolds number, Mach number and lift coefficient.

The wing-section thickness, aft of the leading-edge flap, is shown in Fig. 10. Differences between port and starboard wings are insignificant. Some disagreement between model wing thickness and aircraft wing thickness, adjusted for scale, is apparent (e.g. sections 'A' and 'B'), but is not such as to influence the stall.

Fig. 11 shows the wing-section leading-edge thickness, ahead of the hinge line. Here, although on the model there are no differences between port and starboard wings, there are marked differences between model and aircraft. The principal differences occur on the skew section 'C', where the model section is too thin especially near the nose, and on the outboard sections 'F' and 'G', where the model sections are too thick in the region of the droop 'beak' trailing edge. The wing camber lines are shown in Fig. 12. Here, the differences between port and starboard wings on the model, and between model and aircraft, are negligible.

For sections 'C' and 'F', the actual section shapes are shown in Figs. 13 and 14 respectively. The origin of the scaled wing-section ordinates is at the leading edge of the undrooped section. The model ordinates have been translated parallel to the x and z axes, in order that the leading-edge positions should coincide with those of the scaled aircraft ordinates, and then rotated to allow for the wing twist errors shown in Fig. 9a. Clearly, the error in the upper surface profile of section 'C' is undesirable in that it is likely to promote premature leading-edge separation. On section 'F', the profile shape, although in error, is probably not too seriously at fault to affect the stall significantly.

If these discrepancies in the section shape had been known before the present tests were started, then the profiles could have been made good for the entire tests. However, during the initial tests on the basic configuration (cf. Section 2.4) a premature flow separation occurred, which appeared to originate from the drooped leading edge on section 'C'. After these initial tests, a visual inspection of the leading edge in the vicinity of section 'C' indicated that the profile there was probably unrepresentative. Following discussions with Hawker-Siddeley it was decided, pending a detailed inspection, to modify locally the wing profile on the model by the addition of a leading edge 'chin' on section 'C'. This chin was located mainly on the undersurface although it did extend around the nose to the upper surface to a small extent (Figs. 15 and 16). Its principal effect was to increase locally the leading edge radius. The chin was added to the model as a fairing of polyester resin and filler. It extended along the leading edge for a distance of 0·64 in. (1 ft full scale) on either side of section 'C', and was smoothly faired into the wing profile. At the same time that the chin was added, the opportunity was taken to improve the upper surface profile on section 'C', again using polyester resin and filler. Although a leading edge chin of this type is not fitted to the production aircraft, it had been fitted to the aircraft during the flight development programme, where it was found to have a beneficial effect on the stall. With the vortex generators fitted to the wing to control the stall development, the effect of the leading edge chin on the aircraft stall was found to be no longer noticeable.

2.4. *Model Configuration Details.*

As described in Section 2.3, initial tests were conducted on the *basic configuration.* This consisted of:

(1) Wing leading edge drooped at 26°.

(2) Kruger flaps deflected.

(3) Trailing edge flaps fully deflected at a nominal 50°.

(4) Tailplane setting angle at a nominal $-6°$ relative to fuselage centreline.

(5) Wing fences fitted at 46 per cent semi-span.

(6) Spoilers fitted inboard of fence.

Vortex generators were not fitted to this configuration. Following the local modifications to the wing on section 'C' described in Section 2.3, further tests were made on a model configuration which is described throughout this report as the *final configuration with leading edge chin.* This consisted of the basic configuration with the addition of:

(1) Leading edge chin on section 'C'.

(2) Vortex generators.

Finally, a third series of tests were completed on the *final configuration* which consisted of the basic configuration with the addition of the vortex generators but without the leading edge chin.

In view of the differences between model and aircraft wing sections described in Section 2.3, it is reasonable to take the final configuration with leading edge chin, as being the most representative of full scale, of the configurations tested. The differences between this configuration and the aircraft are thought to be not serious enough to affect comparison of the stall development. Although the most important part of this Report is devoted to that particular configuration, details of the stall development on the basic configuration are included since these results help to explain the stalling behaviour of the final configuration with leading-edge chin. Similarly, a brief account of the stall of the final configuration is included so as to demonstrate more fully the effect of the leading-edge chin.

No attempt was made to fix boundary layer transition on any of the model configurations.

All configurations were tested both with and without tufts attached to the wing upper surfaces. The tufts, 0·75 in. long and approximately 0·040 in. in diameter, were made from the smallest strands obtainable from nylon rope, and each consisted of a large number of very fine untwisted nylon threads. Each one was glued to the wing surface using epoxy resin, care being taken to ensure that the tuft leading edge did not present a step to the approaching flow. An extensive tuft coverage was used (Fig. 2), with 10 rows of tufts inboard of the fence and 11 rows outboard of the fence.

When tufts are used to visualize the flow over a wing, it is essential that their effect on the wing flow is negligibly small, and that changes in the type of flow breakdown should not occur. In typical examples taken from the present case, the effects on C_L (Fig. 17), and C_m (Fig. 18), are fairly small, and are principally to decrease C_L slightly and increase C_m slightly at all incidences, probably due to an increase in the boundary-layer thickness over the rear of the wing.

3. *Test Procedure.*

The stall development was investigated at Mach numbers of 0·15, 0·20, 0·25 and 0·30. At $M = 0·20$, the effect of wide variations in the Reynolds number on the stall was examined, and force measurements and tuft photographs were taken at $R_{\bar{c}} = 1{\cdot}12 \times 10^6$, $2{\cdot}24 \times 10^6$, $3{\cdot}36 \times 10^6$ and $4{\cdot}33 \times 10^6$. At $M = 0{\cdot}15, 0{\cdot}25$ and $0{\cdot}30$ the variation in Reynolds number was limited to $R_{\bar{c}} = 1{\cdot}12 \times 10^6$ and $2{\cdot}24 \times 10^6$. At $M = 0{\cdot}15$ the limitation arose from the maximum allowable tunnel total pressure of 115 in mercury absolute, whereas at $M = 0{\cdot}25$ and $0{\cdot}30$ the range was restricted by maximum allowable kinetic pressure (model strength limitation).

The investigations covered a fuselage incidence range of between $-4°$ and $+22°$, with the interval between consecutive readings being varied between 1° and $\frac{1}{4}°$ as appropriate. Beyond the stall where model buffeting occurred, two or more force measurements were often made at each incidence, although only one tuft photograph was taken at each setting.

At each condition the test procedure was first to pitch the model slowly up to maximum incidence whilst making visual observations of the tuft pattern. This was then repeated so that tuft photographs could be taken and model forces measured at appropriate intervals. The tuft photographs were 'stills' taken with an F–24 camera fitted with a wide angle lens and mounted outside the tunnel working section. When tuft photographs had been taken at all conditions, the tufts were removed and the wing upper surfaces restored to their original condition. Force measurements were then repeated at all conditions.

A limited number of oil flow studies were made of the flow over the wing upper surface at $M = 0{\cdot}20$ and $R_{\bar{c}} = 3{\cdot}36 \times 10^6$. The oil flow mixture used was made up to the following formula:

4 cc Shell Vitrea 72

2 cc Shell Limea 931

3 cc Titanium dioxide ($T_i\,0_2$)

2 drops oleic acid.

4. *Corrections Applied to Results.*

The kinetic pressure and tunnel datum static pressure have been corrected for model blockage but not for wake blockage. The effect of wake blockage on kinetic pressure has been calculated by Maskell's method[6] for one particular configuration (final configuration with leading edge chin) at $M = 0{\cdot}2$ and $R_{\bar{c}} = 4{\cdot}33 \times 10^6$. The following approximate values for the increase in kinetic pressure were obtained,

$\alpha°$	$\Delta q/q$ per cent
17	0·5
18	2·0
20	2·5
21	3·0
22·5	3·5

The greater part of this Report deals with cross-comparisons of results obtained with the present model at different Mach numbers and Reynolds numbers. Since these comparisons should not be affected by wake blockage, corrections for its effect have not been applied. A comparison of the present load measurements (C_L and C_m) with those obtained in full scale stalling tests would not be strictly valid unless the present wind-tunnel results had been corrected for wake blockage. However, the comparison made in Section 5.4 between the stall development on the present model at $M = 0{\cdot}2$ and $R_{\bar{c}} = 4{\cdot}33 \times 10^6$ and the full scale stall development involves only the spanwise and chordwise variations with incidence of the flow separation boundaries. These should not be seriously affected by the changes in kinetic pressure due to wake blockage shown above, and so no attempt has been made to correct these results for wake blockage.

The model incidence has been corrected for deflection under load of the strain gauge balance and sting.

A constraint correction due to Acum[5] has been applied to model incidence,

$$\alpha^{\circ}_{\text{correct}} = \alpha^{\circ} + \delta\alpha^{\circ}_{T},$$

where $\delta\alpha^{\circ}_{T} = 0{\cdot}55\, C_L$.

Although the 'tail-off' value of C_L should be used here it was considered accurate enough to use the 'tail-on' values. As stated previously, in Section 2.3, this theory takes no account of flaps, wing leading edge droop or wing warp but the overall level is probably of the right order. No corrections have been applied to C_m or to tailplane setting angle for the effects of tunnel constraint.

Axial force has been corrected for the difference between measured base pressure and tunnel working section static.

5. *Results.*

Model incidence is measured relative to the fuselage centreline. The moment reference centre is at $0{\cdot}3\,\bar{c}$ (9·346 in aft of wing transverse datum) on the fuselage centreline. The accuracy of the measurements is estimated to be,

$$C_L \pm 0{\cdot}005$$

$$C_m \pm 0{\cdot}002$$

$$\alpha \pm 0{\cdot}03^{\circ}$$

5.1. *Stall Development at $M = 0{\cdot}20$.*

(a) *Basic Configuration.*

The effect on C_L, C_m and tuft pattern of increasing the Reynolds number based on $\bar{c}$ from $1{\cdot}12 \times 10^6$ to $4{\cdot}33 \times 10^6$ is shown in Figs. 19 to 26.

At $R_{\bar{c}} = 1{\cdot}12 \times 10^6$, the stall is fairly gradual with a rounded peak to the lift curve at $\alpha = 12{\cdot}5^{\circ}$ (Fig. 19a). At this point there appears to be a region of flow separation near the trailing edge of the outboard wing (but excluding the tip), elsewhere, the flow is attached (Fig. 20a). As the incidence is increased between 12·5° and 14·0°, the separation spreads forward to the droop 'knuckle' and inboard to the fence but the flow at the tip remains attached. Over this incidence range a nose-up change in C_m occurs (Fig. 19b) accompanied by a loss of lift (Fig. 19a). As incidence is further increased, the flow breakdown spreads over the fence and moves progressively inboard, in addition the attached flow at the tip is reduced in extent and finally disappears. At $\alpha = 21{\cdot}7^{\circ}$, (Fig. 20f), attached flow is present only near the wing root. Between $\alpha = 15^{\circ}$ and 17°, a nose-down variation of C_m with α occurs (Fig. 19b), which is possibly associated with the start of flow separation inboard of the fence. Above 17° incidence a nose-up variation of C_m with α returns. C_L decreases continuously throughout this incidence range.

At $R_{\bar{c}} = 2{\cdot}24 \times 10^6$, the character of the stall has changed quite noticeably. The stalling incidence has increased to 14·27° but at incidences just below the stall, there is evidence (Figs. 22b and c) that the outboard trailing-edge separation is reduced in extent. In addition there is a region of quite strong outflow, just behind the droop 'knuckle' outboard of the fence. The starboard wing stalls first, with the flow separation occurring almost instantaneously outboard of the fence but with the tip remaining clear (Fig. 22c). By $\alpha = 14{\cdot}60^{\circ}$ the port wing has stalled, although here the separation does not extend quite as far as the fence (Fig. 22d). The force measurements (Fig. 21a and b) show a marked loss of lift and an abrupt nose-up pitching moment break at the stall. Above 15° incidence the stall resembles that at the lower Reynolds number, with a progressive inboard movement of the flow separation with increasing incidence (Fig. 22e and f). Between $\alpha = 15^{\circ}$ and 22° there is a nose-up variation of C_m with α (Fig. 21b), without the short range of nose-down variation present at the lower Reynolds number.

At $R_{\bar{c}} = 3{\cdot}36 \times 10^6$ (Figs. 23 and 24) and $4{\cdot}33 \times 10^6$ (Figs. 25 and 26) the nature of the stall is very similar to that at $R_{\bar{c}} = 2{\cdot}24 \times 10^6$ with very little outboard trailing edge separation just before the stall, but with marked outflow just outboard of the fence, behind the droop 'knuckle'. The stalling incidence increases with increasing $R_{\bar{c}}$ to 15·09° and 15·67° at $R_{\bar{c}} = 3{\cdot}36 \times 10^6$ and $4{\cdot}33 \times 10^6$ respectively, and the nose-up pitching moment break becomes even more pronounced at these higher Reynolds numbers. At $R_{\bar{c}} = 4{\cdot}33 \times 10^6$, between $\alpha = 19{\cdot}5°$ and $22{\cdot}0°$, with the flow separation having spread inboard to the fence, the flow, just outboard of the fence on the port wing, reattaches (Fig. 26e) giving a reduction in the nose-up pitching moment (Fig. 25b). The same feature is shown at $\alpha = 22{\cdot}35°$ in Fig. 26f although the corresponding value of C_m (0·194) appears to be consistent with separated flow. It is probable that $\alpha = 22{\cdot}35°$ represents the upper limit of the flow reattachment, and that the flow at this incidence was flicking between attachment and separation, with the tuft photograph taken when the flow was attached and the force measurement taken with the flow separated.

In order to explore more fully the flow over the wing just below the stall at the higher Reynolds numbers, an oil flow investigation was performed at $R_{\bar{c}} = 3{\cdot}36 \times 10^6$ and $\alpha = 14{\cdot}37°$. The stalling incidence at this Reynolds number is 15·09° for the wing with tufts and 14·45° for the wing without tufts (Fig. 30). The oil flow pattern (Fig. 27) shows clearly, regions of separation or near separation at the trailing edge of the outboard wing. Although the tufts did not show fully separated flow here, they did show some outflow, and it is clear that the flow is very close to separation with low values of skin friction and consequent lack of oil movement. The extensive regions of outflow outboard of the fence just behind the droop 'knuckle' is evident from the oil flow pattern.

Fig. 27b, which shows the detail on the starboard wing leading edge at wing section 'C', contains a very involved flow pattern. An accumulation of oil is visible just behind the leading edge which is thought to be due to a laminar separation bubble of the 'short' variety[7] (laminar boundary-layer separation followed by transition to turbulence and reattachment). Immediately inboard of wing section 'C', which corresponds to the joint in the drooped leading edge shown in the photograph (Fig. 27b), there is a large increase in the chordwise extent of the oil accumulation. Just outboard of this oil accumulation a region of reverse flow can be seen. The inboard boundary of this region of reverse flow is swept back at an angle of 25° relative to the leading edge, and shows the pattern of diverging streamlines associated with swept flow attachment lines[8]. At the outboard end of the region of reverse flow, the attachment line curves forward towards the leading edge. It is suggested that due to the reduced thickness of the profile on section 'C' and corresponding steeper pressure gradients at incidence, a short bubble type separation cannot exist here and the separated flow does not reattach until much further aft on the wing section in the manner of the long bubble separation which can occur on two-dimensional aerofoils. However, the resemblance of the present case to long bubble separation is superficial only, since the velocities within a long bubble are quite low and apart from some diffusion there is little interchange of fluid across the bubble surface[8]. In the present case the flow pattern which occurs ahead of the swept attachment line is clearly defined, and indicates that the leading-edge separation has formed a coiled vortex sheet in the manner of leading-edge separation on more highly swept wings[8]. Outboard of section 'C', where the wing profile has changed sufficiently to stabilize the short bubble separation, the coiled vortex sheet presumably leaves the surface and rolls up into a concentrated core of vorticity.

It is very probable that the strong outflow just behind the droop 'knuckle', outboard of the fence is produced by incipient separation of the turbulent boundary layer due to its development through two adverse pressure gradients (from leading edge and droop 'knuckle') aggravated by the increased circulation due to the outboard flap, and is not due to the coiled vortex sheet arising from the leading-edge separation on section 'C'. Unfortunately, the model was not tested with the leading-edge chin on section 'C' and without vortex generators, so direct experimental evidence has not been obtained on the sole effect of increasing the leading-edge radius on section 'C' and so eliminating the leading-edge separation. Figs. 28 and 29 show pitching moment curves and tuft patterns respectively for the stall of the final configuration at $R_{\bar{c}} = 3{\cdot}36 \times 10^6$. Here the stall occurs over the outboard wing, although the outflow is not present behind the droop 'knuckle', outboard of the fence due to the beneficial effects of the vortex generators on the boundary layer. Although both basic and final configurations stall at the same incidence, there are significant differences in the initial part of the stall. For the basic configuration, flow breakdown occurs instantaneously over almost the entire wing outboard of the fence, producing an abrupt nose-up pitching moment break (Figs. 23 and 24). For the final configuration, flow breakdown begins on the port wing at the third row of tufts outboard of the fence (Fig. 29b), and its extent spreads fairly slowly until at $\alpha = 15{\cdot}85°$ (Fig. 29d) it covers the wing, from just inboard of the fence to roughly halfway between the fence and the tip.

It would seem then, that at Reynolds numbers above $2{\cdot}24 \times 10^6$ there are two potential sources of separation, the leading-edge separation on section 'C' and associated coiled vortex sheet which gives a progressive stall, and turbulent boundary-layer separation occurring just behind the droop 'knuckle' and producing an abrupt stall. On the basic configuration the latter occurs before the leading-edge separation has time to develop significantly, whereas on the final configuration, where the vortex generators suppress the turbulent separation, the stall is of the former type.

Summarizing the results of the basic configuration, we have then, a fairly gradual stall at $R_{\bar{c}} = 1{\cdot}12 \times 10^6$ due to trailing-edge separation on the outboard wing extending forwards to the droop 'knuckle'. Increasing $R_{\bar{c}}$ to $2{\cdot}24 \times 10^6$ or more has a beneficial effect in suppressing this trailing-edge separation. Because of the higher incidences attained and the consequently steeper adverse pressure gradients existing behind the leading edge and the droop 'knuckle', separation of the turbulent boundary layer occurs just behind the droop knuckle producing a very abrupt stall, again over the outboard wing. At all Reynolds numbers a nose-up pitching moment break occurs at the stall. It should be noted that even if further increase in Reynolds numbers, to values higher than those attained in the present tests, had a beneficial effect in suppressing the turbulent separation behind the droop 'knuckle', stall would in all probability, still be unrepresentative of full scale, in that it would be initiated by the leading-edge separation arising from wing section 'C', and that a nose-up pitching-moment break would still occur. The effect of different Reynolds numbers on the variation of C_L and C_m with α is summarized in Fig. 30 for the basic configuration *without* tufts.

(b) *Final configuration with leading-edge chin.*

At $R_{\bar{c}} = 1{\cdot}12 \times 10^6$, the nature of the stall, as shown by the lift and pitching-moment measurements (Fig. 31) and the tuft patterns (Fig. 32), is very similar to the basic configuration at the same Reynolds number (Figs. 19 and 20). The flow breakdown again occurs first over the outboard wing and spreads inboard to the root with increasing incidence (Fig. 32). Consequently, the post stall variation of C_m with α (Fig. 31b) displays the same form as for the basic configuration (Fig. 19b). The inference to be drawn from this result is that the vortex generators are relatively ineffective at this Reynolds number in suppressing the trailing-edge separation.

At $R_{\bar{c}} = 2{\cdot}24 \times 10^6$, and just below the stall, there is no sign of the outflow just behind the droop 'knuckle' outboard of the fence which occurs on the basic configuration. The initial part of the stall is again fairly gradual with separation first occurring on the outboard starboard wing at $\alpha = 15{\cdot}72°$ (Fig. 34b). Simultaneously, the beginning of an inboard wing stall is shown by flutter of the first row of tufts inboard of the fence. At this point the lift curve has reached a fairly rounded peak and the pitching-moment curve is showing a gradual nose-up variation. By $\alpha = 16{\cdot}18°$ (Fig. 34c), the inboard wing stall has spread to 3 rows of tufts on the starboard wing whereas the outboard wing separation has reattached resulting in an abrupt nose-down pitching-moment break. At $\alpha = 17{\cdot}26°$ (Fig. 34d), the flow separation inboard of the fence has spread roughly half way to the root giving a further nose-down change in pitching moment. Separation over the entire starboard wing outboard of the fence occurs at $\alpha = 17{\cdot}56°$ (Fig. 34e). At the same time the extent of the inboard separation on the starboard wing is reduced. A second nose-up pitching-moment break occurs at this incidence. At incidences of 16·0° to 16·5° and again at 17·5° to 18·0°, where the abrupt changes in C_m occur, it was observed that the stall would often flick from inboard to outboard and *vice versa*. Further increase of incidence causes the port outboard wing to stall with an additional increase in the nose-up pitching moment.

At $R_{\bar{c}} = 3{\cdot}36 \times 10^6$ the wing stall has changed entirely in character. Although there is a slight outflow near the trailing edge of the outboard wing, flow breakdown first occurs just inboard of the fence at

$\alpha = 16{\cdot}73°$ (Fig. 36b), and rapidly spreads inboard to the root over one wing. The lift and pitching-moment measurements (Fig. 35) show clearly C_L and C_m 'breaks' of $-0{\cdot}16$ and $-0{\cdot}03$ respectively due to one wing stalling at $\alpha = 16{\cdot}8°$ closely followed at $\alpha = 17{\cdot}4°$ by additional C_L and C_m breaks of the same size due to the other wing stalling. As at $R_{\bar{c}} = 2{\cdot}24 \times 10^6$, however, the stalls were intermittent in nature at the above incidences with flicking between the stalled and unstalled conditions and *vice versa.* In particular, Fig. 36d, shows only one wing stalled whereas the force measurements clearly show both wings stalled. Fig. 36d also shows a stall only on the starboard wing whereas Fig. 36c shows a stall only on the port wing, indicating that the change-over from two wings stalled to one wing stalled can occur on either side. At 20·2° incidence the inboard wing stall is firmly established on both port and starboard wings, and the tufts just outboard of the fence show signs of a disturbance (slight outflow combined with unsteadiness) originating from section 'C' (Fig. 36e). By $\alpha = 21{\cdot}15°$ the entire starboard wing outboard of the fence has stalled, coupled with a slight reduction in extent of the flow breakdown inboard of the fence on the starboard wing (Fig. 36f). A substantial nose-up change in C_m occurs at this point (Fig. 35b).

At $R_{\bar{c}} = 4{\cdot}33 \times 10^6$ (Figs. 37 and 38), the results are much the same as at $R_{\bar{c}} = 3{\cdot}36 \times 10^6$ except that here the flow breakdown over the outboard wing is delayed to incidences above the range of the present tests (22°).

Comparison of the oil flow pattern obtained at $R_{\bar{c}} = 3{\cdot}36 \times 10^6$ and $\alpha = 14{\cdot}42°$ for the final configuration with leading-edge chin (Fig. 39a), with that obtained at the same Reynolds number and $\alpha = 14{\cdot}37°$ for the basic configuration (Fig. 27a), clearly shows the beneficial effect of the vortex generators in suppressing trailing-edge separation on the outboard wing. A detailed view of the oil flow pattern near the leading-edge of section 'C' on the port wing (Fig. 39b), shows that the leading-edge chin has effectively eliminated the leading-edge separation which was present on the basic configuration (Fig. 27b). The strong outflow just behind the droop 'knuckle', outboard of the fence, which was evident in the oil flow pattern on the basic configuration (Fig. 27), does not occur in the oil flow pattern shown in Fig. 39 nor in the tuft patterns (Figs. 34, 36 and 38).

A second oil flow pattern was obtained on the final configuration with leading-edge chin at $R_{\bar{c}} = 3{\cdot}36 \times 10^6$ and $\alpha = 16{\cdot}44°$ (stalling incidence, with or without tufts 16·73°). Here, the extent of outboard wing trailing-edge separation or near separation has increased in extent (Fig. 40a), and in the detail view (Fig. 40b) can be seen two vortex sheets originating from leading-edge separations at either end of the chin on section 'C'. Although these separations do not initiate a stall on this configuration, clearly the chin is only partially effective in suppressing leading-edge separation at this incidence, and it is probable that the error in section shape extends over a greater length of the leading edge than that covered by the chin.

In summarizing the results for the final configuration with leading-edge chin we may conclude that the addition of the vortex generators has virtually no effect on trailing-edge separation at $R_{\bar{c}} = 1{\cdot}12 \times 10^6$, and the stall is identical to that on the basic configuration, i.e. a nose-up pitching-moment break occurs due to flow breakdown over the outboard wing. At $R_{\bar{c}} \geqslant 3{\cdot}36 \times 10^6$, the vortex generators have suppressed the turbulent separation occurring just behind the droop knuckle, outboard of the fence on the basic configuration, and the leading-edge chin has eliminated the leading-edge separation occurring on section 'C'. (Implying that the correct profile on section 'C' would also eliminate the leading-edge separation.) Flow breakdown first occurs over the inboard wing giving a nose-down pitch break. In other words, with a configuration which is representative of the aircraft, the type of stall occurring full scale has been obtained. The variation of C_L and C_m with α at different Reynolds numbers for the final configuration with leading-edge chin and without tufts is summarised in Fig. 41.

5.2. *Effect of Mach Number on the Stall Development of the Final Configuration with Leading-Edge Chin.*

At $R_{\bar{c}} = 1{\cdot}12 \times 10^6$, changes in Mach number within the range 0·15 to 0·30 have no marked effect on the lift curves (Fig. 42a). There are, however, noticeable changes in the shape of the pitching-moment curves (Fig. 42b) for Mach numbers above 0·2. The initial nose-up pitching-moment break occurs at the same incidence (13·5°) at all Mach numbers, but at $M = 0{\cdot}25$ and 0·30 it is reduced in size, and occurs more abruptly. Due to excessive buffeting of the model, no measurements were made beyond $\alpha = 15{\cdot}5°$ at $M = 0{\cdot}30$. However, measurements were made on the configuration with tufts up to an incidence of 22° and here the measured pitching-moment coefficients, although showing the abrupt nose-down change which occurs at $\alpha = 14{\cdot}5°$, did not fall below a value of 0·02 (adjusted for the slight difference in basic C_m level for the configurations with and without tufts), and for incidences above 15·5° showed a nose-up variation with increasing incidence. The reasons for the discrepancy in C_m level at $\alpha = 15{\cdot}5°$ between the two cases, with and without tufts, are not clear, but it is expected that both cases would show similar variations of C_m with α for $\alpha > 15{\cdot}5°$.

At $R_{\bar{c}} = 2{\cdot}24 \times 10^6$, decreasing Mach number has a very favourable effect on $C_{L\max}$ (Fig. 43) and of more importance, at $M = 0{\cdot}15$, a nose-down pitching-moment break occurs at the stall, in contrast to the nose-up pitching-moment breaks occurring at the other Mach numbers. Unfortunately, no tuft photographs were obtained at this condition so that the actual nature of the flow breakdown is not known. However, this result would seem to indicate that the turbulent separation which occurs just behind the droop 'knuckle' at $R_{\bar{c}} > 2{\cdot}24 \times 10^6$ is Mach-number sensitive. Presumably increasing the Mach number causes the adverse pressure gradients to become more pronounced.

5.3. *Maximum Lift Coefficient.*

For all configurations a marked gain in $C_{L\max}$ occurs at $M = 0{\cdot}2$ with increasing Reynolds number, by virtue of the higher values of α at which flow breakdown occurs (Fig. 44a). For the basic configuration a rise of 0·16 in $C_{L\max}$ occurs when $R_{\bar{c}}$ is increased from $1{\cdot}12 \times 10^6$ to $3{\cdot}36 \times 10^6$. As shown in Section 5.1(a) this follows from the beneficial effect of increasing Reynolds number on the outboard wing trailing edge separation and on the turbulent separation occurring behind the droop 'knuckle', outboard of the fence. Increasing $R_{\bar{c}}$ from $1{\cdot}12 \times 10^6$ to $4{\cdot}33 \times 10^6$ produces an improvement of 0·290 in $C_{L\max}$ (from 1·615 to 1·905) for the final configuration with leading-edge chin. Here the increase arises from the effect of Reynolds number on the inboard wing stall. For the final configuration, the increase in $C_{L\max}$ is slightly less at 0·240, and in general $C_{L\max}$ for the final configuration is always slightly less than that for the final configuration with leading edge chin, due to the leading edge separation occurring at section 'C' with the former. Even at the highest Reynolds number of the tests, $R_{\bar{c}} = 4{\cdot}33 \times 10^6$, $C_{L\max}$ is still rising with increasing Reynolds number for all configurations. Maximum $C_{L\max}$ achieved with the aircraft is of the order of 1·95 and it would seem that the final configuration with leading-edge chin could reach this sort of value by $R_{\bar{c}} = 6 \times 10^6$.

Changes in Mach number over the range 0·15 to 0·30 have no effect on $C_{L\max}$ for the final configuration with leading-edge chin at $R_{\bar{c}} = 1{\cdot}12 \times 10^6$, although there is a slight decrease in $C_{L\max}$ with increasing Mach number for the final configuration (Fig. 44b). It follows that the outboard wing trailing-edge separation occurring at this Reynolds number is insensitive to Mach number changes within the range 0·15 to 0·30. At $R_{\bar{c}} = 2{\cdot}24 \times 10^6$, Mach number has a very pronounced effect on $C_{L\max}$. For the final configuration with leading-edge chin, $C_{L\max}$ decreases from 1·875 at $M = 0{\cdot}15$ to 1·680 at $M = 0{\cdot}30$, and for the final configuration it remains constant at 1·765 between $M = 0{\cdot}15$ and 0·20 before decreasing to 1·675 at $M = 0{\cdot}30$. This type of variation with Mach number, with the rate of decrease with increasing Mach number diminishing as Mach number increases, has been reported by several authors[9,10,11]. In particular, Furlong and Fitzpatrick[9] show that both maximum peak suction pressure coefficient and maximum $C_{L\max}$ occur when the former has reached the critical pressure coefficient.

5.4. *Flight-Tunnel Comparison of the Stall Development.*

Details of a typical stall development on the aircraft is shown in Fig. 45a. The source of this data is an unpublished Hawker-Siddeley flight-test report (flight 111 on G-ARPC). The Mach number and Reynolds number of the flight test were approximately 0·20–0·21 and 14×10^6–15×10^6 respectively. The aircraft configuration differs significantly from the present model (final configuration with leading-edge chin) only in that the undercarriage was lowered. It is thought that this feature would not seriously modify the upper surface flow breakdown at the stall. Although a small region of flow breakdown occurs inboard of the fence at $\alpha = 10°$, it does not noticeably increase in extent up to $\alpha = 14°$. The major part of the flow breakdown occurs between $\alpha = 16°$ and 18°. The outboard wing remains free from separation up to 18° incidence.

On the model, at $R_{\bar{c}} = 4{\cdot}33 \times 10^6$, localized regions of flow separation occur inboard of the fence between 15° and 17° incidence with the main spread of the flow separation boundary taking place between 17° and 20° incidence (Fig. 45b).

Although the shape of the separation boundary on the model is different to that at full scale during the main spread of the stall, the values of the incidence at which the main spread of the stall is initiated, 16° full scale and 17° model scale, are in quite close agreement, and in both cases the flow breakdown reaches the fuselage side after a further 2·5° to 3° increase in incidence. The outflow present on the model near the trailing edge of the outboard wing at 20° incidence would probably be eliminated by increasing the Reynolds number to the full scale value. Thus at the maximum Reynolds number of the present tests ($R_{\bar{c}} = 4{\cdot}33 \times 10^6$) quite good agreement has been obtained between the stall development, as shown by the separation boundaries, on the present model and full scale.

6. *Conclusions.*

An investigation has been made of the independent effects of Reynolds number and Mach number on the low-speed stalling characteristics of a model of the Trident 1C. The investigation covered a range of Reynolds number based on $\bar{c}$ from $1{\cdot}12 \times 10^6$ to $4{\cdot}33 \times 10^6$, with a Mach number range extending from 0·15 to 0·30.

The results obtained effectively demonstrate the importance of testing models at sufficiently high Reynolds numbers, and of the necessity of separating Reynolds number effects from Mach number effects, if realistic values of $C_{L\max}$ are to be obtained in tunnel tests, and if the full scale type of stall development is to be reproduced at model scale.

Experience with the model showed that flow breakdown at the stall was very sensitive to the wing profile shape at the leading edge. In this type of test therefore, it is essential to ensure that the wing profile shape is correctly represented on the model, in order that the type of stall occurring full scale shall occur on the model.

On the present model, the stall development at $M = 0{\cdot}2$ and $R_{\bar{c}} = 4{\cdot}33 \times 10^6$ is very similar to that on the aircraft at the same Mach number and $R_{\bar{c}} = 14{\cdot}5 \times 10^6$.

LIST OF SYMBOLS

b	Wing span
C_L	Lift coefficient $-\dfrac{\text{Lift}}{qS}$
$C_{L\max}$	Maximum value of C_L
C_m	Pitching-moment coefficient $-\dfrac{\text{Pitching moment}}{qS\bar{c}}$
$\bar{c}$	Standard mean chord
M	Mach number
$R_{\bar{c}}$	Reynolds number based on $\bar{c}$
q	Kinetic pressure
S	Wing area
s	Exposed wing semi-span (outboard of root rib datum)
x	Distance aft—usually measured from wing leading edge parallel to fuselage centreline
y	Distance outboard from root-rib datum
z	Height above wing horizontal datum or undrooped leading edge
α	Model incidence relative to fuselage centreline in degrees
α_W	Wing local incidence (angle of twist) measured relative to fuselage centreline
$\Delta\alpha_W$	Wing twist error—difference between model and aircraft wing twist
$\Delta\alpha_T$	Induced incidence in degrees along wing leading edge due to tunnel constraint
$\delta\alpha_T$	Mean value of $\Delta\alpha_T$

REFERENCES

No.	*Author(s)*	*Title, etc.*
1	D. A. Kirby and D. J. Kettle	Low speed tunnel tests on the effects of tailplane and nacelle position on the super-stall characteristics of transport aircraft. Unpublished Mintech Report.
2	R. T. Taylor and E. J. Ray	A systematic study of the factors contributing to post-stall longitudinal stability of T-tail transport configurations. A.I.A.A. Paper No. 65–737, May 1965.
3	R. S. Shevell and R. D. Schaufele	Aerodynamic design features of the DC-9. A.I.A.A. Paper No. 65–738, November 1965. *Jour. of Aircraft*, Vol. 3, No. 6, November-December 1966, pp. 515–523.
4	R. C. Montgomery and M. T. Moul	Analysis of deep-stall characteristics of T-tailed aircraft configurations and some recovery procedures. A.I.A.A. Paper No. 66–13, January 1966. *Jour. of Aircraft*, Vol. 3, No. 6, November-December, 1966, pp. 562–566.
5	W. E. A. Acum	Corrections for symmetrical swept and tapered wings in rectangular wind tunnels. A.R.C., R. & M. 2777 (1950).
6	E. C. Maskell	A theory of the blockage effects on bluff bodies and stalled wings in a closed wind tunnel. A.R.C., R. & M. 3400 (1963).
7	I. Tani	Low speed flows involving bubble separations. Progress in Aeronautical Sciences, Vol. 5, pp. 70–103 (1964).
8	E. C. Maskell	Flow separation in three dimensions. R.A.E. Report Aero 2565 (A.R.C. 18063) (1955).
9	G. C. Furlong and J. E. Fitzpatrick	Effects of Mach number and Reynolds number on the maximum lift coefficient of a wing of NACA 230-series airfoil sections. NACA TN No. 1299 (1947).
10	M. Cooper and P. F. Korycinski	The effects of compressibility on the lift, pressure and load characteristics of a tapered wing of NACA 66-series airfoil sections. NACA TN No. 1697 (1948).
11	G. C. Furlong and J. E. Fitzpatrick	Effects of Mach number up to 0·34 and Reynolds number up to 8×10^6 on the maximum lift coefficient of a wing of NACA 66-series airfoil sections. NACA TN No. 2251 (1950).

TABLE 1

Principal Dimenions of the Model.

Model scale = 1/18·86

Wing area (S)*	550·08 sq in
Wing span (b)	57·156 in
Wing standard mean chord ($\bar{c} = S/b$)	9·629 in
Wing aspect ratio ($A = b^2/S$)	5·933
Wing taper ratio†	0·2709
Sweepback of leading edge, inboard of section 'C'	38·84°
Sweepback of leading edge outboard of section 'C'	38·12°
Sweepback of trailing edge, inboard of section 'C'	3·93°
Sweepback of trailing edge outboard of section 'C'	24·09°
Sweepback of $\frac{1}{4}$ chord line, outboard of section 'C'	35·00°
Leading-edge droop angle	26°
Trailing-edge flap setting, starboard inboard	49·17°
Trailing-edge flap setting starboard outboard	50·67°
Trailing-edge flap setting port inboard	49·67°
Trailing-edge flap setting port outboard	50·17°
Fuselage diameter	7·714 in
Tailplane-setting angle	−5·67°
Location of wing horizontal datum below fuselage centreline	1·724 in
Location of root rib datum out from fuselage centreline	3·735 in
Location of moment reference centre (0·3 $\bar{c}$) behind wing transverse datum	9·346 in

*The wing area S is defined by the leading and trailing edges between the tip and the root rib datum (Fig. 3), plus the rectangle defined by the port and starboard root rib datums and the lines joining their leading and trailing edges.

†The taper ratio is defined as the ratio of the tip chord and the root rib datum chord.

TABLE 2

Wing Section Design Details to Model Scale (1/18·86)

Section	Distance out from root rib datum (inches)	Chord length (inches)	Thickness/ chord percentage	Leading edge height above wing horizontal datum (inches)	Trailing-edge height above wing horizontal datum (inches)	Wing local incidence relative to fuselage centreline (jig twist) (degrees)	Location of hinge line aft undrooped leading edge (inches)	Location of hinge line above undrooped leading edge (inches)
A	4·242	12·266	10·509	−0·026	−0·649	2·91	1·324	−0·620
B	7·212	10·079	10·616	−0·044	−0·384	1·93	1·196	−0·470
C	10·641			−0·065			0·841	−0·316
D	12·421	8·361	9·526	0·031	−0·004	0·24	0·992	−0·239
E	16·453	7·000	9·607	0·256	0·293	−0·30	0·873	−0·148
F	22·359	5·008	9·813	0·673	0·729	−0·64	0·698	−0·101
G (Wing tip)	24·843	4·169	9·973	0·849	0·912	−0·87	0·624	−0·082

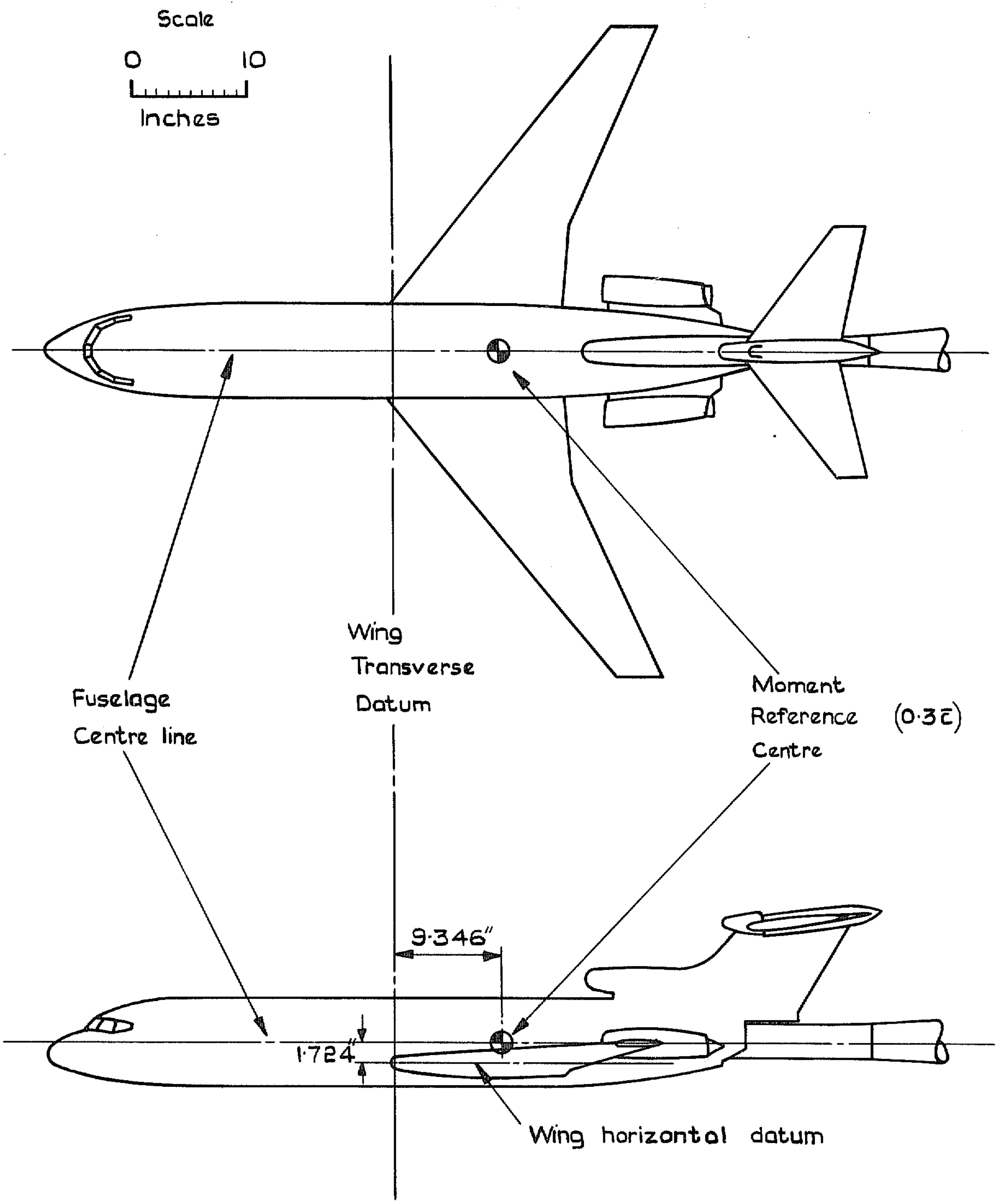

(N.B wing planform and side elevation only shown here, for details of leading edge droop, trailing edge flaps etc., see fig 3)

FIG. 1. General arrangement of model.

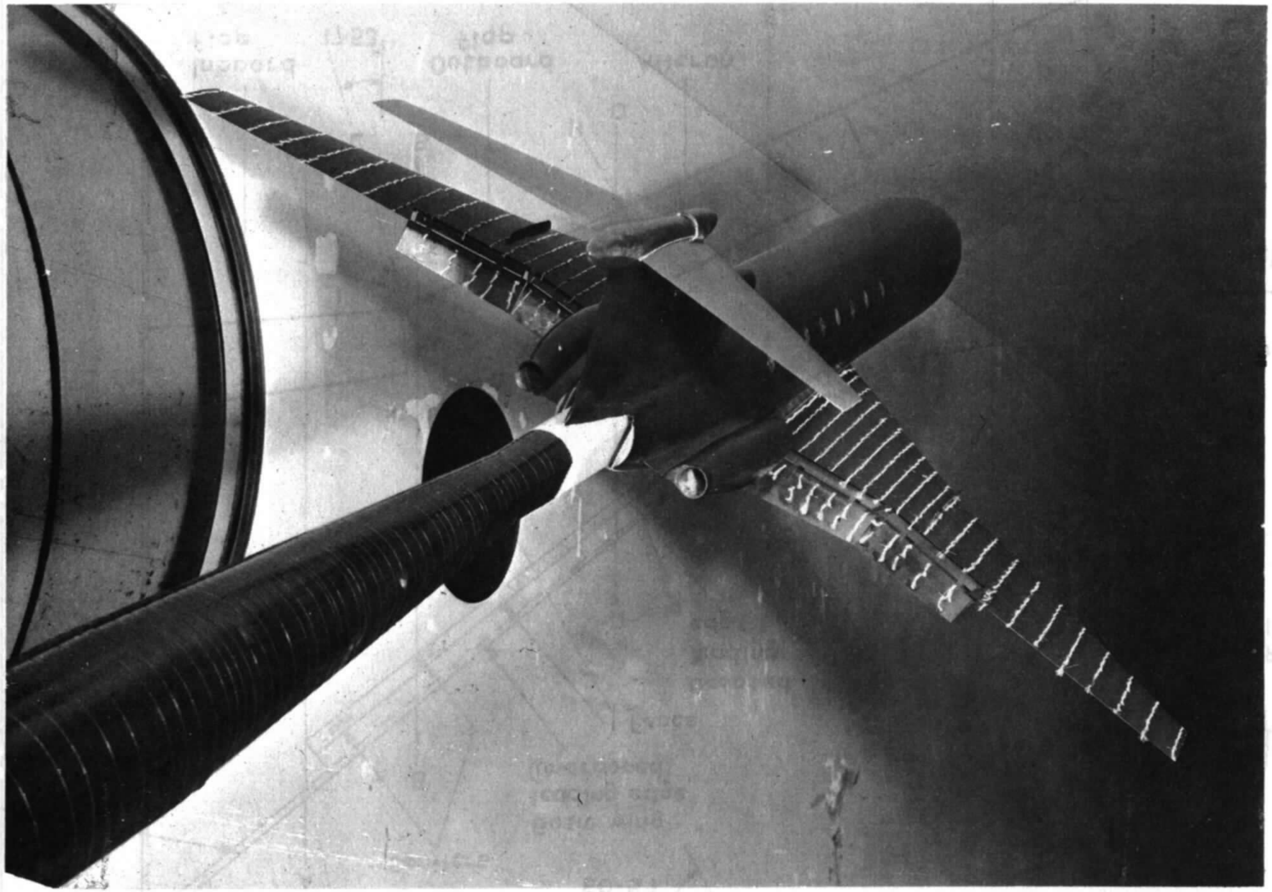

FIG. 2. View of model in working section of 8 ft × 8 ft tunnel.

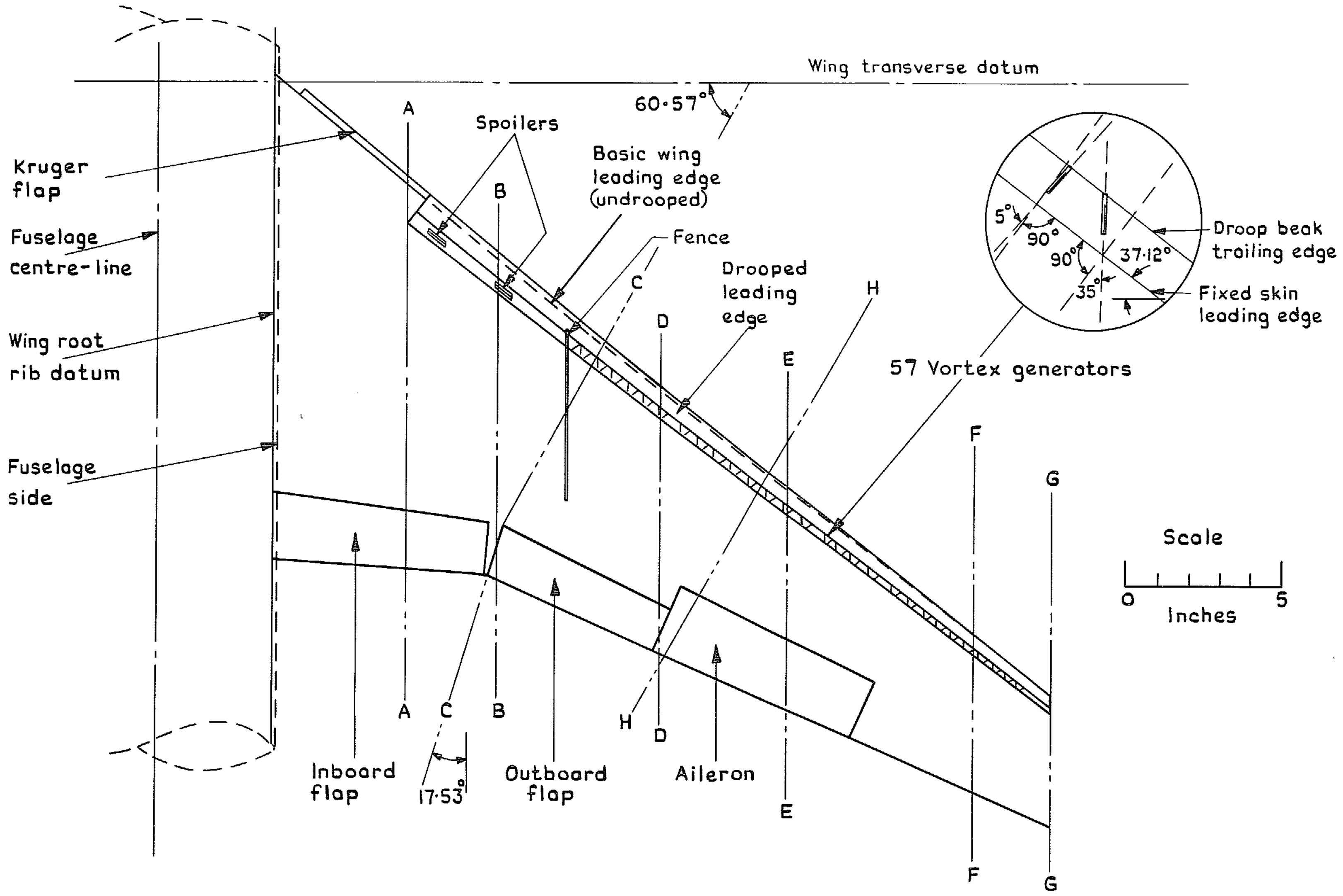

FIG. 3. Wing details.

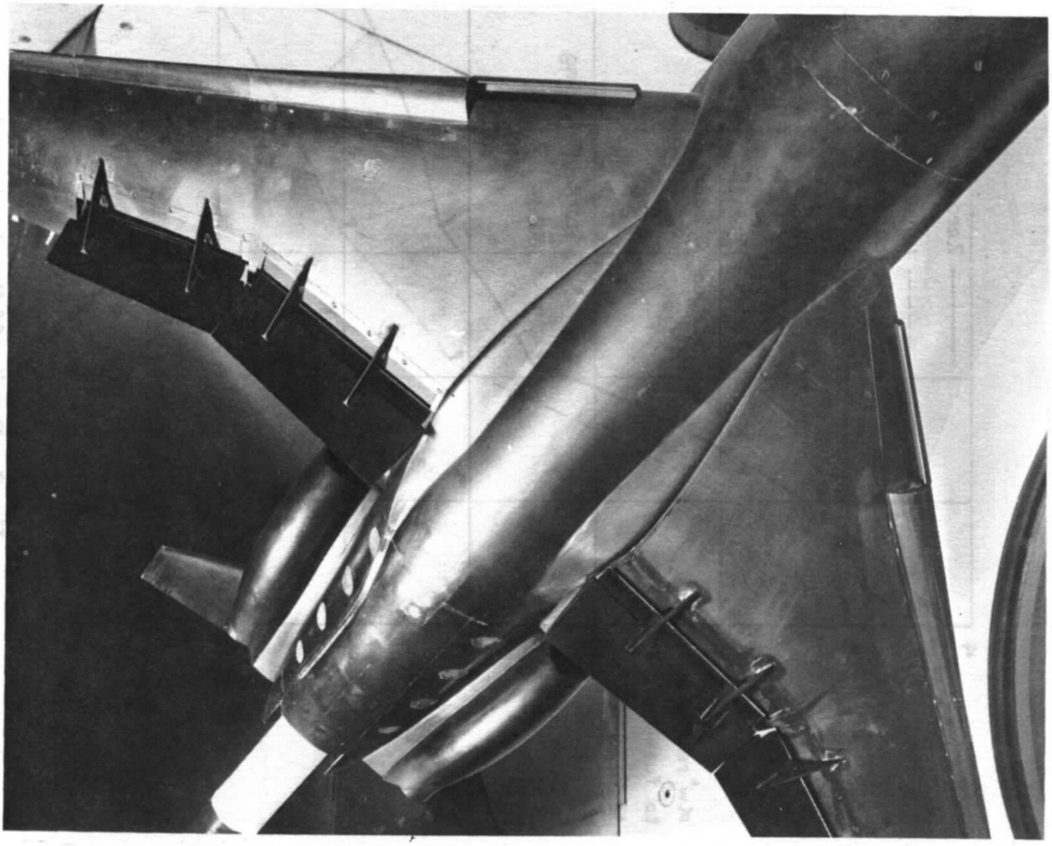

FIG. 4. Wing under surface details.

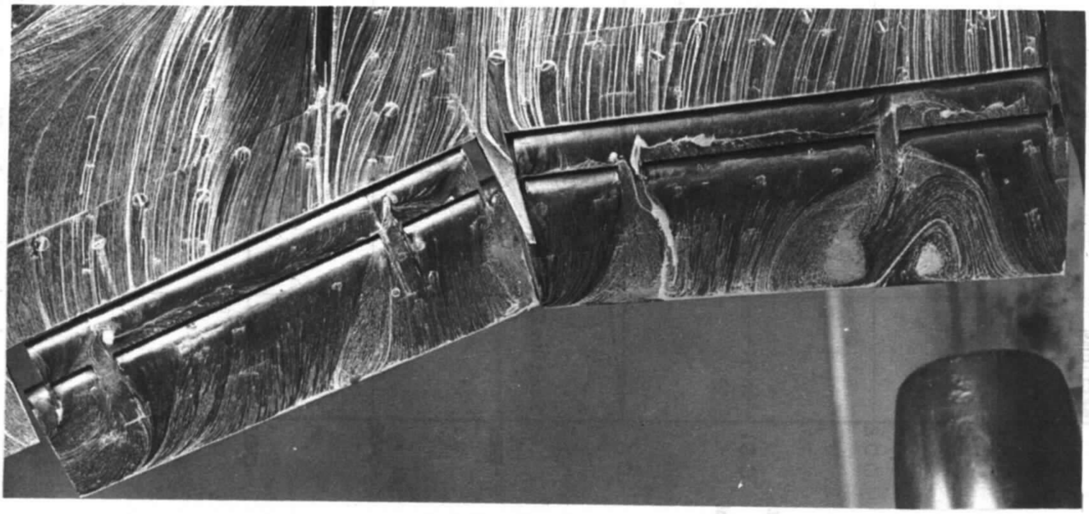

FIG. 5. Flap upper surface details.

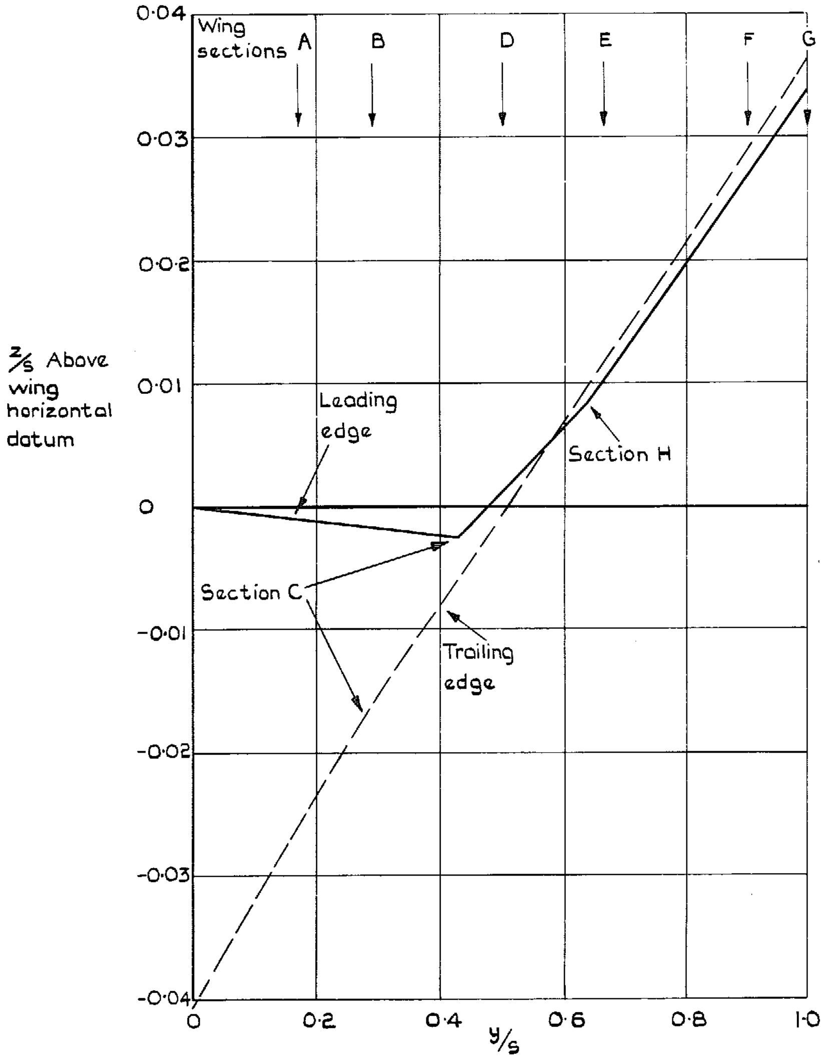

FIG. 6. Full scale height location of unloaded wing leading and trailing edges (zero g shape).

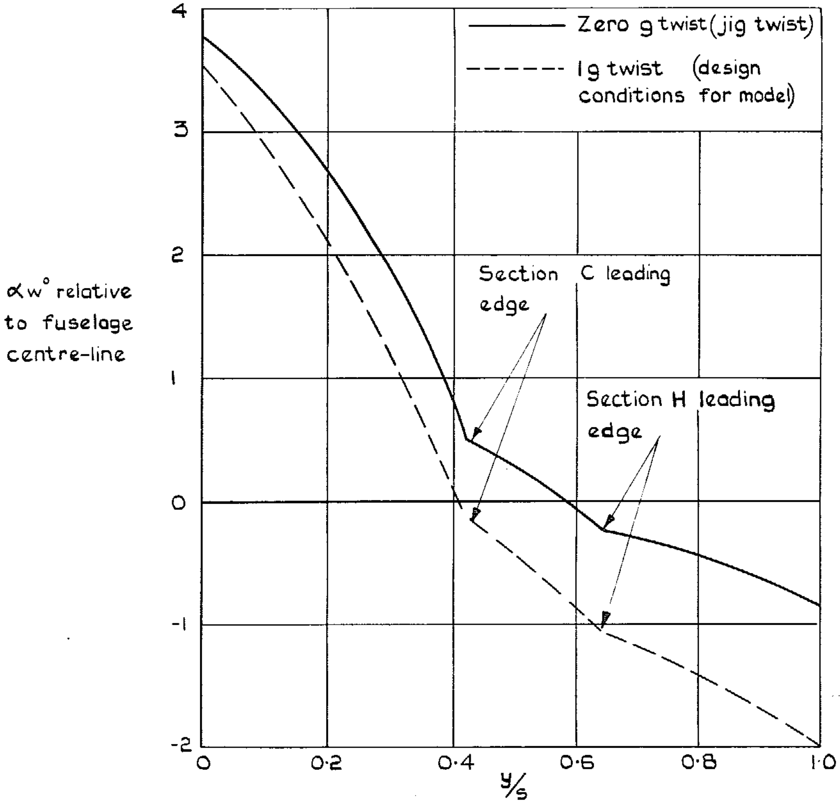

FIG. 7. Details of full scale wing twist.

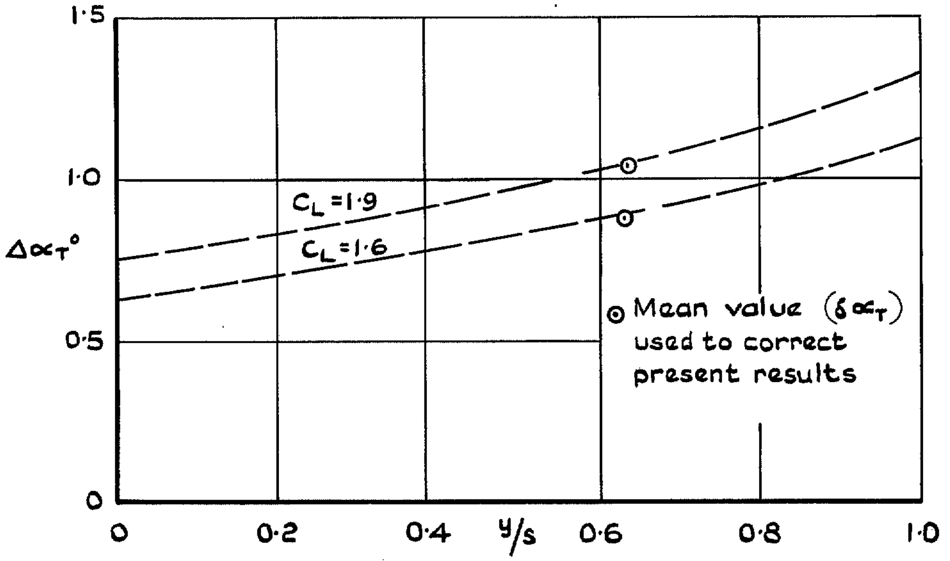

FIG. 8. Aerodynamic twist due to tunnel constraint (ref. 5).

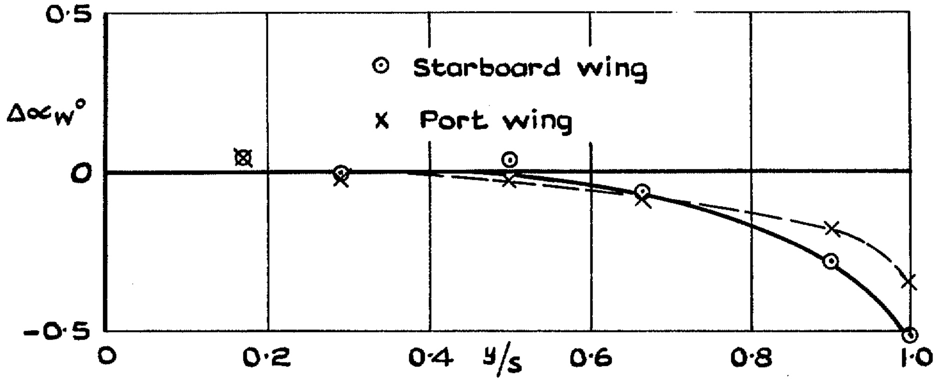

(a) Geometrical twist error

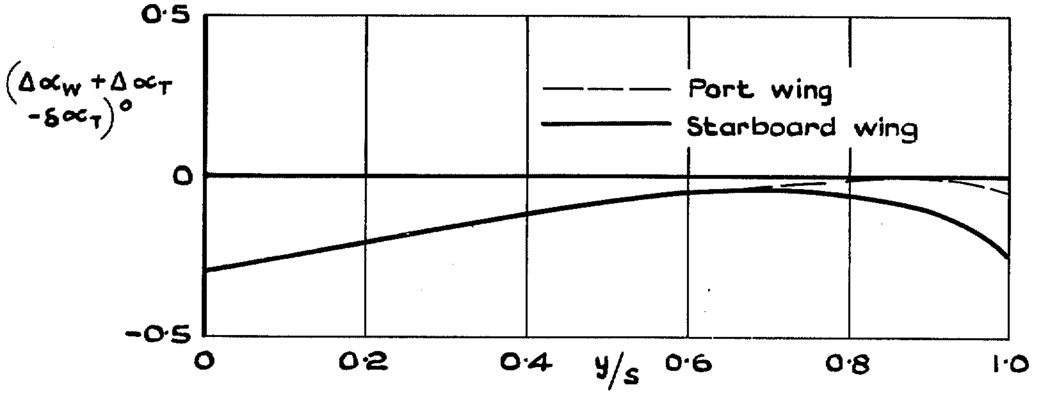

(b) Total twist error (geometrical + aerodynamic) $C_L = 1·9$

FIG. 9a & b. Model wing twist error.

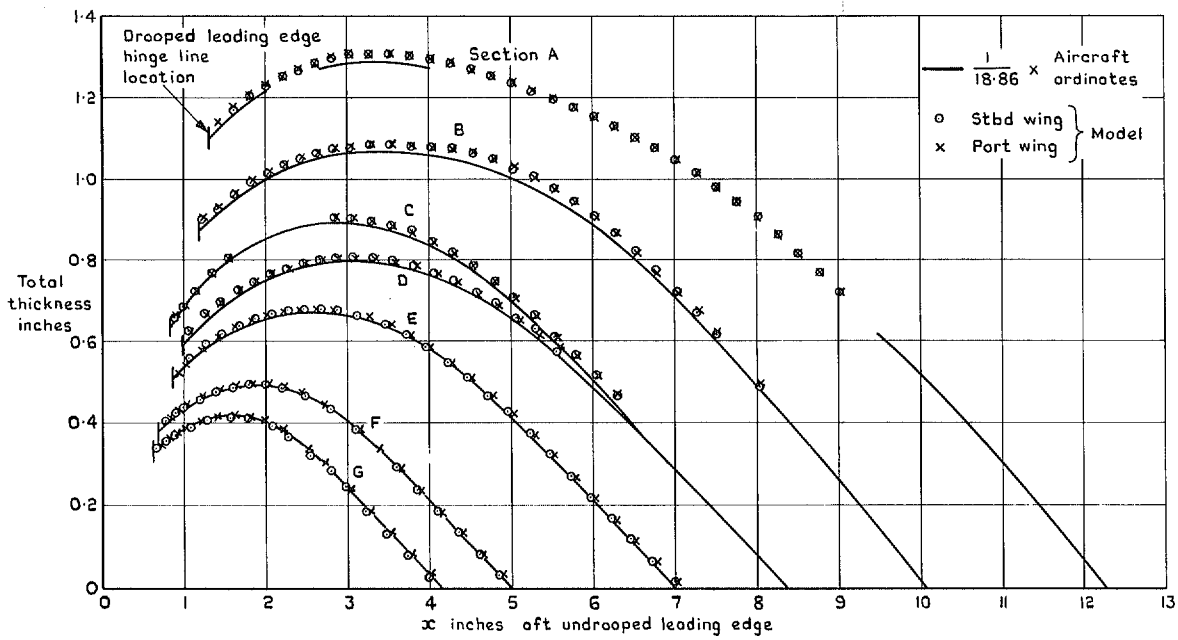

FIG. 10. Wing section thickness aft of leading edge hinge line.

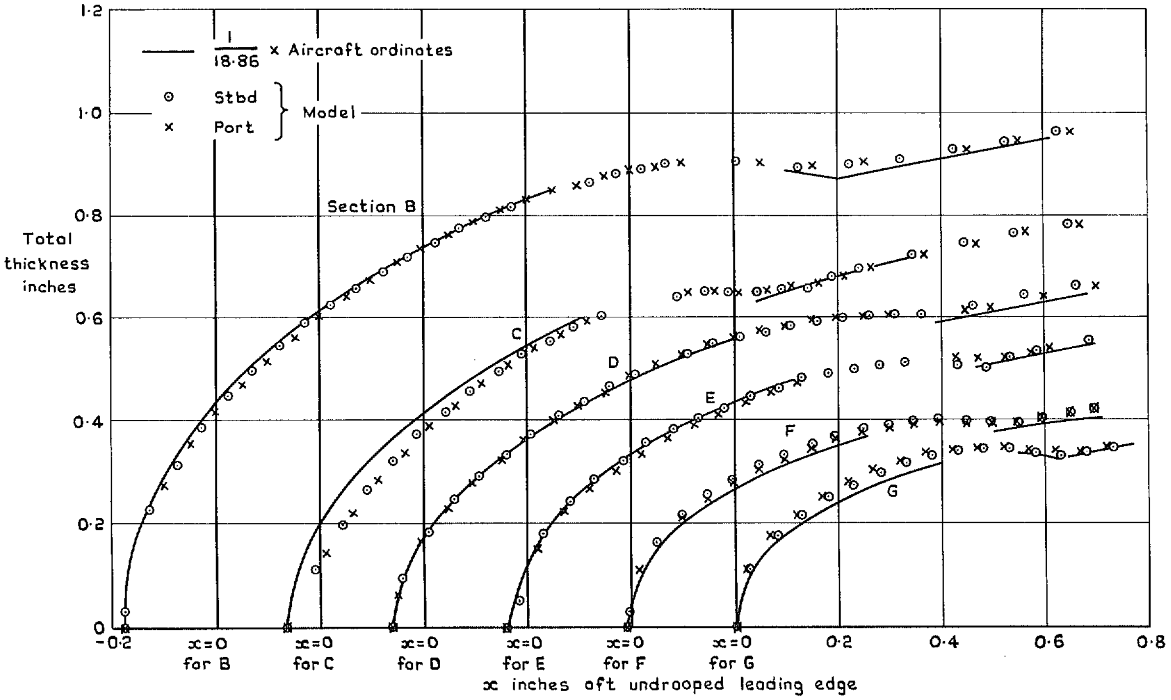

FIG. 11. Wing leading edge thickness.

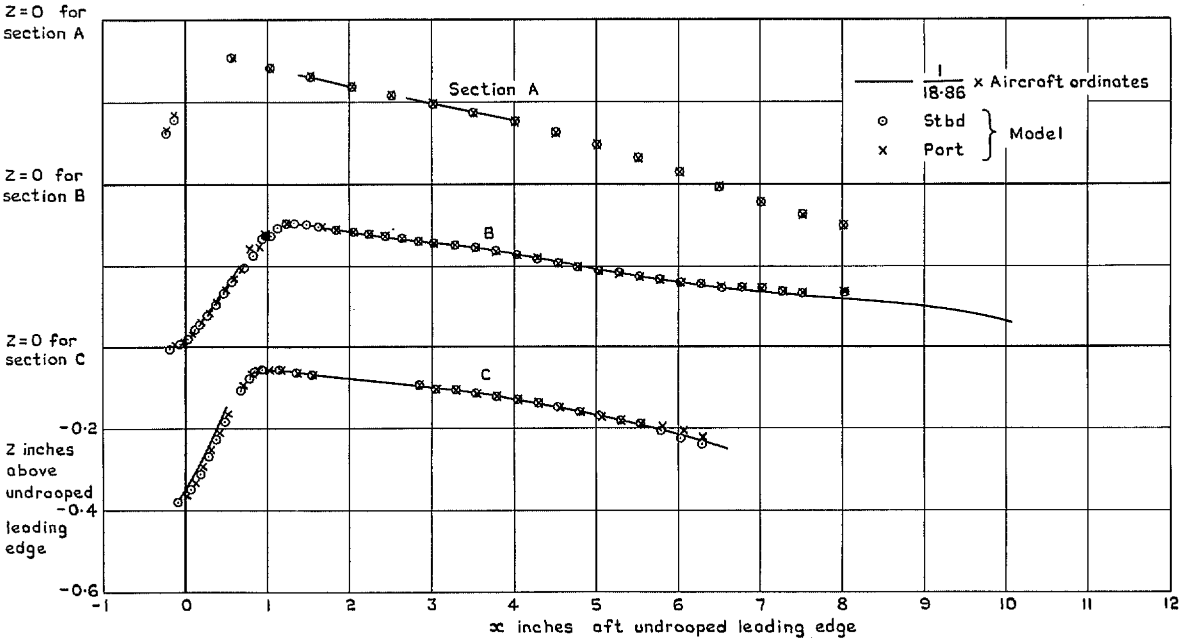

FIG. 12. Wing camber lines.

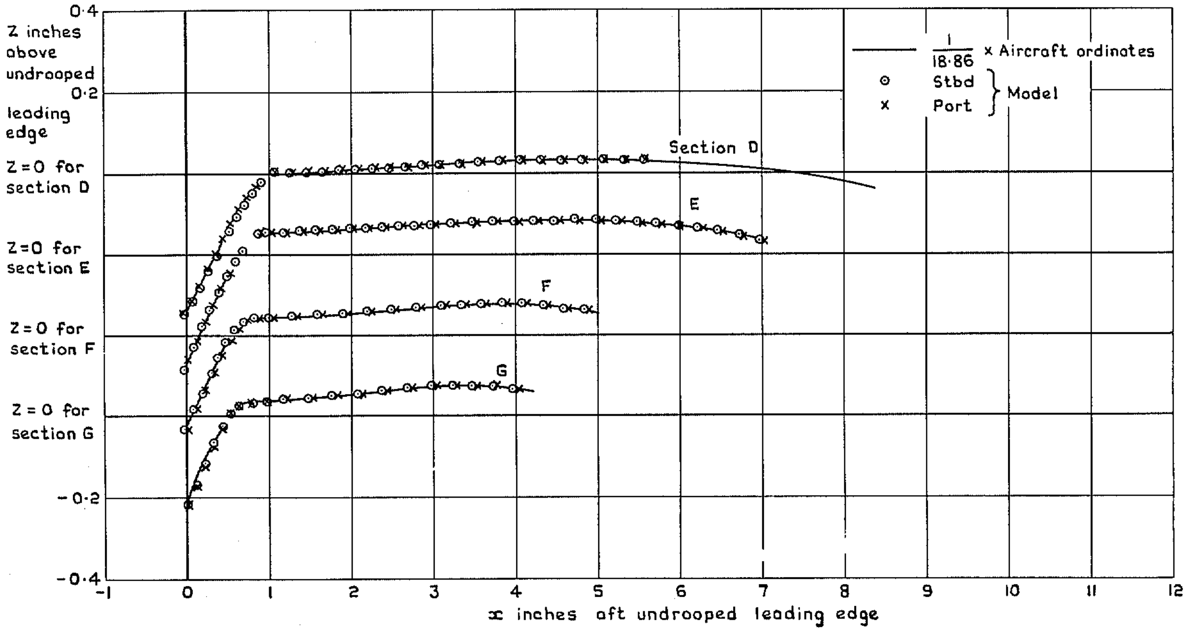

FIG. 12 *concld.* Wing camber lines.

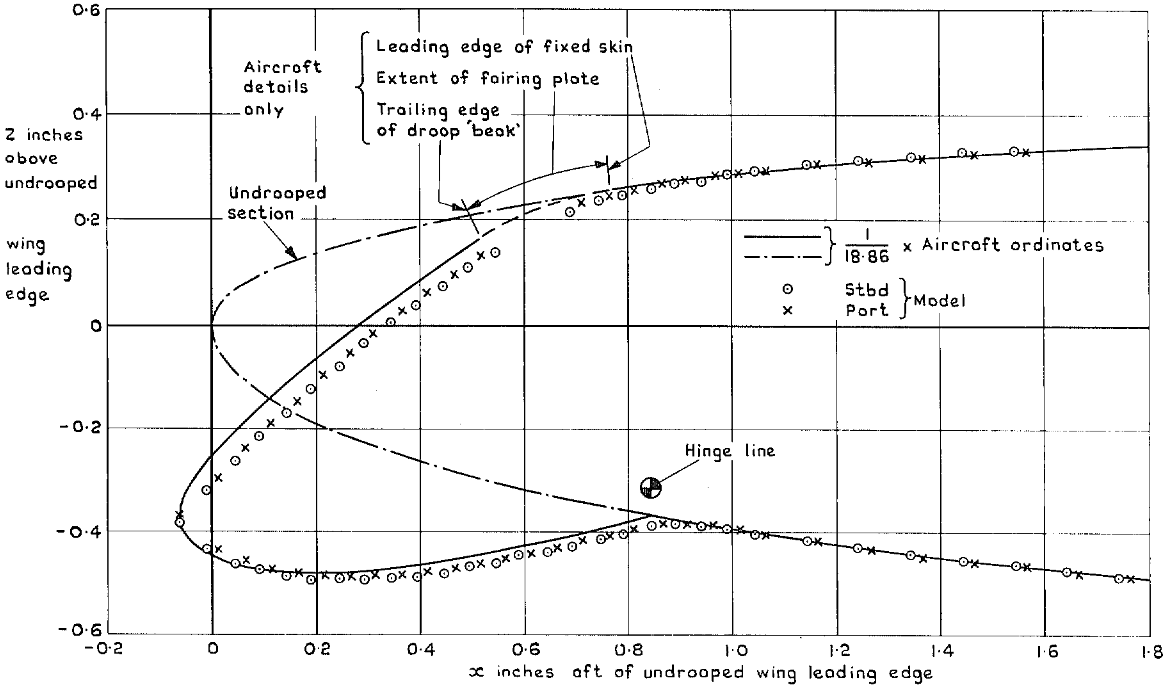

FIG. 13. Wing leading edge profile; section C.

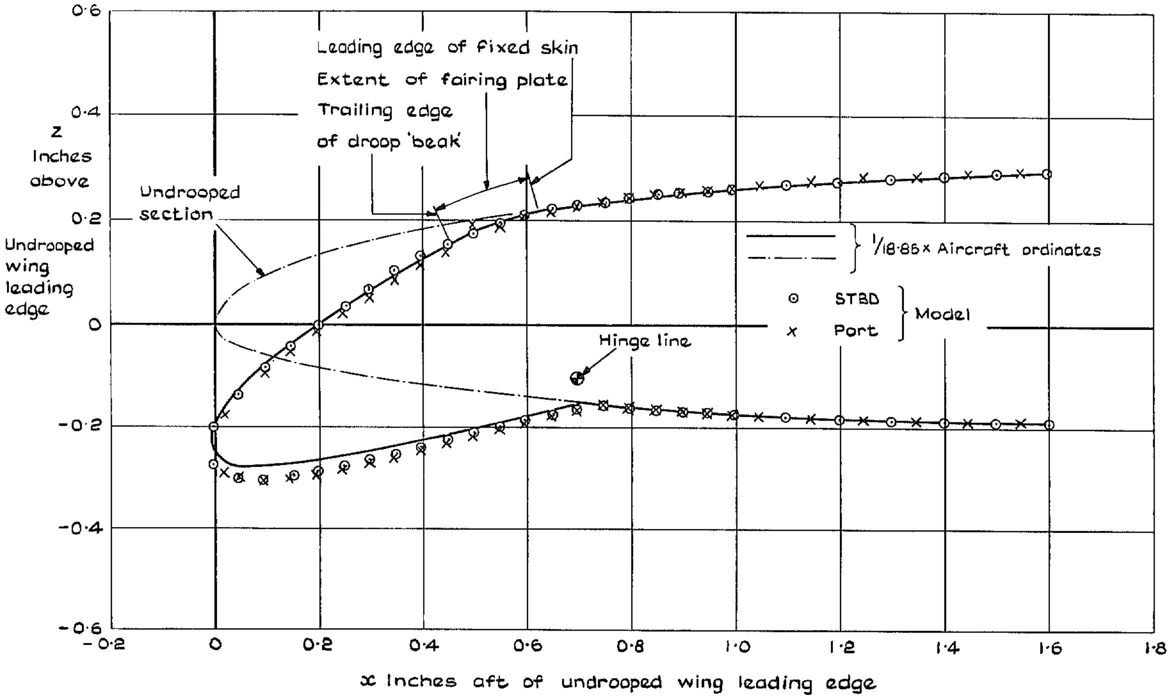

FIG. 14. Wing leading edge profile; section F.

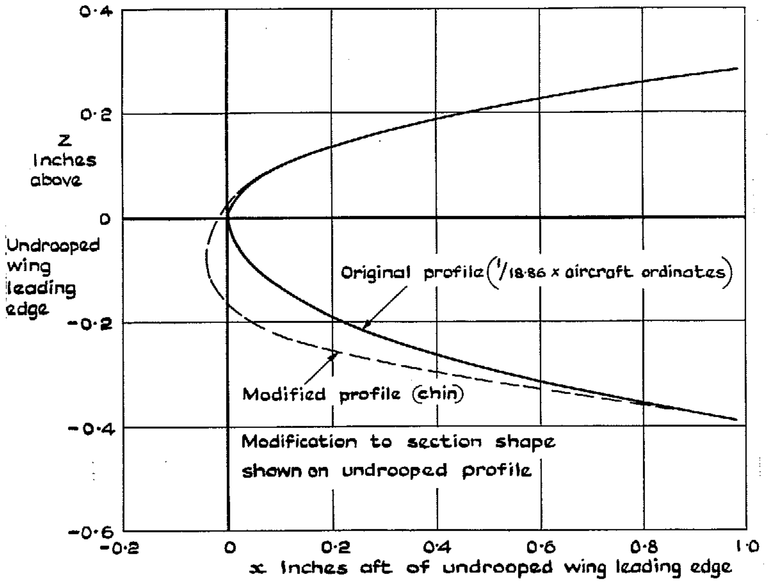

FIG. 15. Modification to wing leading edge profile on section C.

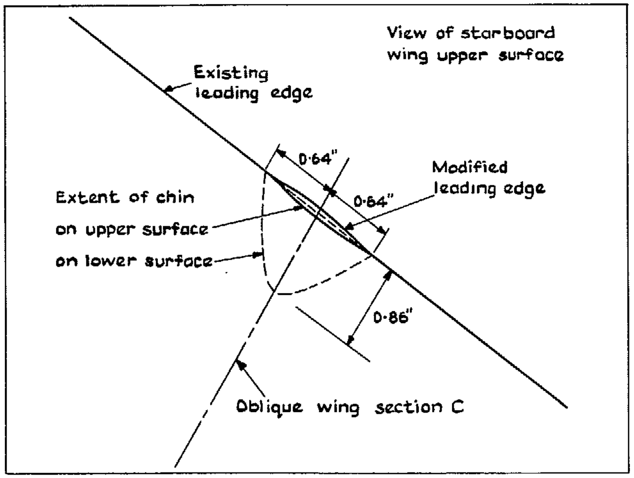

FIG. 16. Extent of modification to model wing leading edge profile.

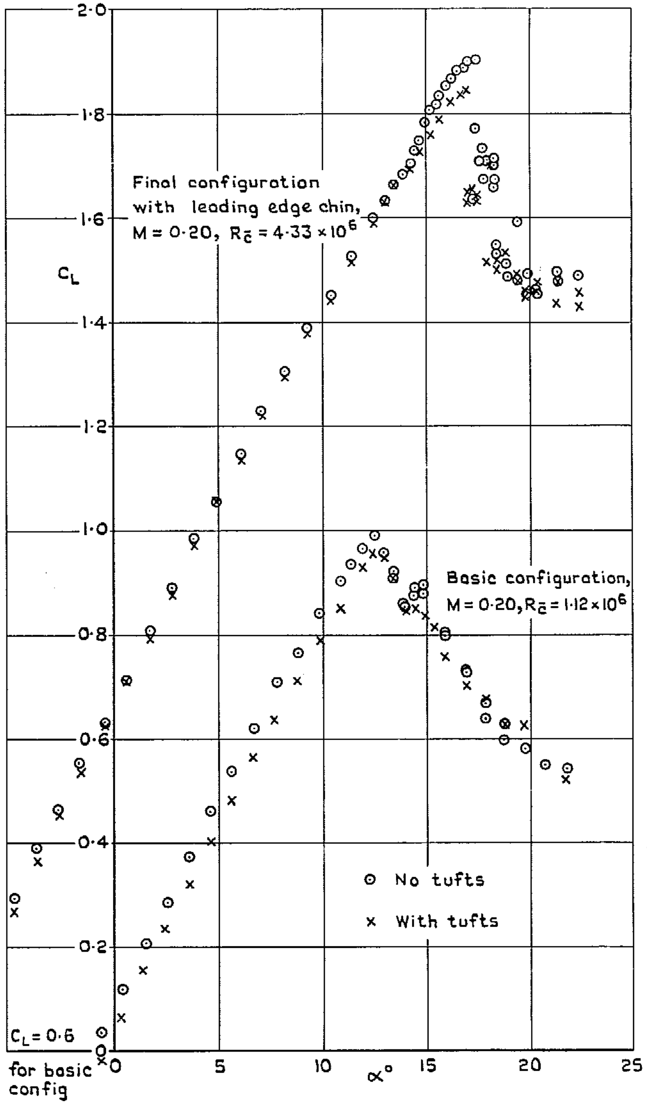

FIG. 17. Effect of tufts on lift.

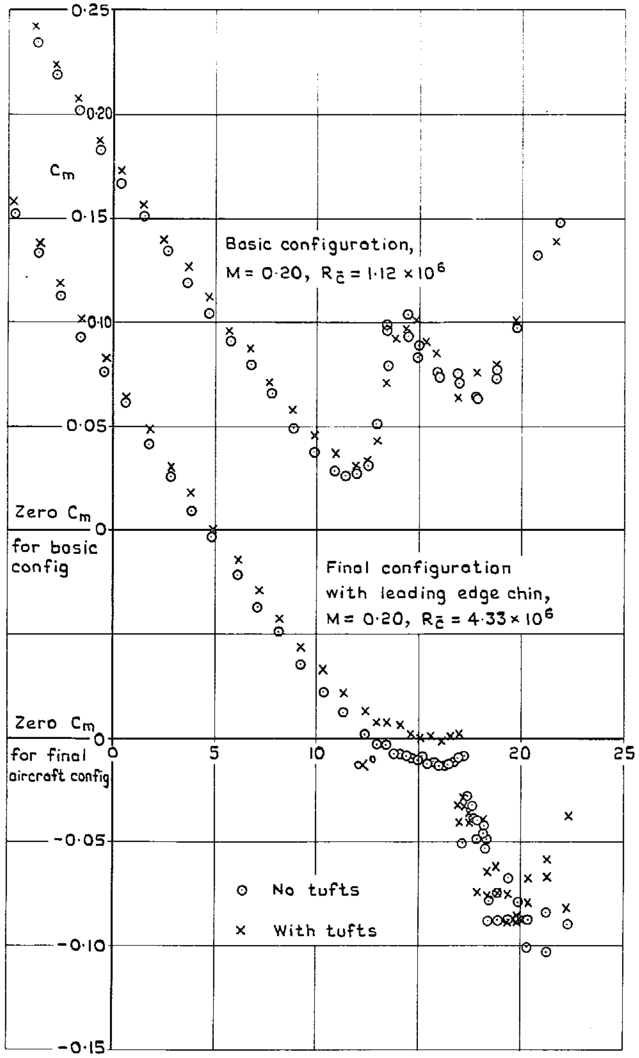

FIG. 18. Effect of tufts on pitching moment.

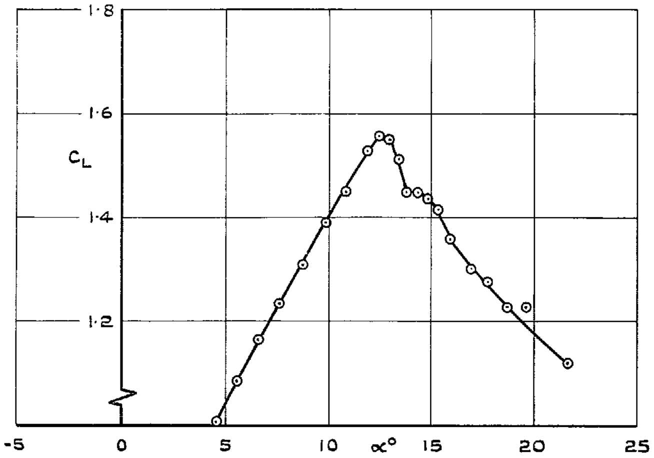

(a) C_L v α

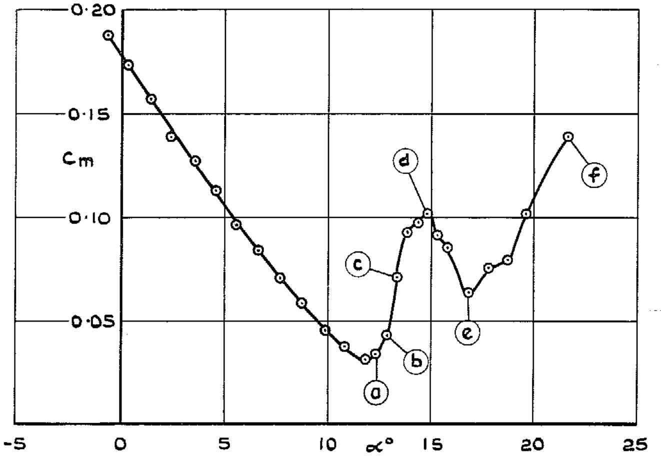

(b) C_m v α

FIG. 19a & b. Variation of C_L and C_m with α for basic configuration.
$M = 0{\cdot}20$, $R_{\bar{c}} = 1{\cdot}12 \times 10^6$, (with tufts)

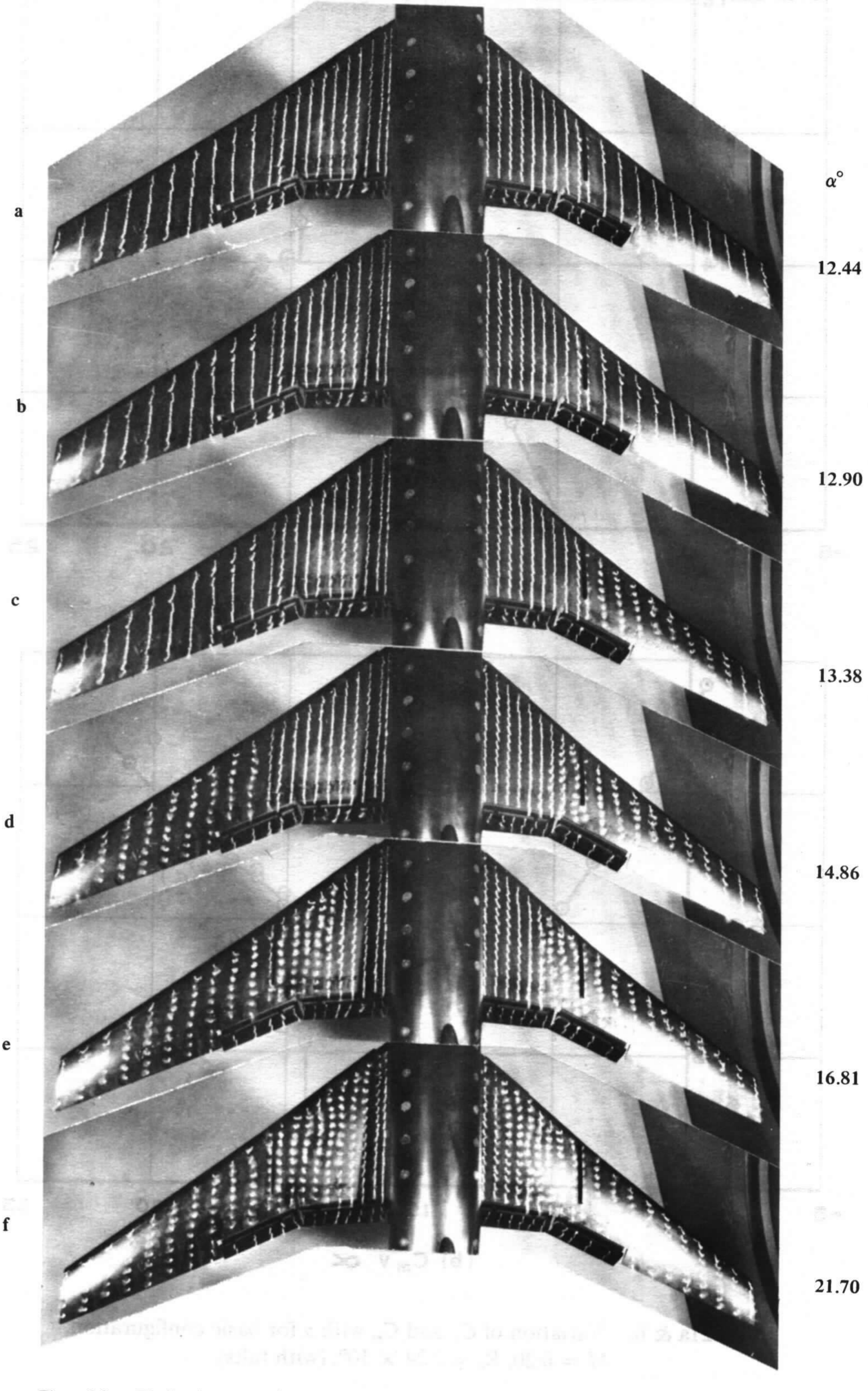

FIG. 20. Tuft patterns for basic configuration, $M = 0{\cdot}20$, $R_{\bar{c}} = 1{\cdot}12 \times 10^6$.

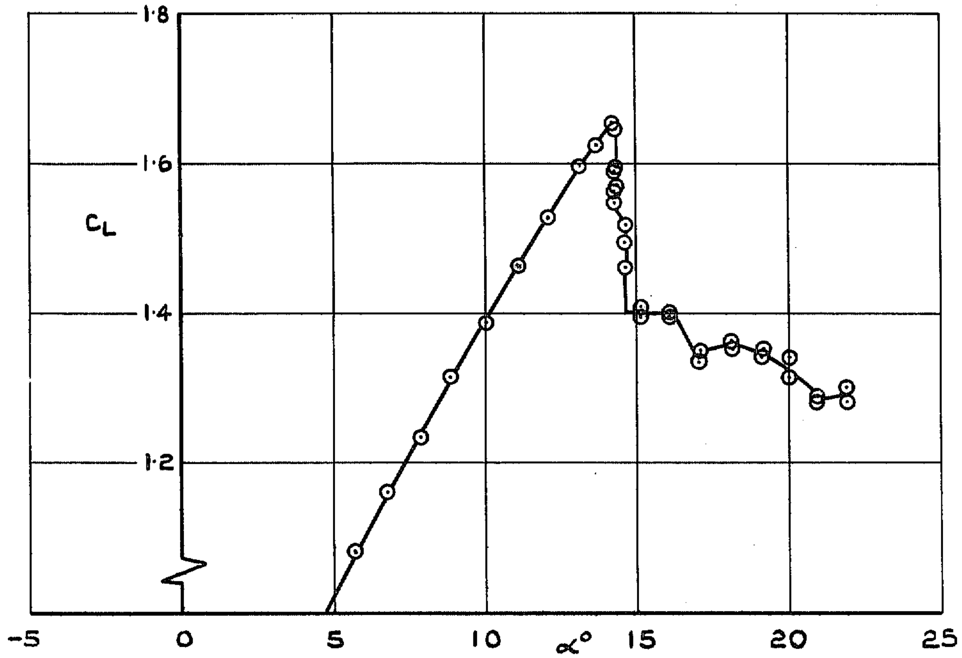

(a) C_L v α

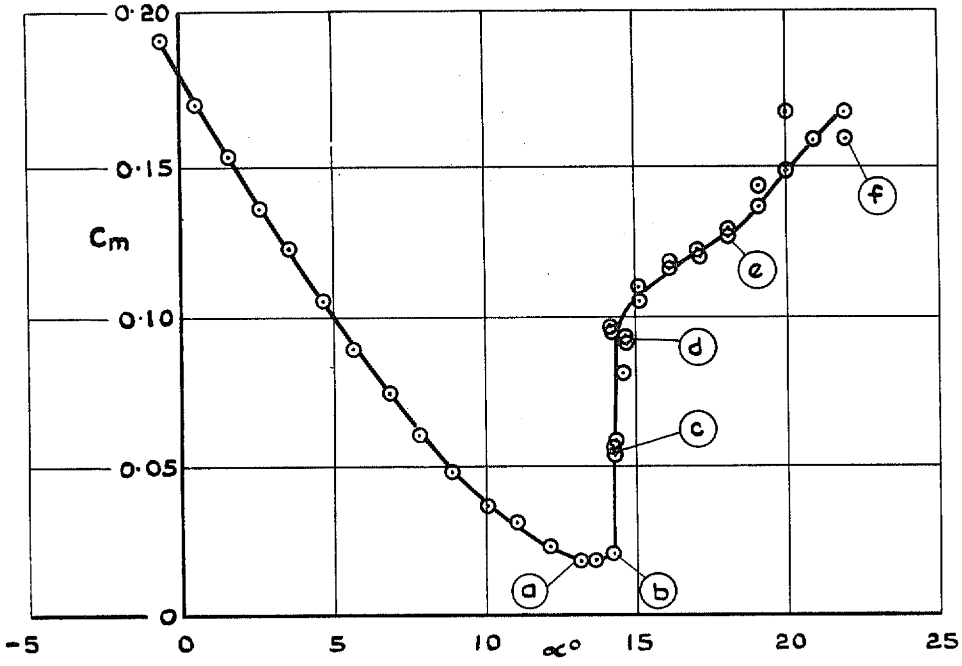

(b) C_m v α

FIG. 21a & b. Variation of C_L and C_m with α for basic configuration, $M = 0{\cdot}20$, $R_{\bar{c}} = 2{\cdot}24 \times 10^6$, (with tufts).

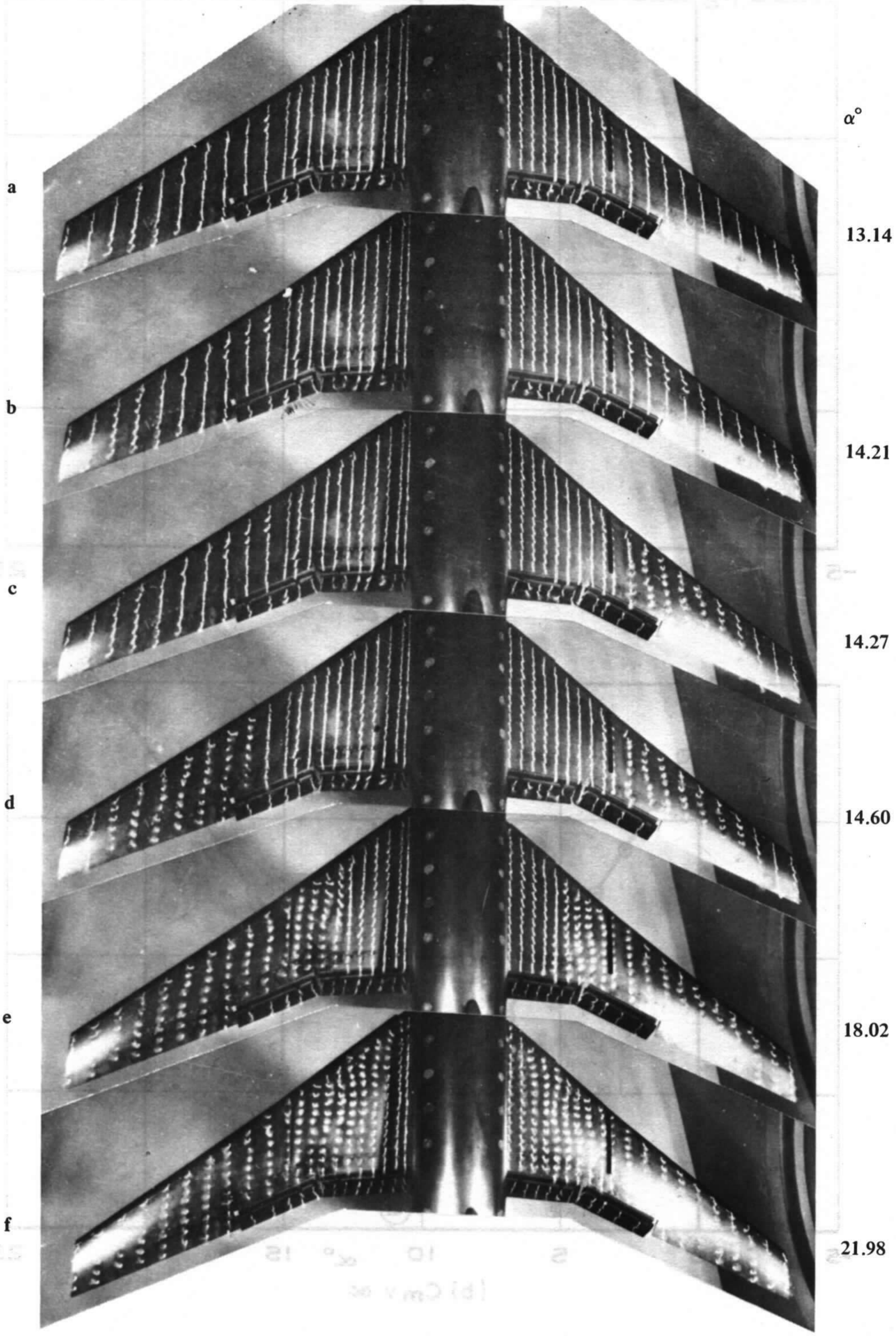

FIG. 22. Tuft patterns for basic configuration, $M = 0{\cdot}20$, $R_{\bar{c}} = 2{\cdot}24 \times 10^6$.

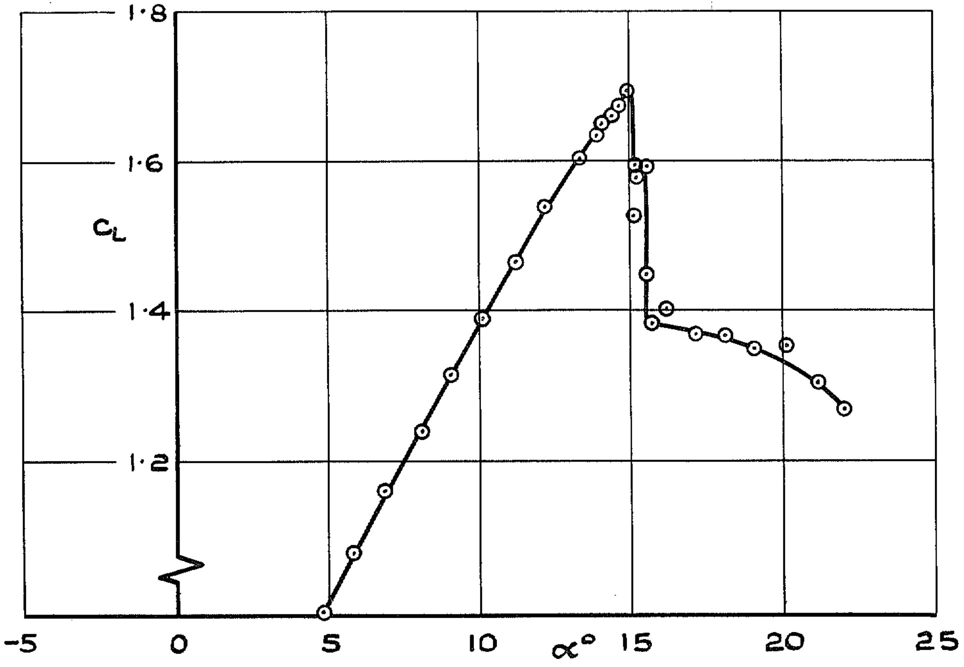

(a) C_L v α

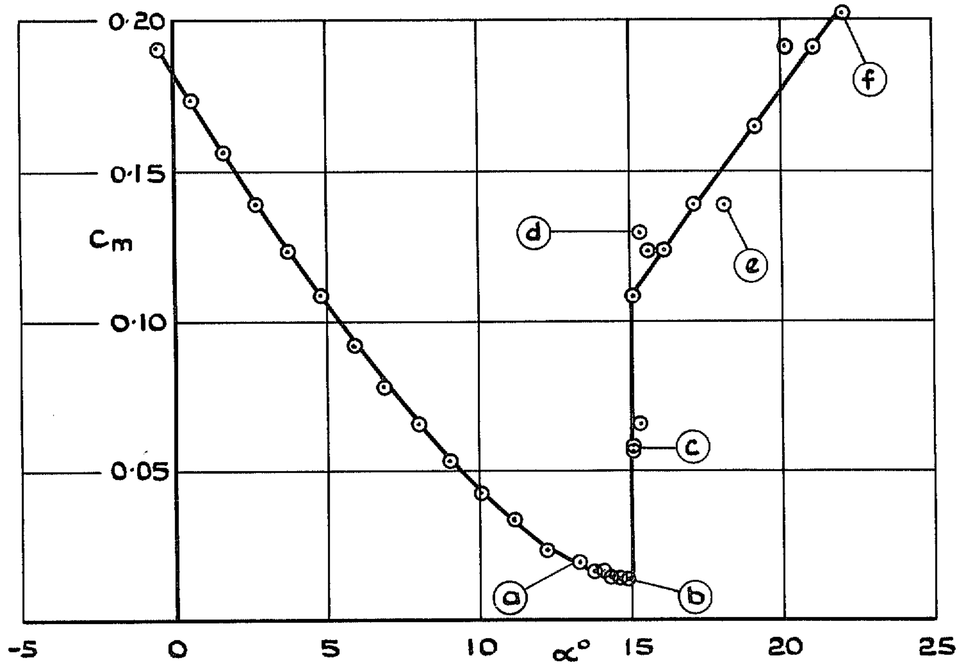

(b) C_m v α

FIG. 23a & b. Variation of C_L and C_m with α for basic configuration, $M = 0{\cdot}20$, $R_{\bar{c}} = 3{\cdot}36 \times 10^6$, (with tufts).

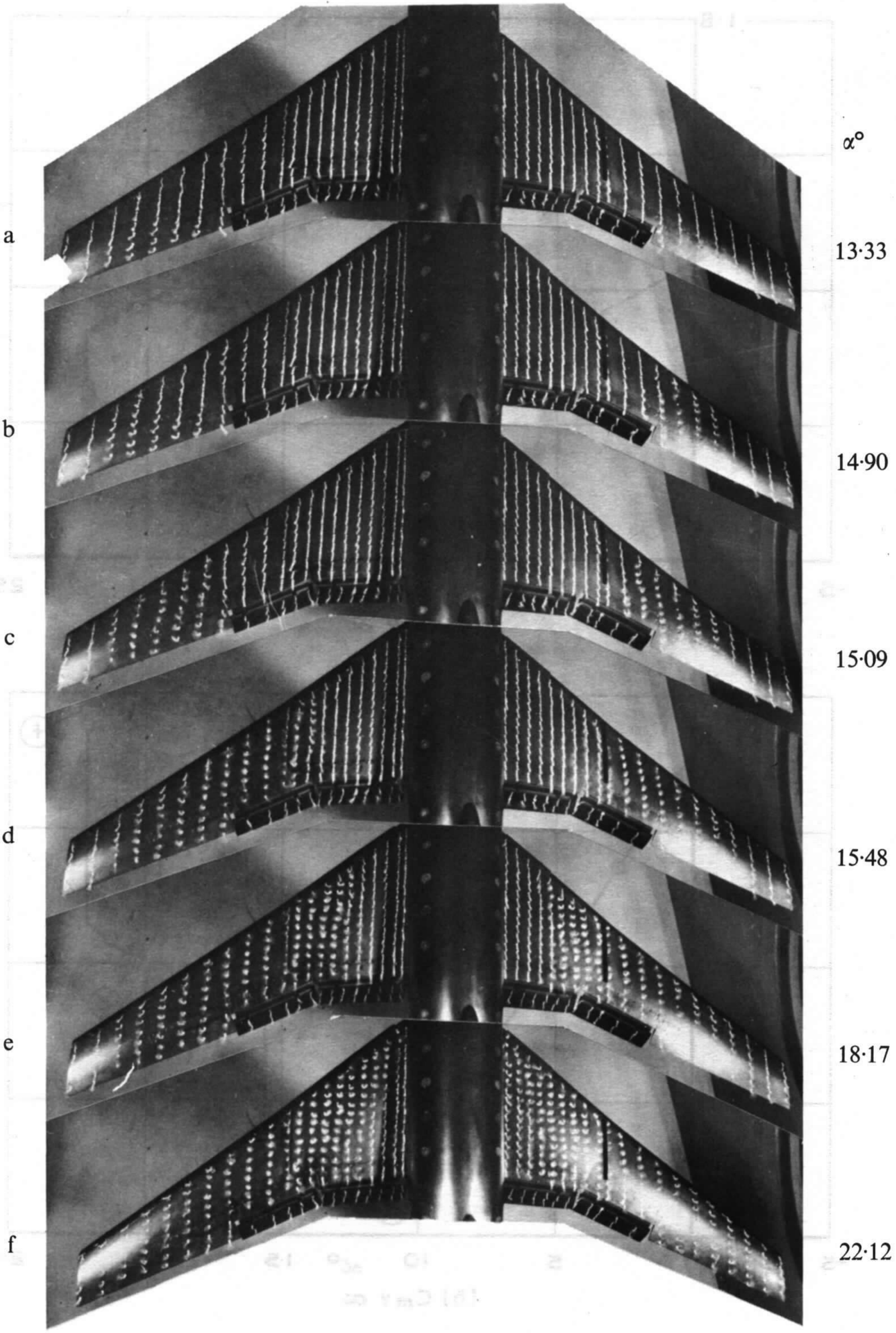

FIG. 24. Tuft patterns for basic configuration, $M = 0{\cdot}20$, $R_{\bar{c}} = 3{\cdot}36 \times 10^6$.

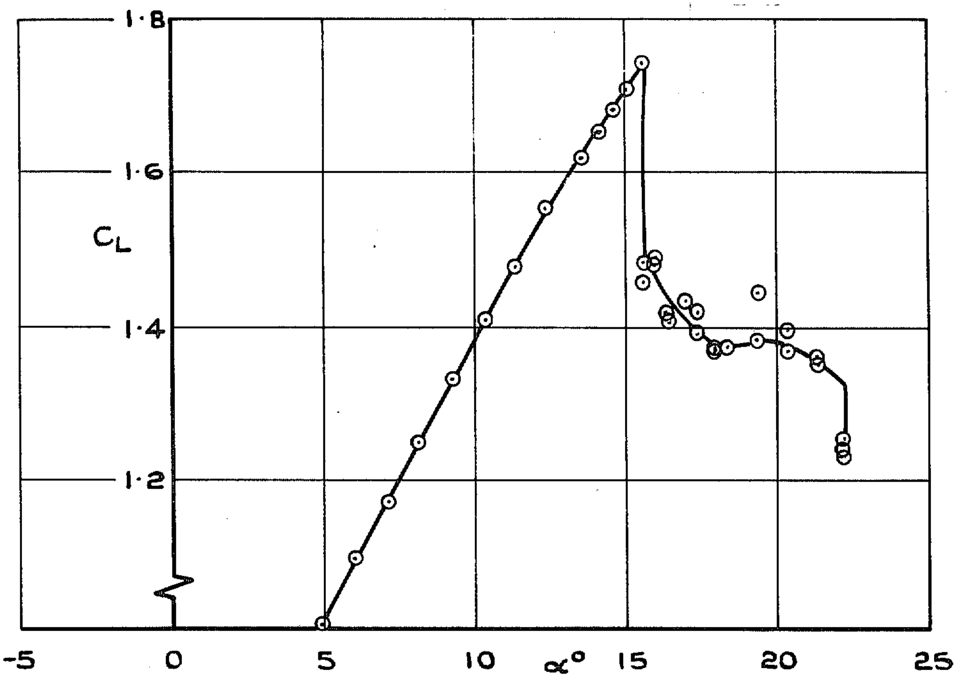

(a) C_L v α

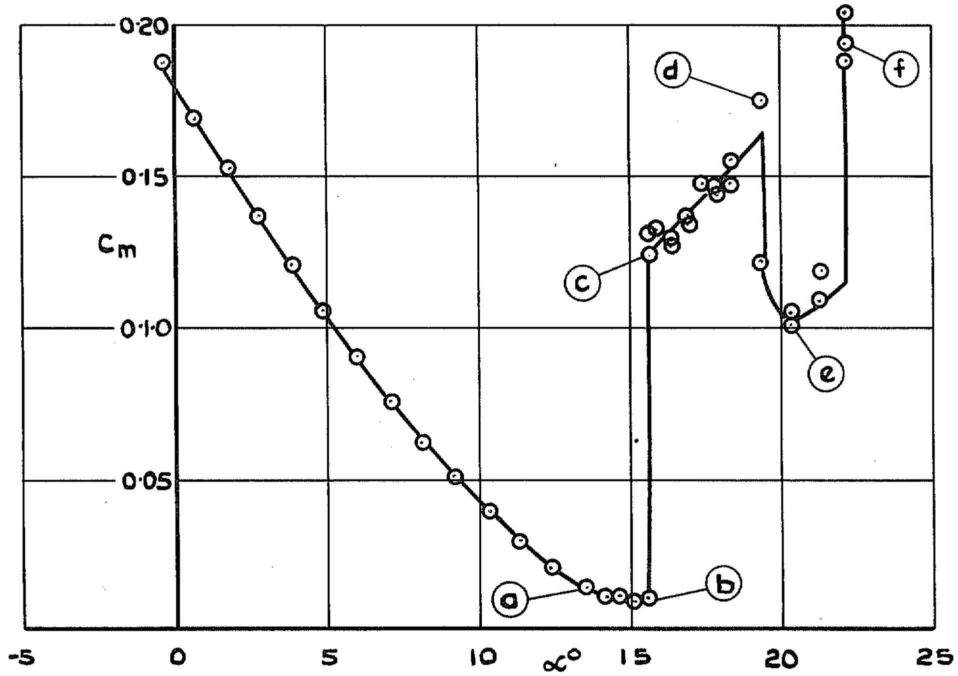

(b) C_m v α

FIG. 25a & b. Variation of C_L and C_m with α for basic configuration, $M = 0{\cdot}20$, $R_{\bar{c}} = 4{\cdot}33 \times 10^6$, (with tufts).

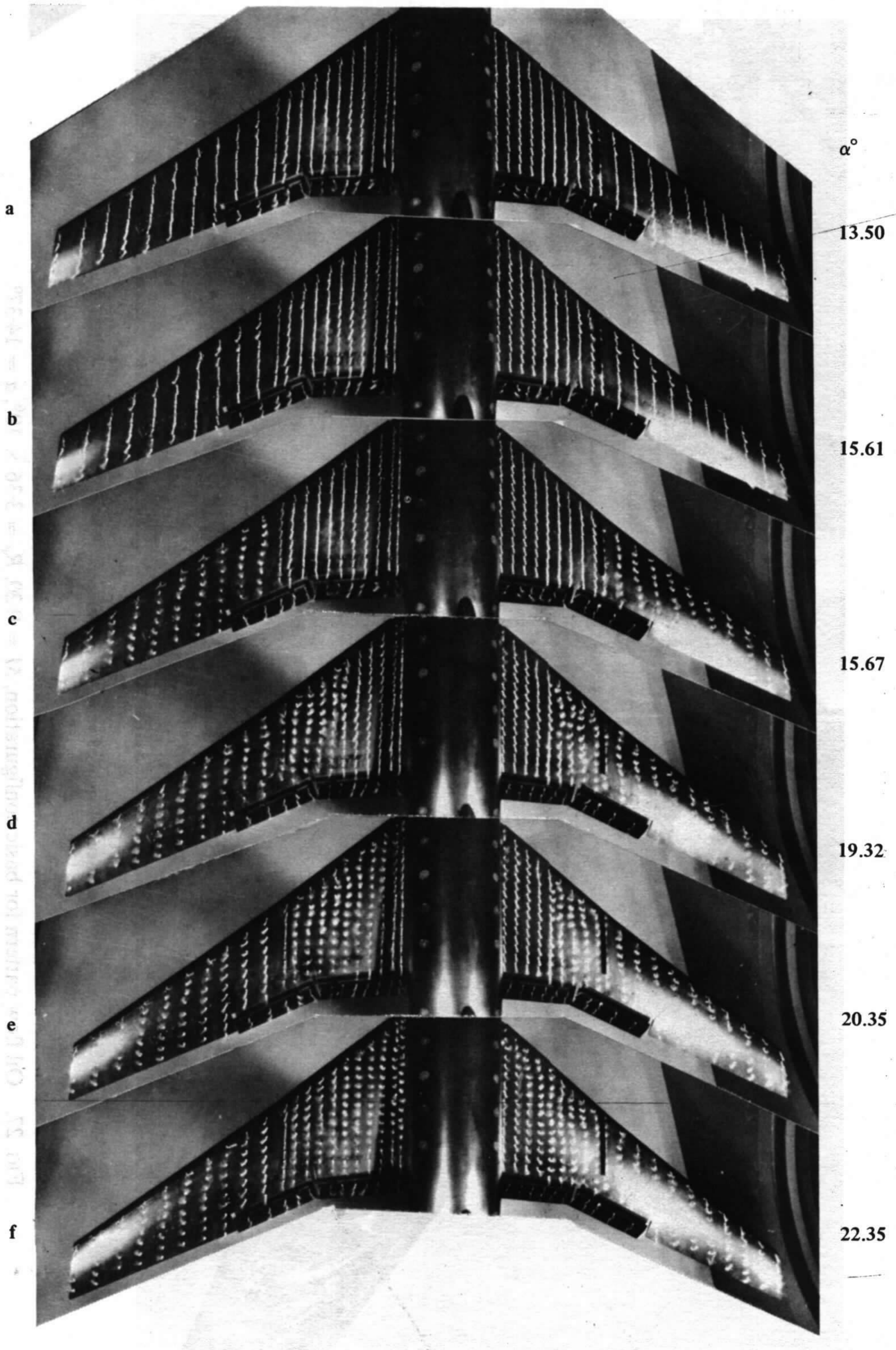

FIG. 26. Tuft patterns for basic configuration, $M = 0{\cdot}20$, $R_{\bar{c}} = 4{\cdot}33 \times 10^6$.

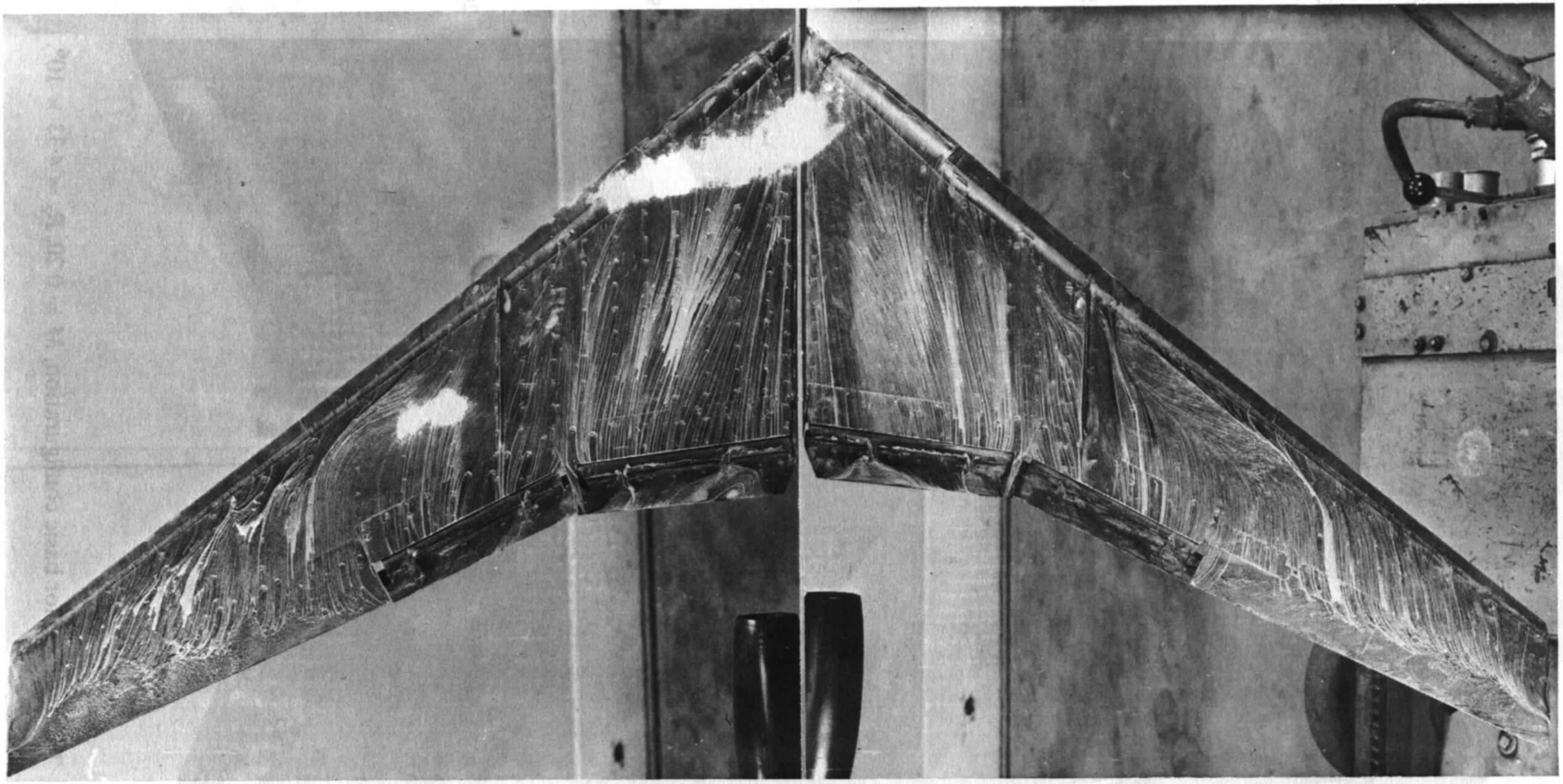

(a) General view of wing upper surfaces

FIG. 27. Oil flow pattern for basic configuration, $M = 0{\cdot}20$, $R_{\bar{c}} = 3{\cdot}36 \times 10^6$, $\alpha = 14{\cdot}37°$.

(b) Detail view of starboard wing leading edge at section C.

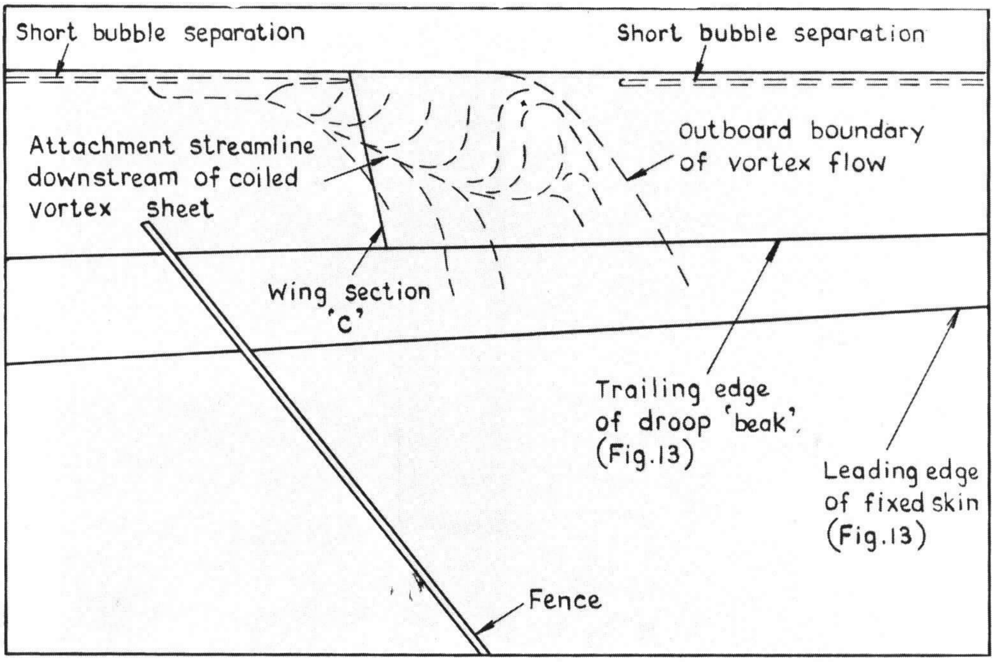

(c) Key to flow pattern in (b).

FIG. 27. Oil flow pattern for basic configuration, $M = 0{\cdot}20$, $R_{\bar{c}} = 3{\cdot}36 \times 10^6$, $\alpha = 14{\cdot}37°$.

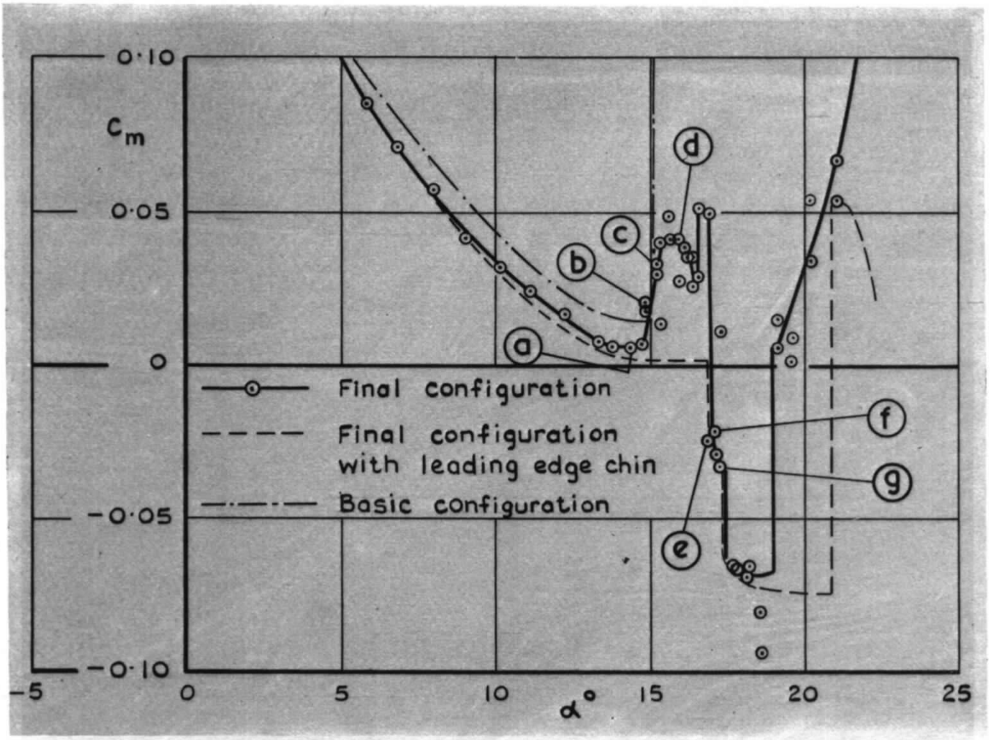

FIG. 28. Variation of C_m with α for final configuration, $M = 0{\cdot}20$, $R_{\bar{c}} = 3{\cdot}36 \times 10^6$, (with tufts).

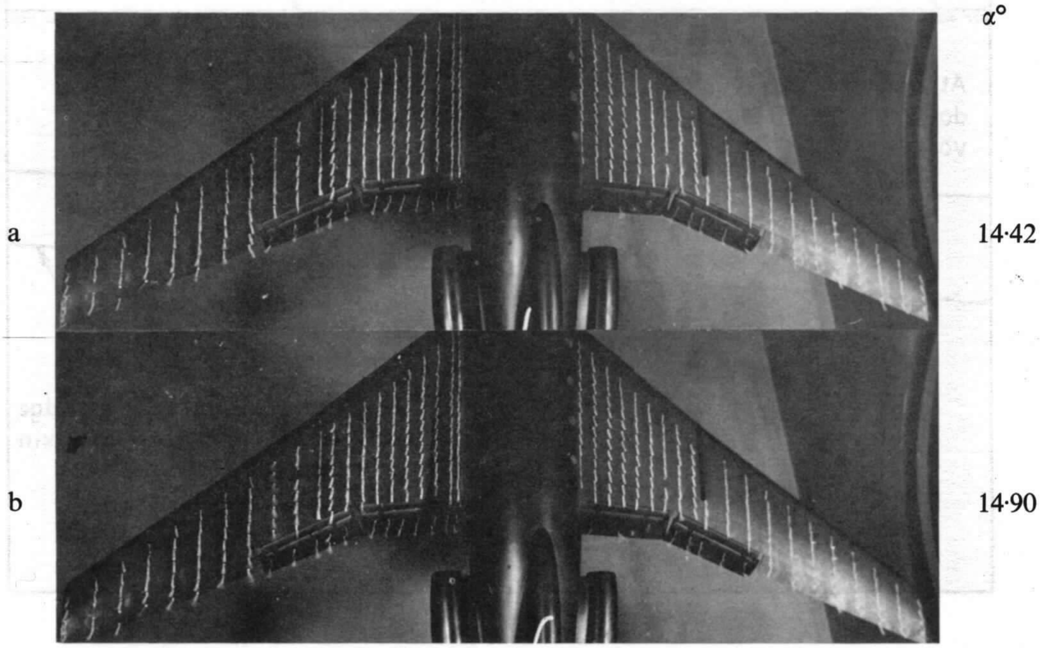

FIG. 29. Tuft patterns for final configuration, $M = 0{\cdot}20$, $R_{\bar{c}} = 3{\cdot}36 \times 10^6$.

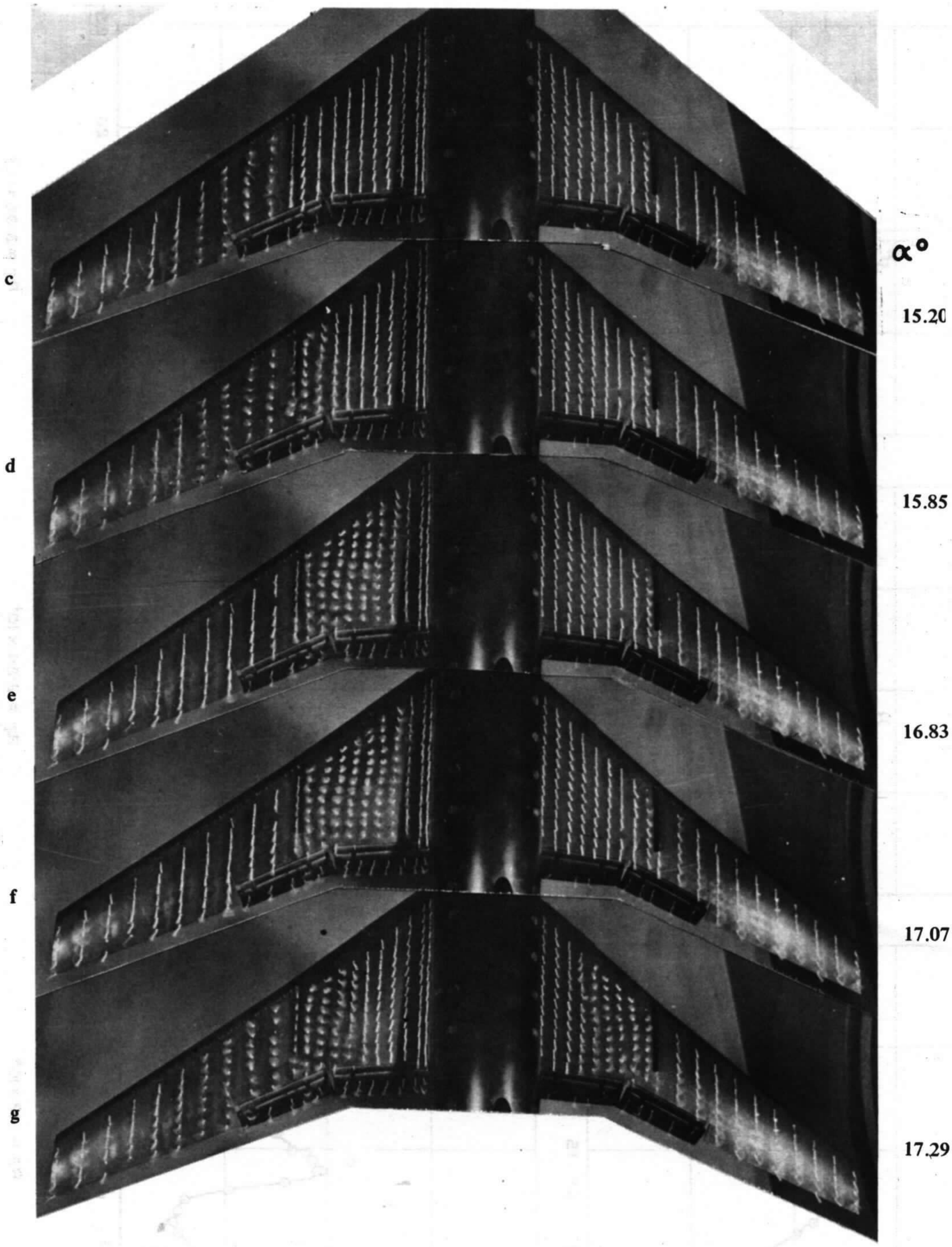

FIG. 29 *concld.* Tuft patterns for final configuration, $M = 0{\cdot}20$, $R_{\bar{c}} = 3{\cdot}36 \times 10^{6}$.

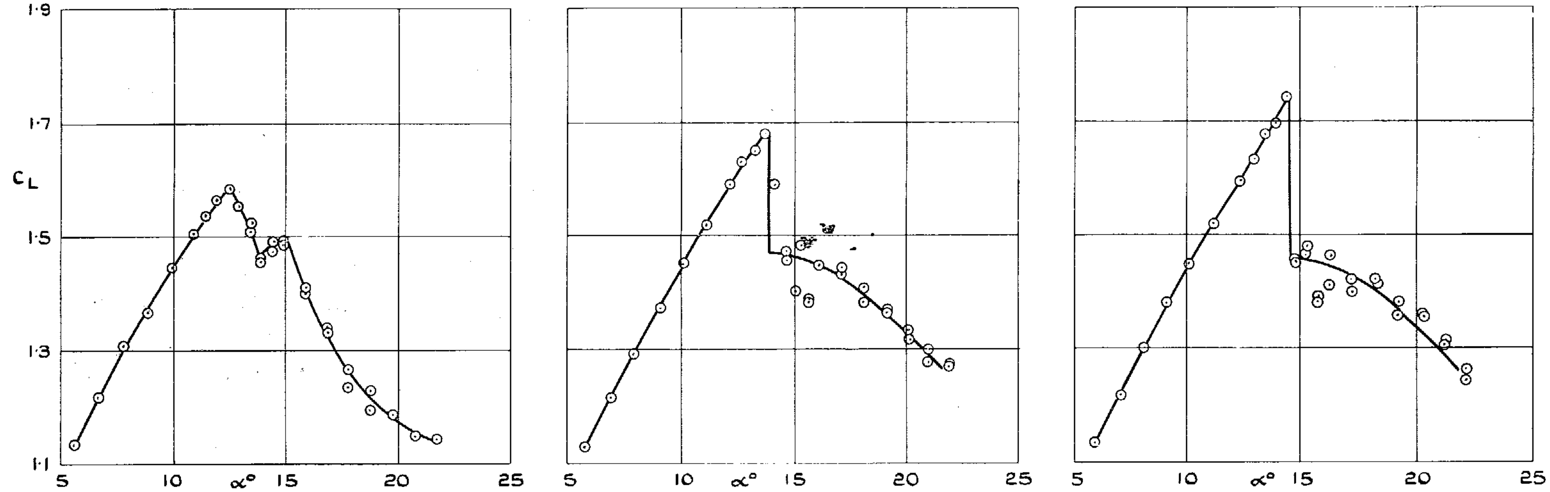

(a) C_L v α

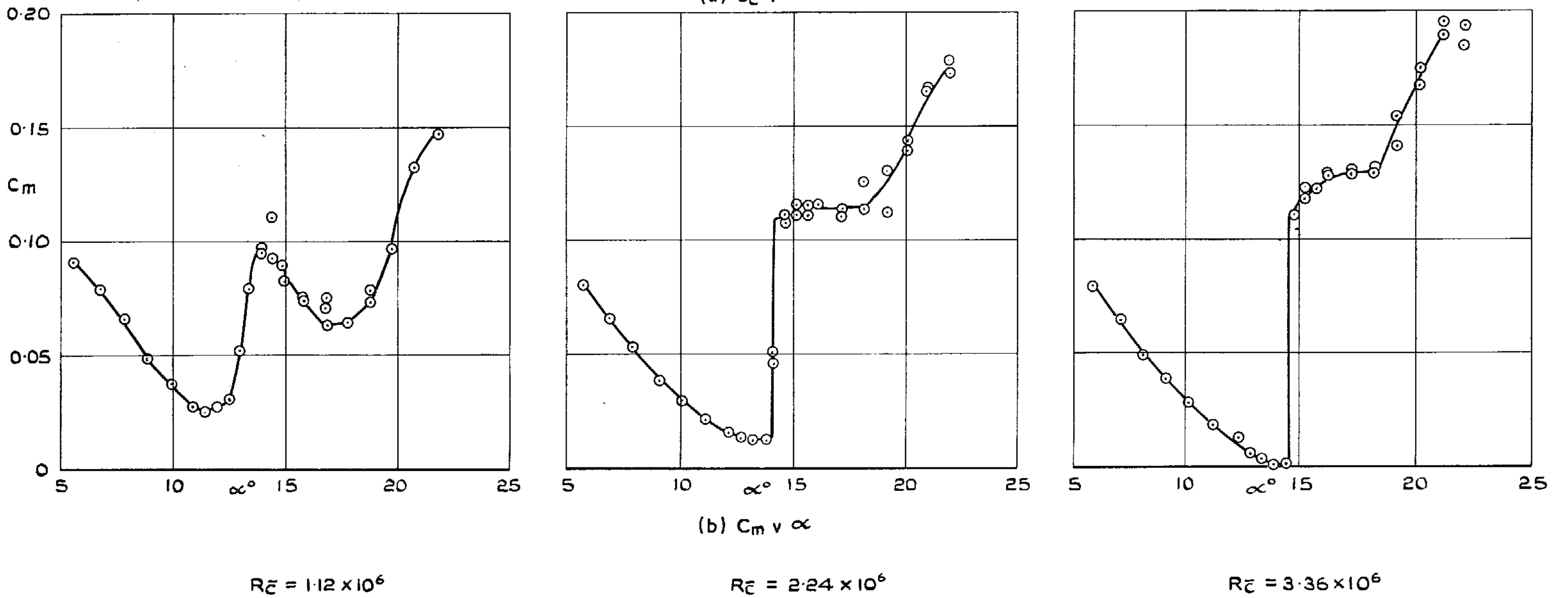

FIG. 30a & b. Effect of Reynolds number at $M = 0{\cdot}20$ on the variation of C_L and C_m with α for the basic configuration (no tufts).

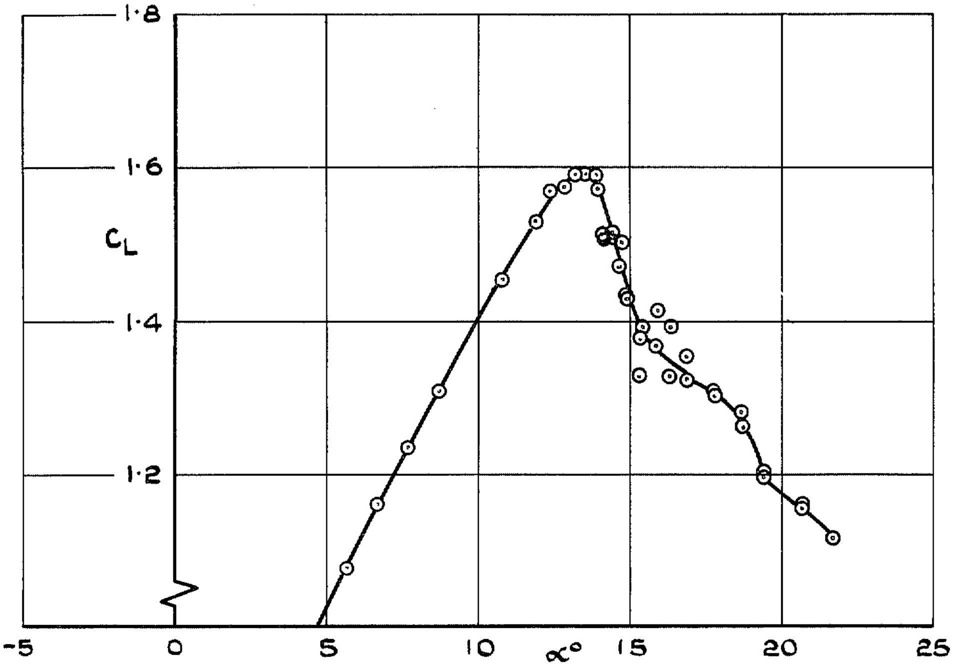

(a) C_L v α

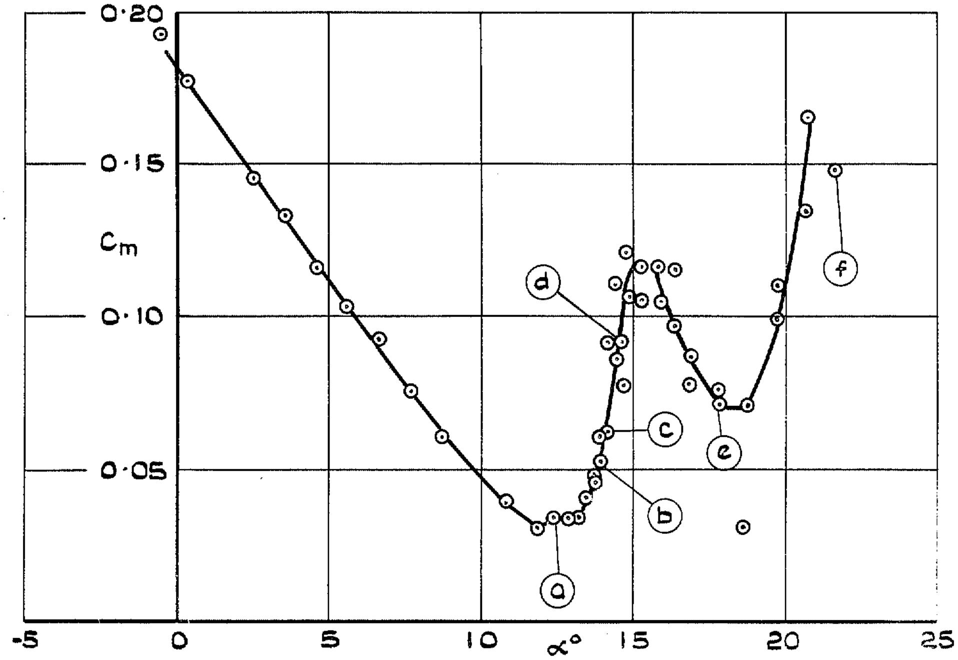

(b) C_m v α

FIG. 31a & b. Variations of C_L and C_m with α for final configuration with leading edge chin; $M = 0{\cdot}20$, $R_{\bar{c}} = 1{\cdot}12 \times 10^6$, (with tufts).

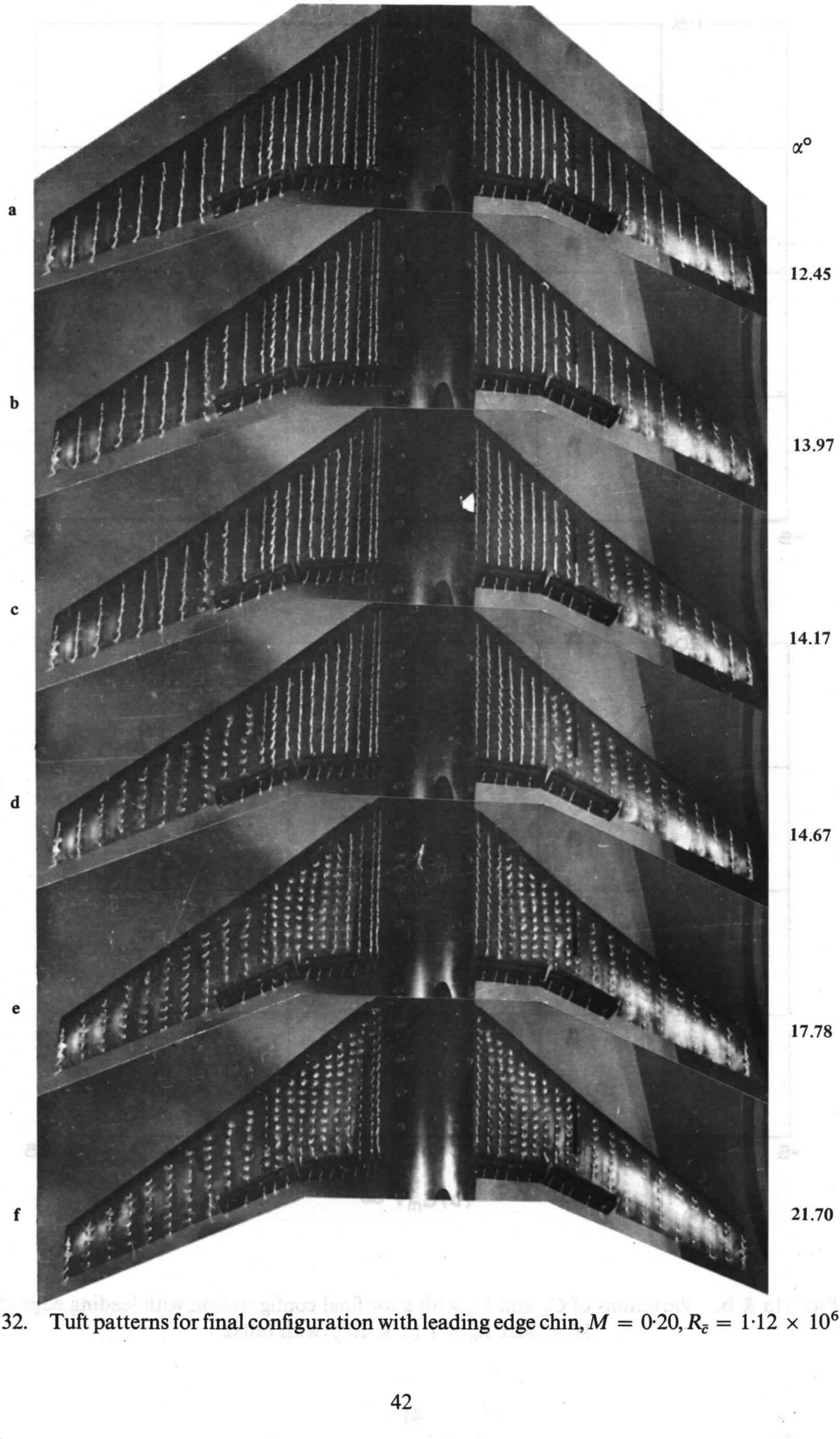

FIG. 32. Tuft patterns for final configuration with leading edge chin, $M = 0{\cdot}20, R_{\bar{c}} = 1{\cdot}12 \times 10^6$.

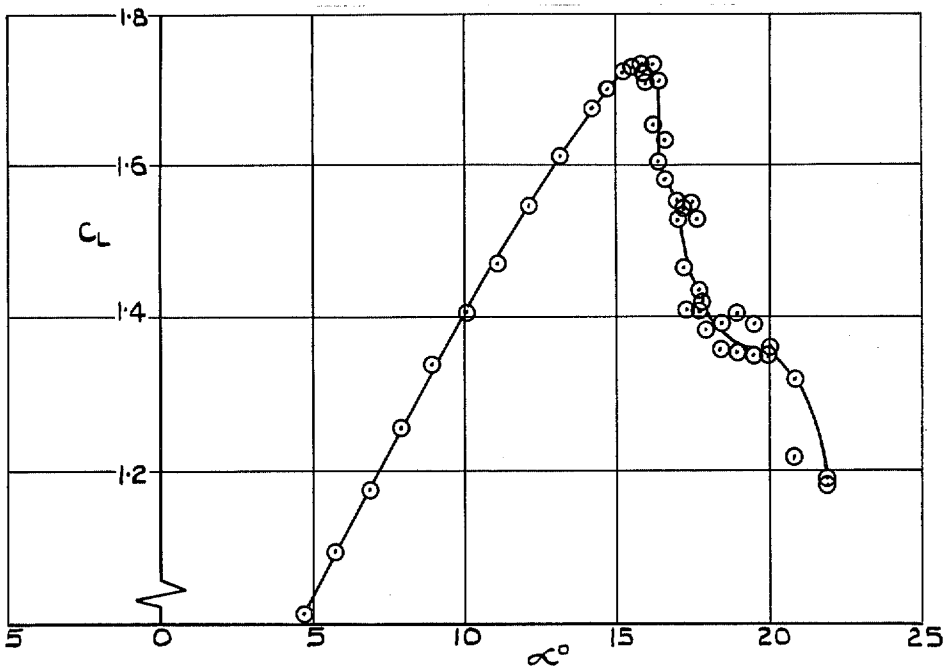

(a) C_L v α

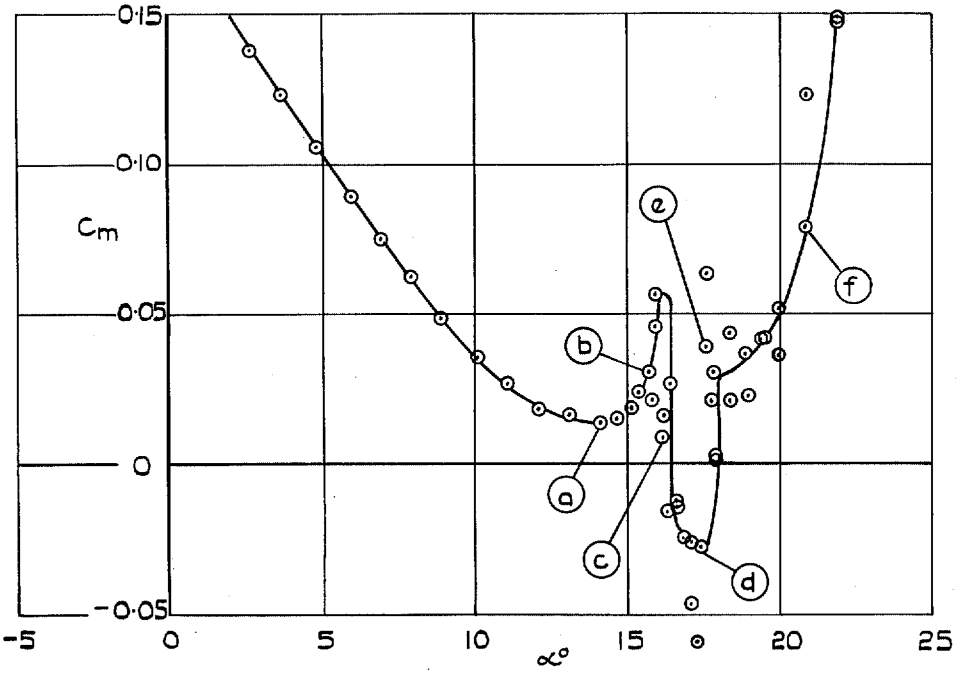

(b) C_m v α

FIG. 33a & b. Variation of C_L and C_m with α for final configuration with leading edge chin; $M = 0{\cdot}20$, $R_{\bar{c}} = 2{\cdot}24 \times 10^6$, (with tufts).

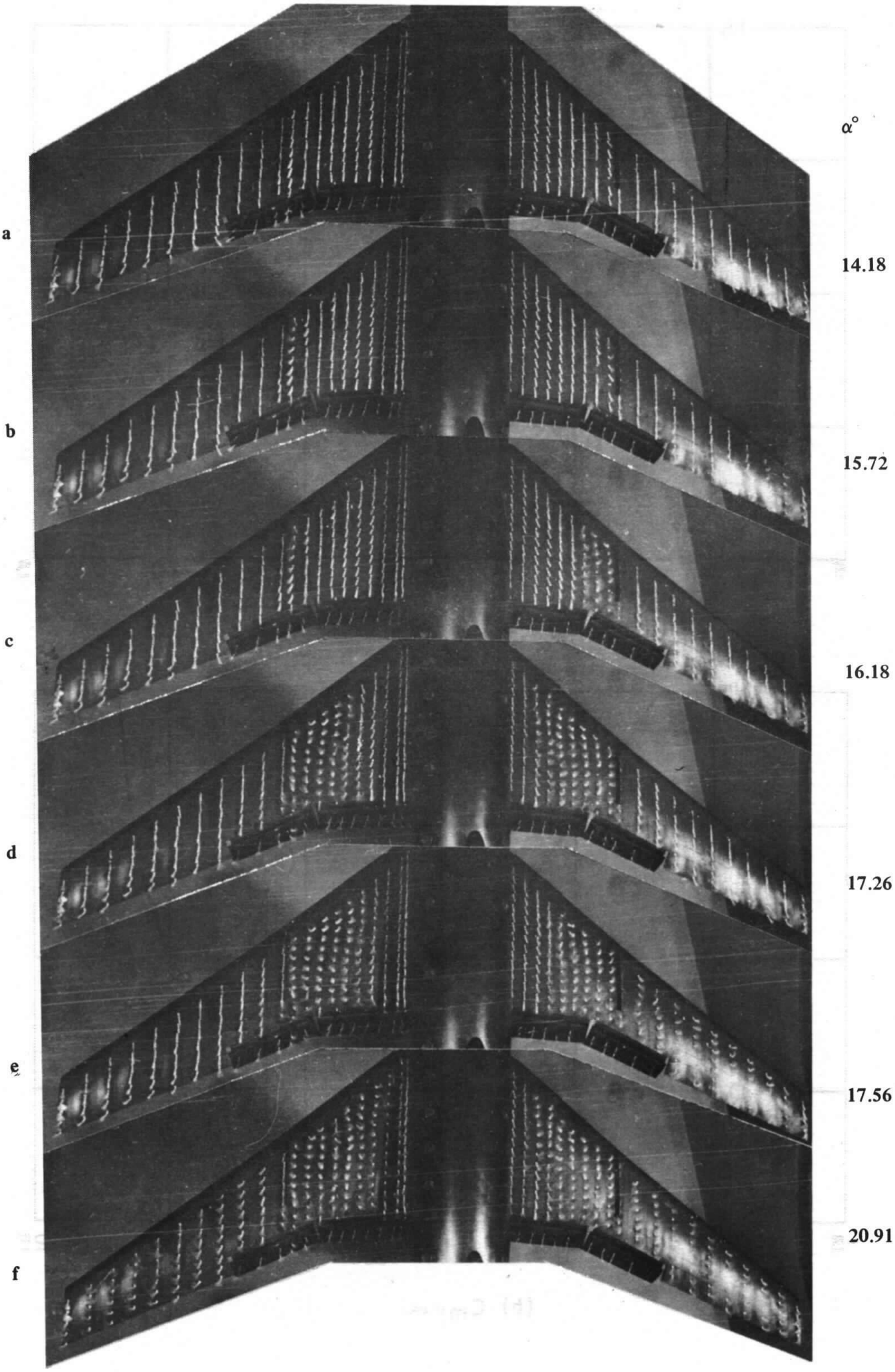

FIG. 34. Tuft patterns for final configuration with leading edge chin, $M = 0{\cdot}20, R_{\bar{c}} = 2{\cdot}24 \times 10^{6}$.

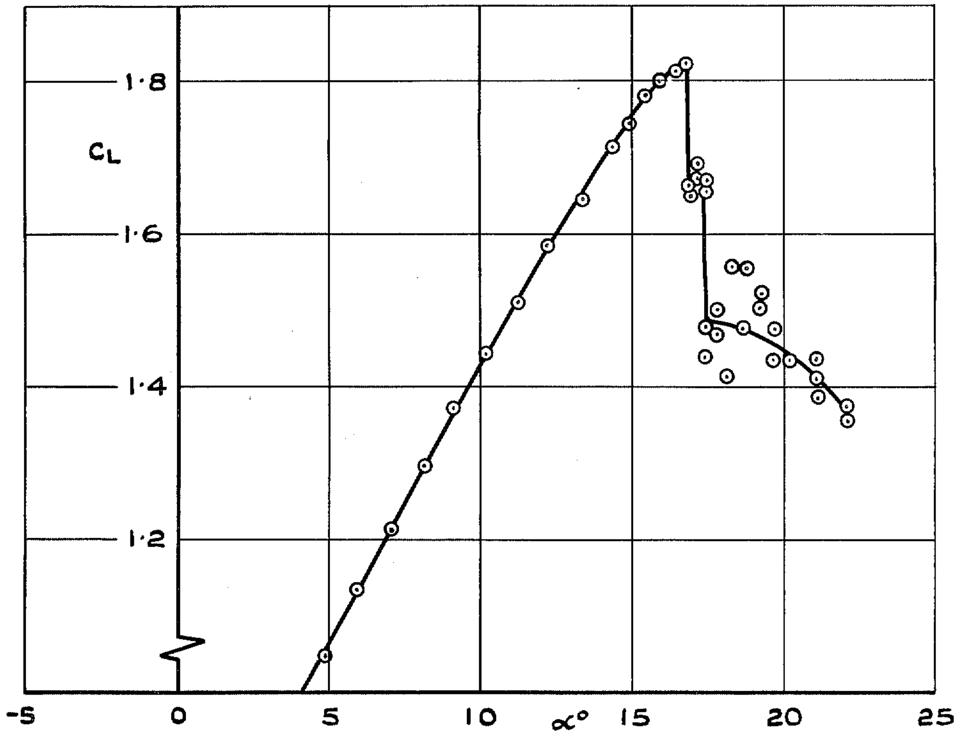

(a) C_L v α

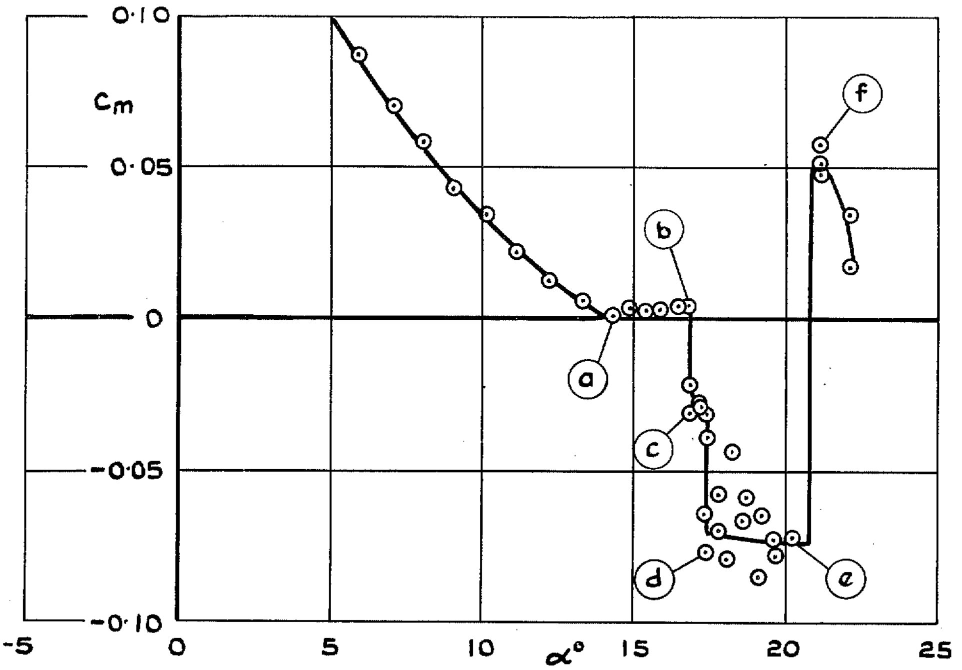

(b) C_m v α

FIG. 35a & b. Variation of C_L and C_m with α for final configuration with leading edge chin; $M = 0{\cdot}20$, $R_{\bar{c}} = 3{\cdot}36 \times 10^6$, (with tufts).

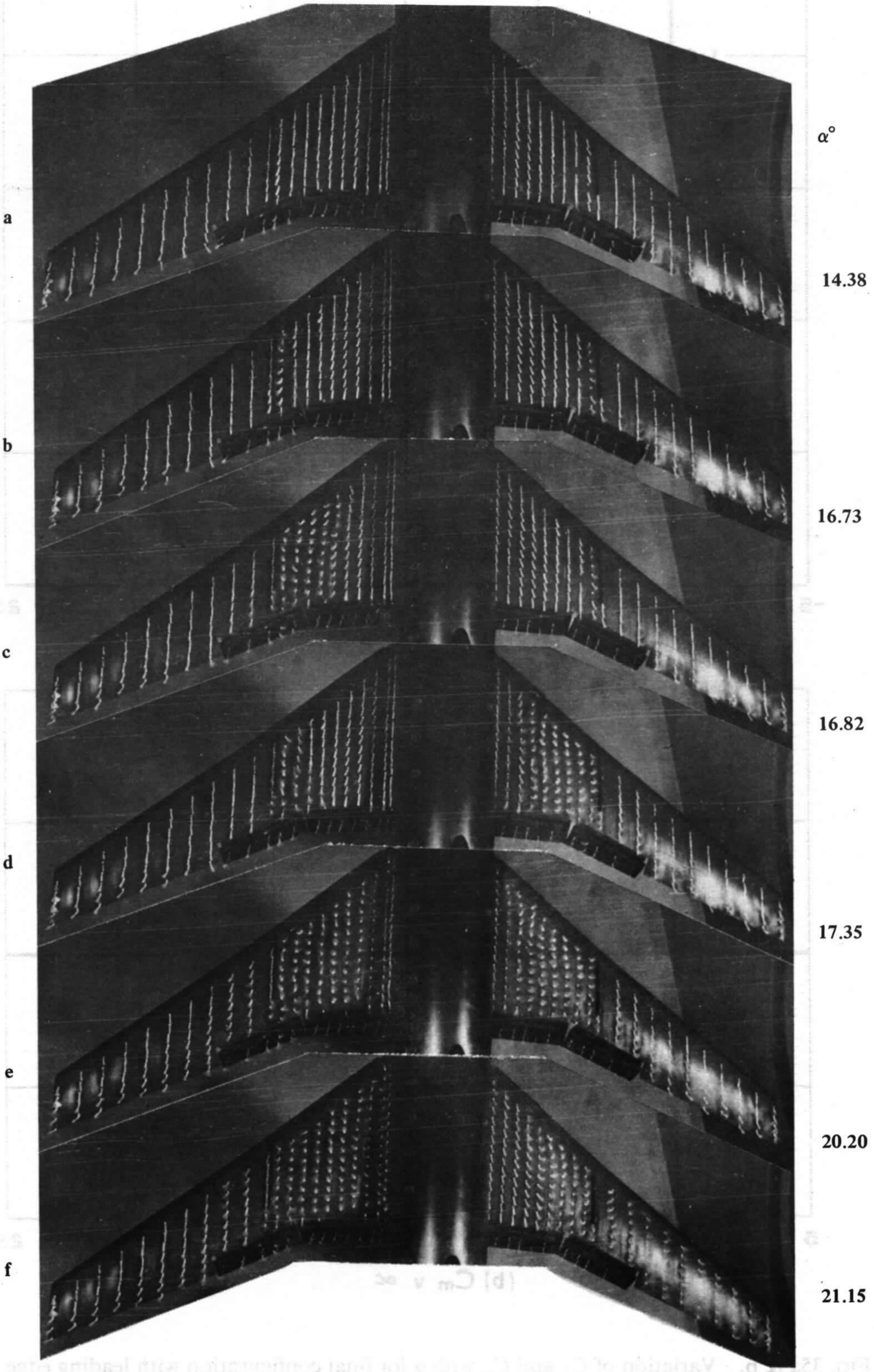

FIG. 36. Tuft patterns for final configuration with leading edge chin, $M = 0{\cdot}20$, $R_{\bar{c}} = 3{\cdot}36 \times 10^6$.

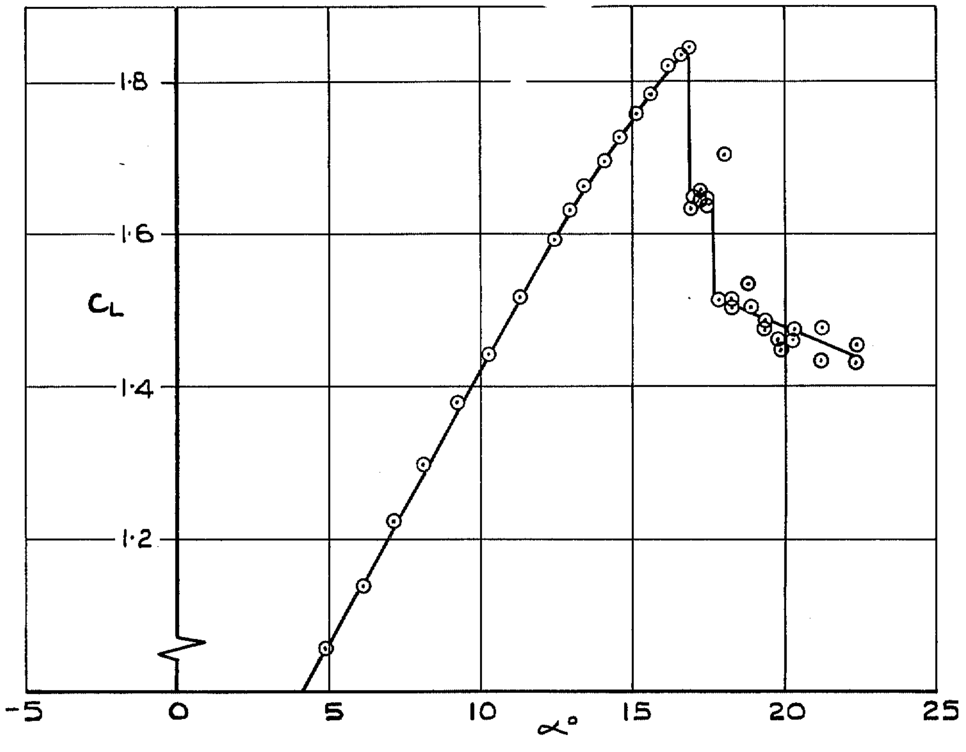

(a) C_L v α

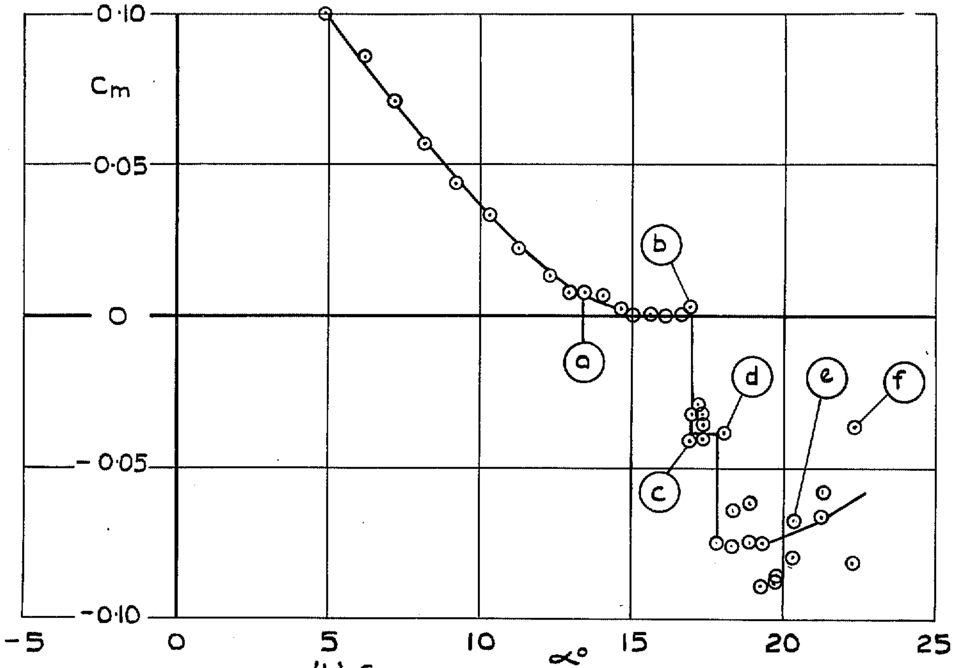

(b) C_m v α

FIG. 37a & b. Variation of C_L and C_m with α for final configuration with leading edge chin; $M = 0{\cdot}20$, $R_{\bar{c}} = 4{\cdot}33 \times 10^6$, (with tufts).

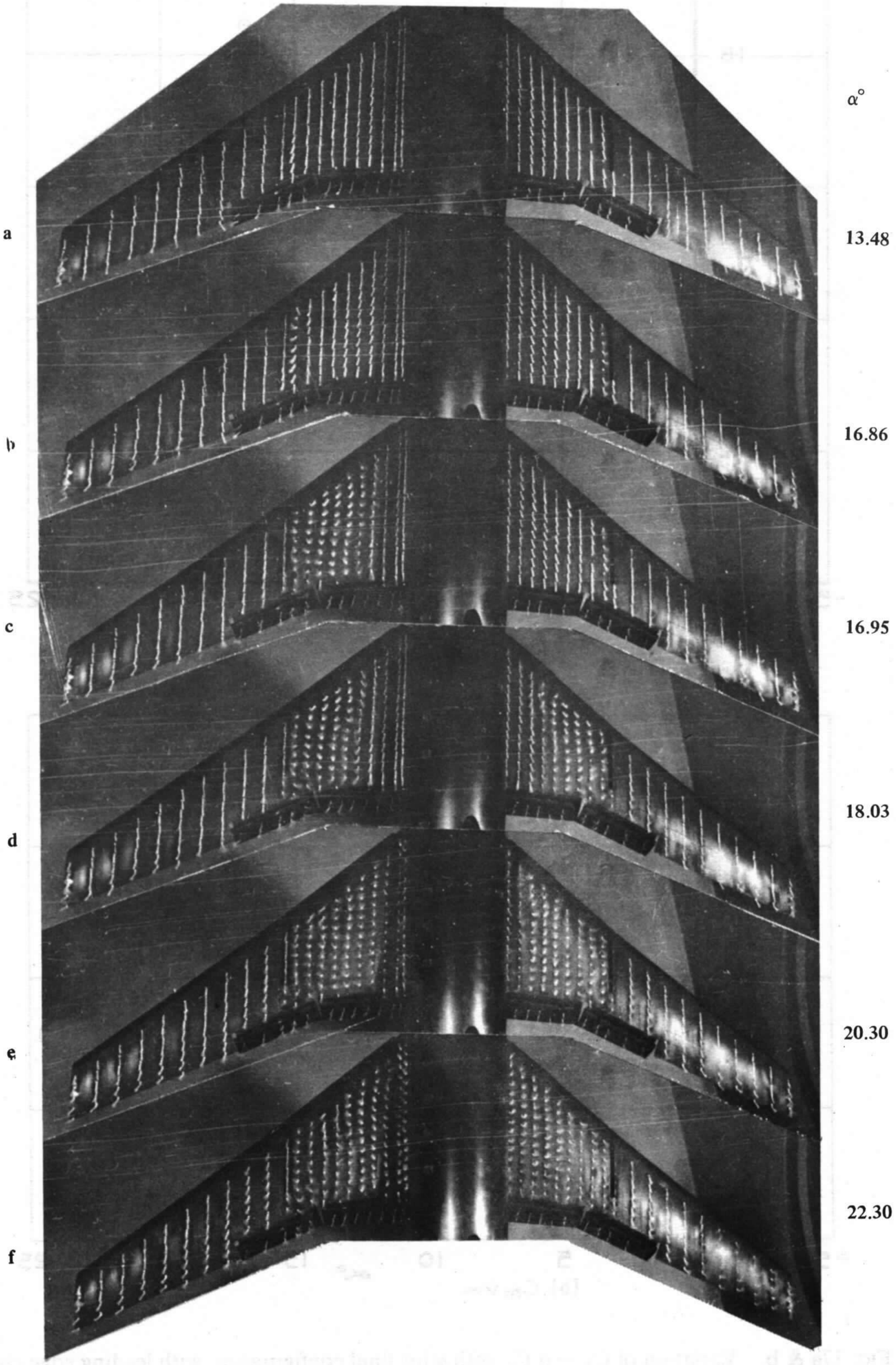

FIG. 38. Tuft patterns for final configuration with leading edge chin; $M = 0{\cdot}20$, $R_{\bar{c}} = 4{\cdot}33 \times 10^6$.

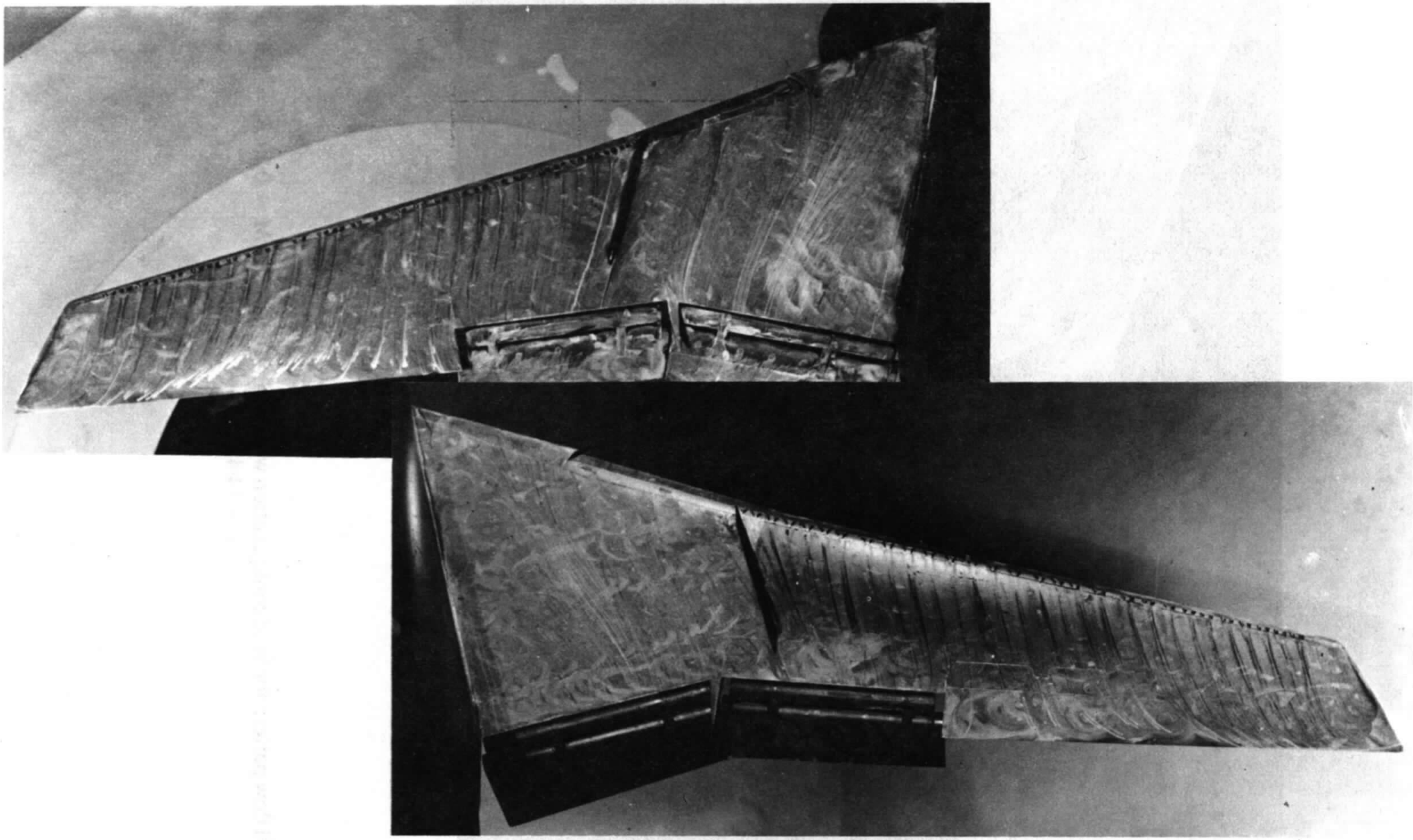

(a) General view of wing upper surfaces.

FIG. 39. Oil flow pattern for final configuration with leading edge chin; $M = 0{\cdot}20$, $R_{\bar{c}} = 3{\cdot}36 \times 10^6$, $\alpha = 14{\cdot}42°$.

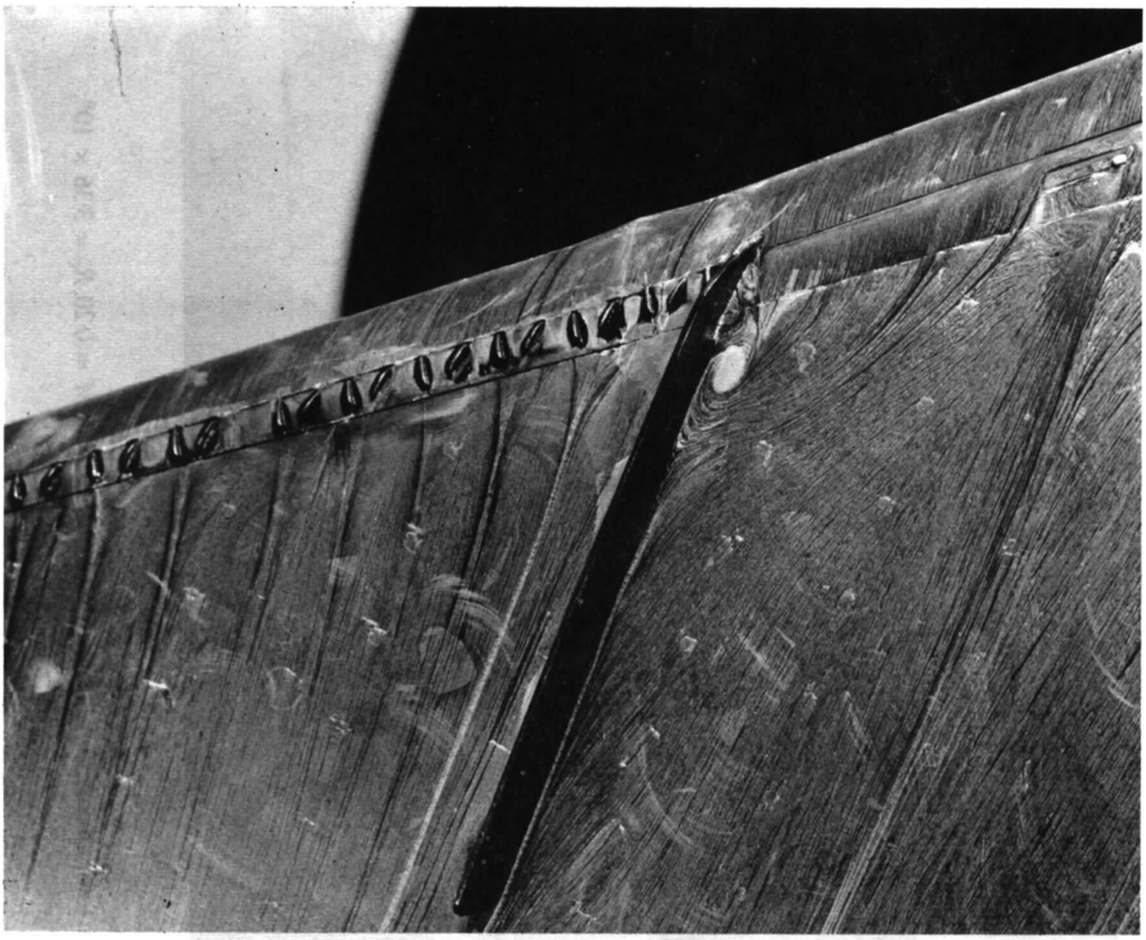

(b) Detail view of port wing leading edge at section C.

FIG. 39 *contd.* Oil flow pattern for final configuration with leading edge chin, $M = 0{\cdot}20$, $R_{\bar{c}} = 3{\cdot}36 \times 10^6$, $\alpha = 14{\cdot}42°$.

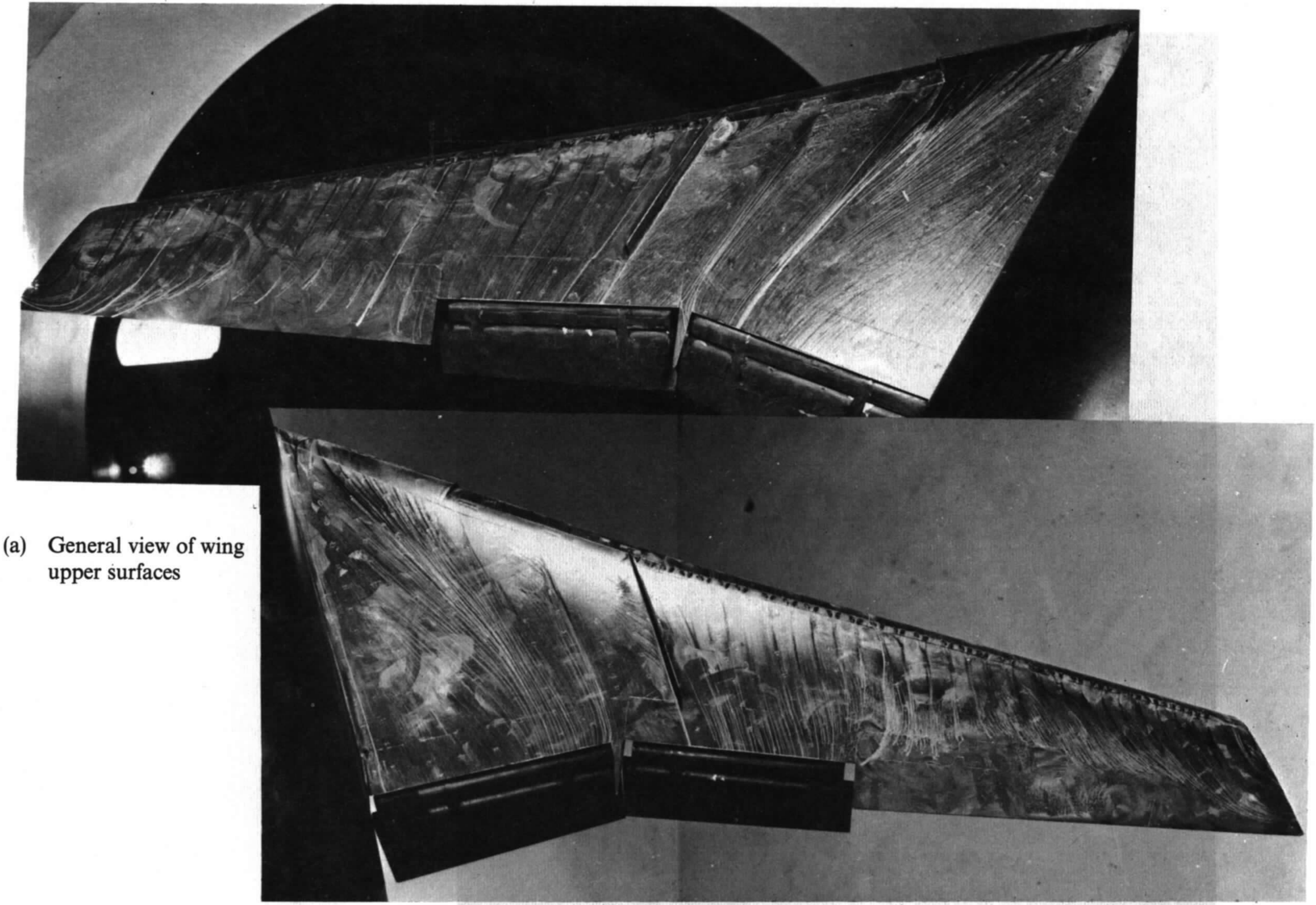

(a) General view of wing upper surfaces

FIG. 40. Oil flow pattern for final configuration with leading edge chin; $M = 0{\cdot}20$, $R_{\bar{c}} = 3{\cdot}36 \times 10^{6}$, $\alpha = 16{\cdot}44^{\circ}$.

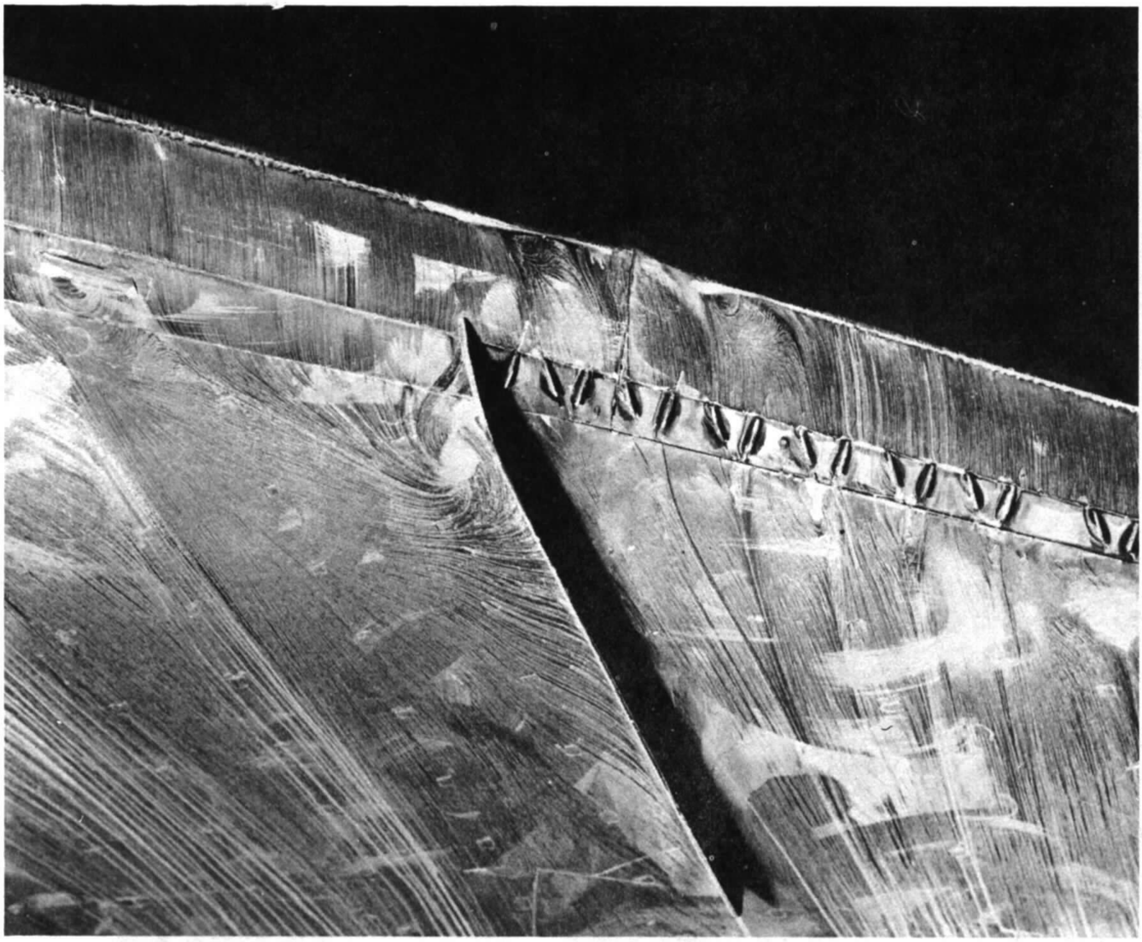

(b) Detail view of starboard wing leading edge at section C.

FIG. 40 *contd.* Oil flow pattern for final configuration with leading edge chin; $M = 0{\cdot}20, R_{\bar{c}} = 3{\cdot}36 \times 10^6$, $\alpha = 16{\cdot}44°$.

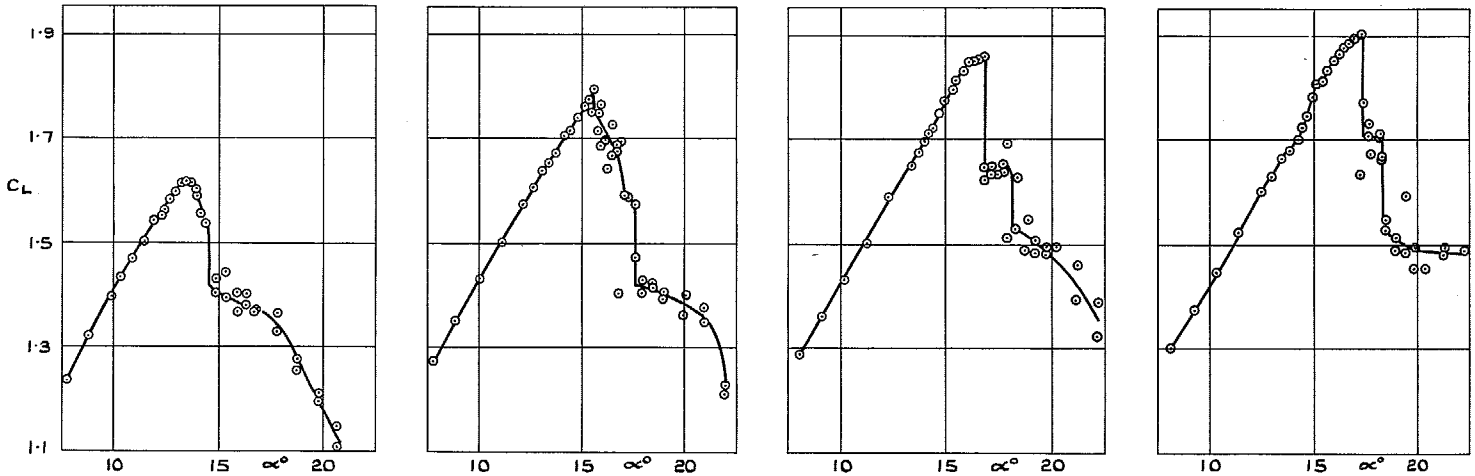

(a) C_L v α

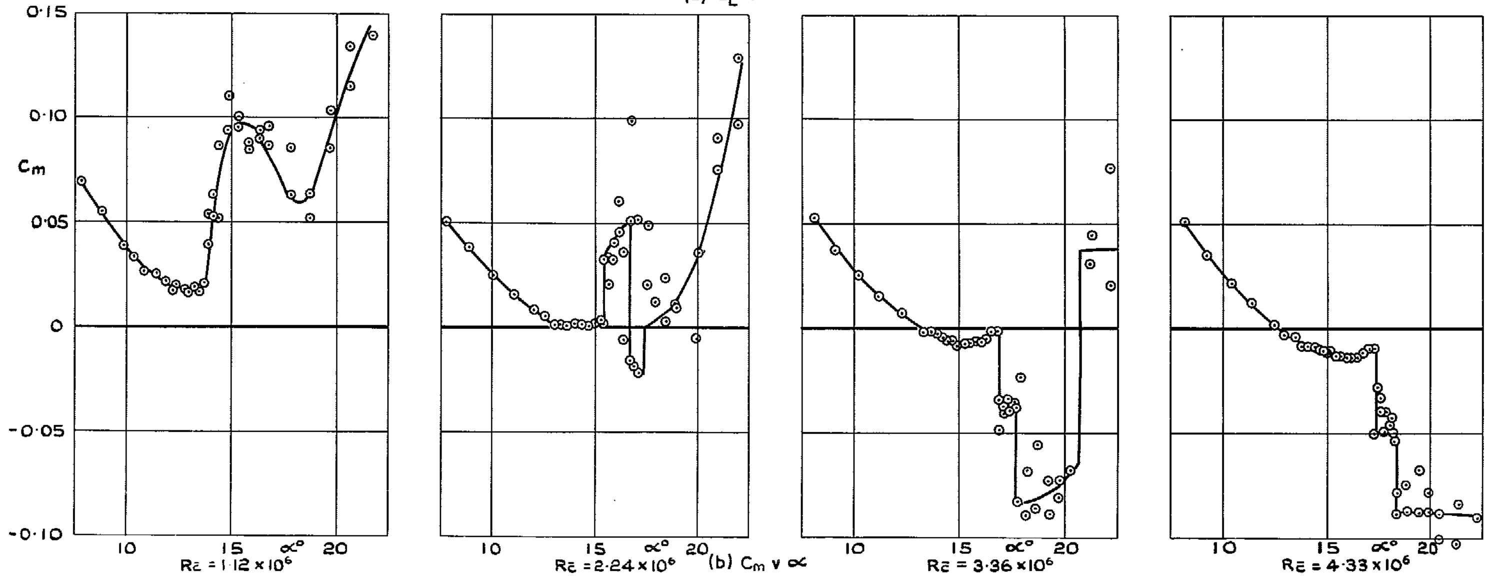

Re = 1·12 × 10⁶

Re = 2·24 × 10⁶

(b) C_m v α

Re = 3·36 × 10⁶

Re = 4·33 × 10⁶

FIG. 41a & b. Effect of Reynolds number at $M = 0{\cdot}20$ on the variation of C_L and C_m with α for the final configuration with leading edge chin (no tufts).

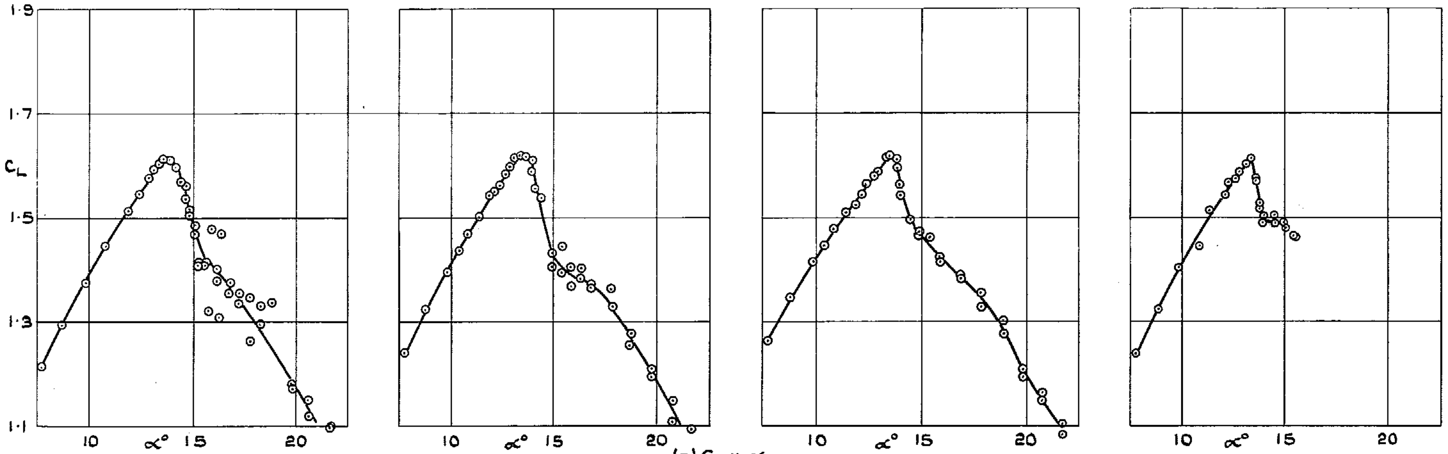

(a) C_L v α

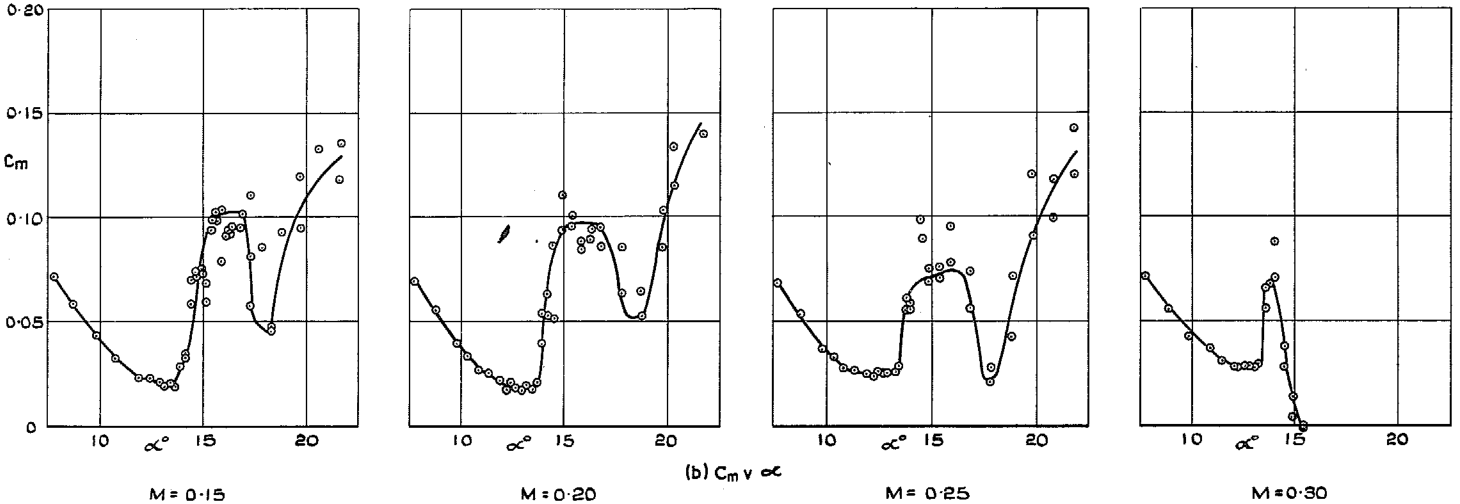

(b) C_m v α

FIG. 42a & b. Effect of mach number at $R_{\bar{c}} = 1{\cdot}12 \times 10^6$ on the variation of C_L and C_m with α for the final configuration with leading edge chin (no tufts).

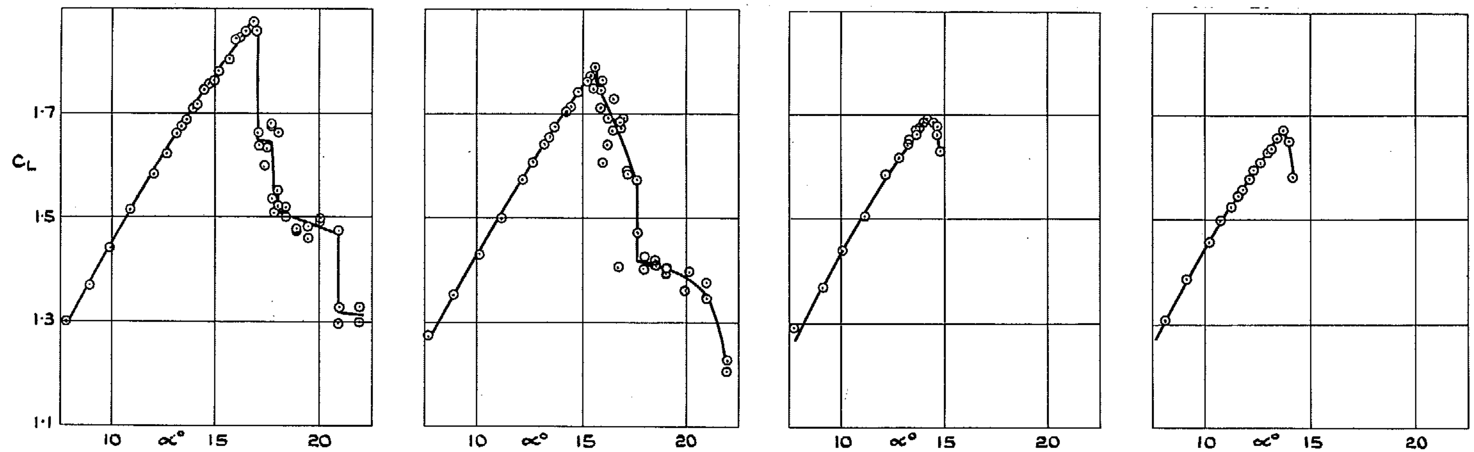

(a) C_L v α

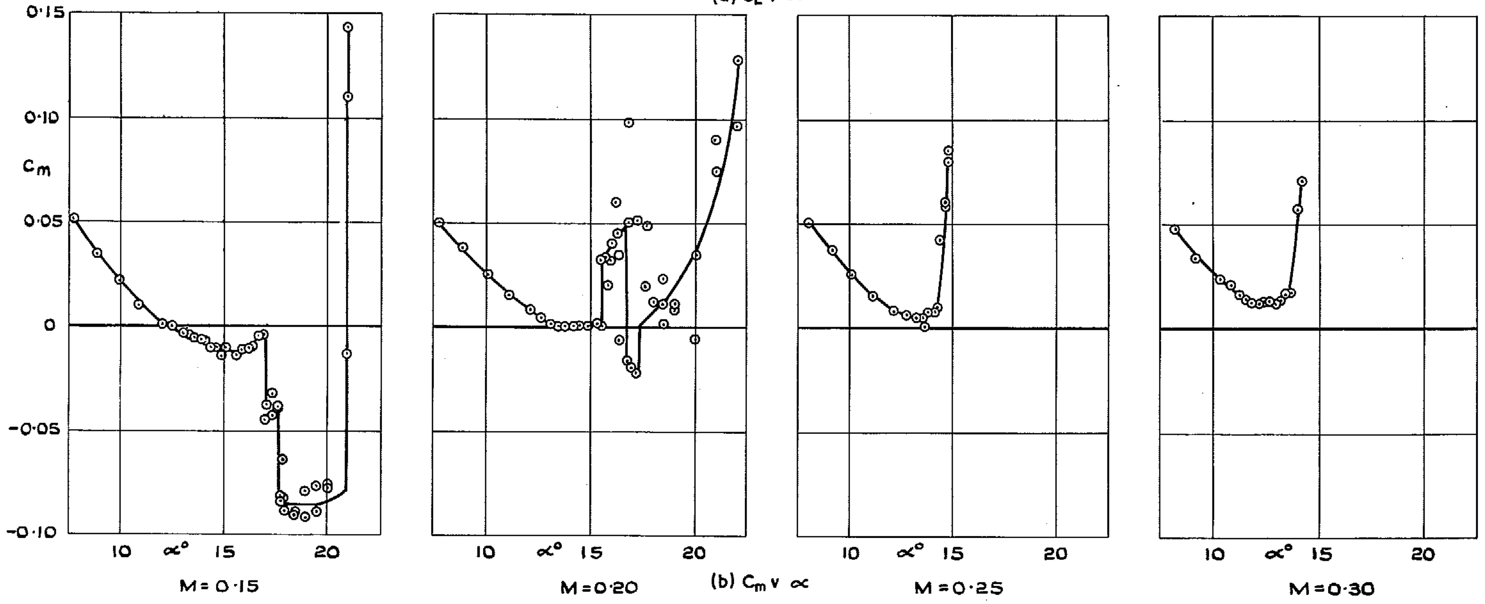

(b) C_m v α

FIG. 43a & b. Effect of mach number at $R_{\bar{c}} = 2{\cdot}24 \times 10^6$ on the variation of C_L and C_m with α for the final configuration with leading edge chin (no tufts).

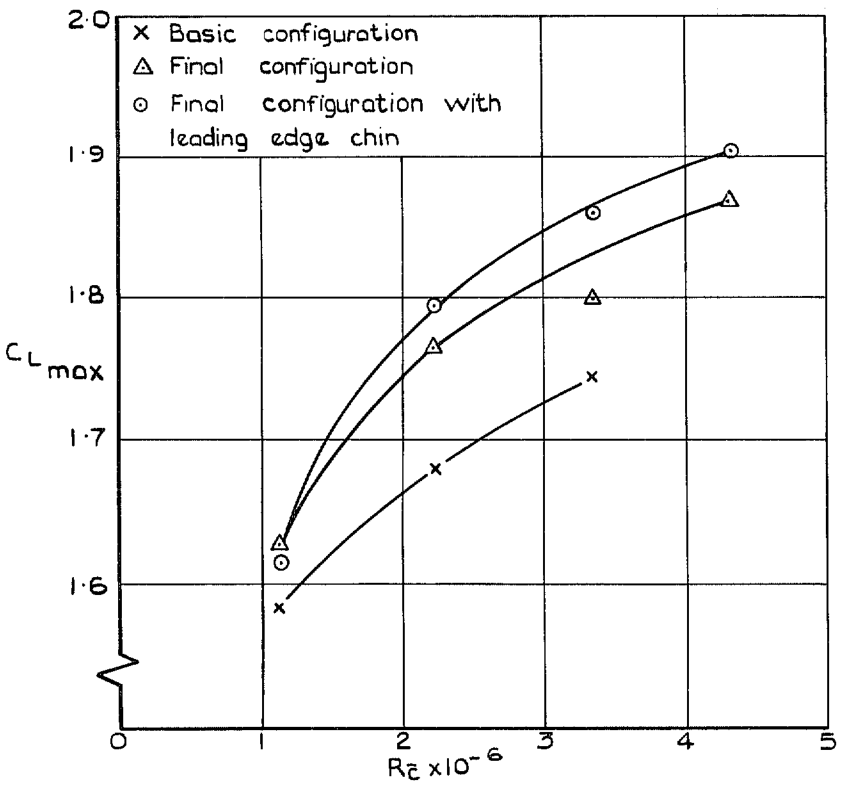

(a) Effect of Reynolds No; M = 0·20, no tufts

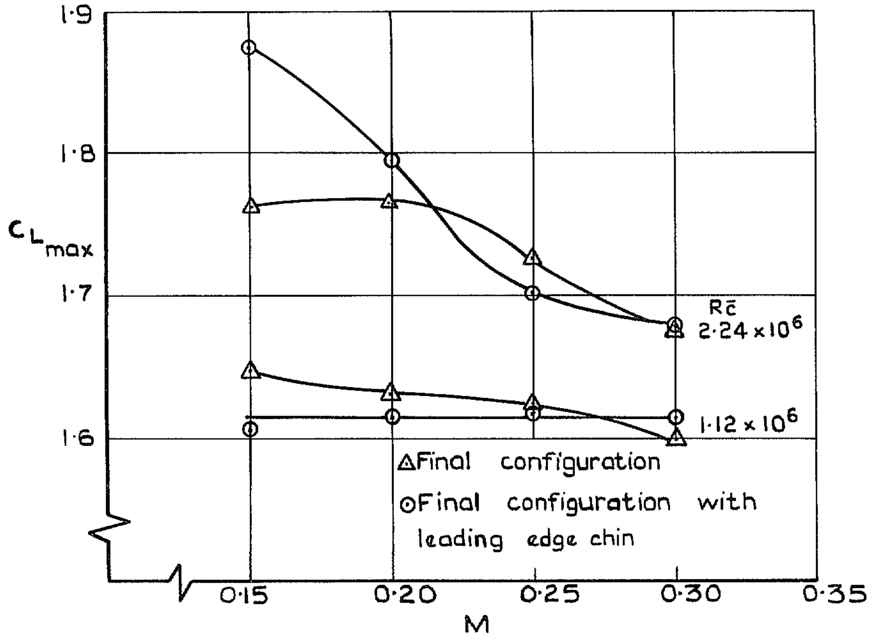

(b) Effect of Mach No; $R_{\bar{c}} = 1{\cdot}12 \times 10^6$ and $2{\cdot}24 \times 10^6$, no tufts

FIG. 44a & b. Effect of Reynolds number and Mach number on $C_{L\max}$.

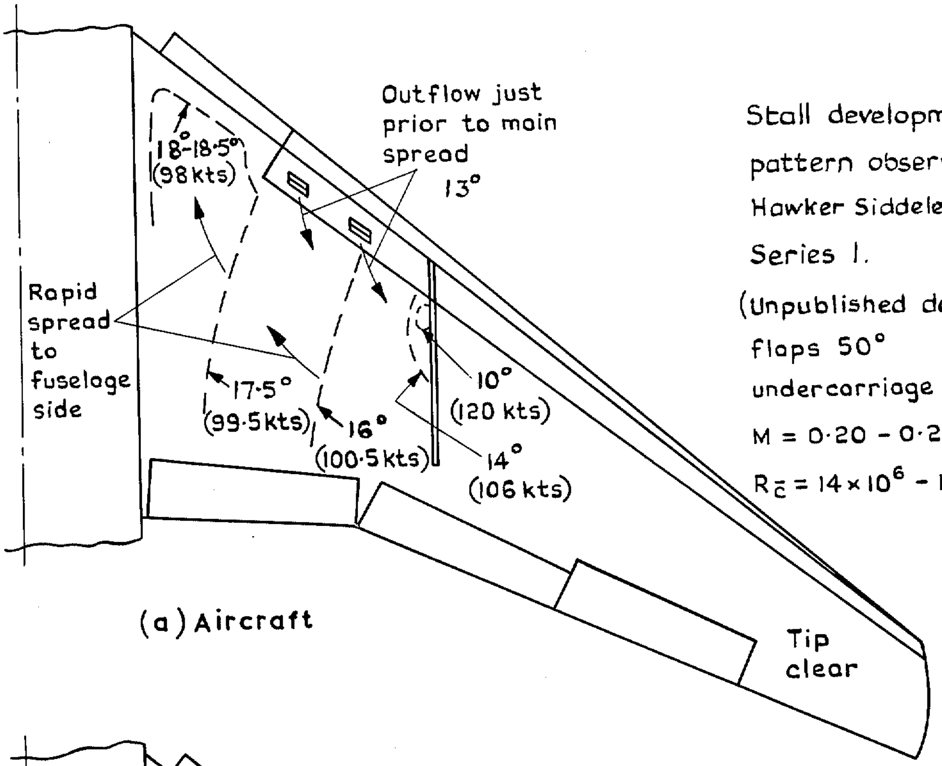

Stall development pattern observed on Hawker Siddeley Trident Series I.
(Unpublished data)
flaps 50°
undercarriage down
$M = 0{\cdot}20 - 0{\cdot}21$
$R_{\bar{c}} = 14 \times 10^6 - 15 \times 10^6$

(a) Aircraft

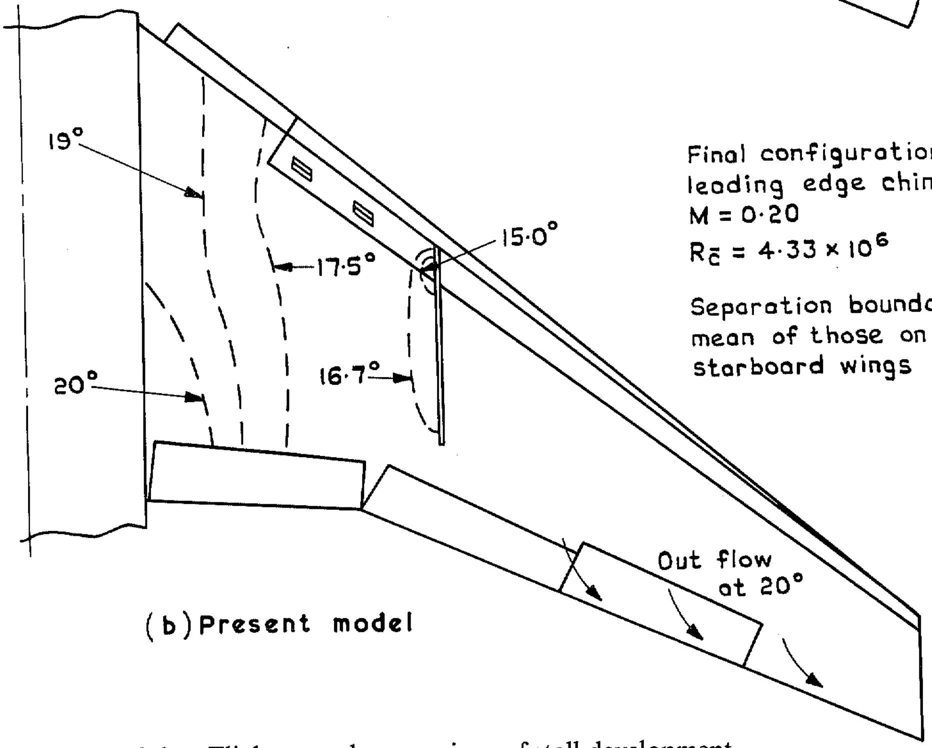

Final configuration with leading edge chin
$M = 0{\cdot}20$
$R_{\bar{c}} = 4{\cdot}33 \times 10^6$

Separation boundaries are mean of those on port and starboard wings

(b) Present model

FIG. 45a & b. Flight-tunnel comparison of stall development.

Printed in Wales for Her Majesty's Stationery Office by Allens Printers (Wales) Limited

Dd. 146916 K.5.

R. & M. No. 360

Published by
HER MAJESTY'S STATIONERY OFFICE

To be purchased from
49 High Holborn, London WC1
13a Castle Street, Edinburgh EH2 3AR
109 St Mary Street, Cardiff CF1 1JW
Brazennose Street, Manchester M60 8AS
50 Fairfax Street, Bristol BS1 3DE
258 Broad Street, Birmingham 1
7 Linenhall Street, Belfast BT2 8AY
or through any bookseller

R. & M. No. 360

SBN 11 470244